



THE HONG KONG
POLYTECHNIC UNIVERSITY

香港理工大學

Pao Yue-kong Library

包玉剛圖書館

Copyright Undertaking

This thesis is protected by copyright, with all rights reserved.

By reading and using the thesis, the reader understands and agrees to the following terms:

1. The reader will abide by the rules and legal ordinances governing copyright regarding the use of the thesis.
2. The reader will use the thesis for the purpose of research or private study only and not for distribution or further reproduction or any other purpose.
3. The reader agrees to indemnify and hold the University harmless from and against any loss, damage, cost, liability or expenses arising from copyright infringement or unauthorized usage.

If you have reasons to believe that any materials in this thesis are deemed not suitable to be distributed in this form, or a copyright owner having difficulty with the material being included in our database, please contact lbsys@polyu.edu.hk providing details. The Library will look into your claim and consider taking remedial action upon receipt of the written requests.

The Hong Kong Polytechnic University
Department of Land Surveying & Geo-Informatics

Determination of Tidal Displacements
Using the Global Positioning System

Linguo Yuan

A thesis submitted in partial fulfillment of the requirements
for the degree of Doctor of Philosophy

October 2009

CERTIFICATE OF ORIGINALITY

I hereby declare that this thesis is my own work and that, to the best of my knowledge and belief, it reproduces no material previously published or written, nor material that has been accepted for the award of any other degree or diploma, except where due acknowledgement has been made in the text.

_____ (Signed)

Linguo Yuan _____ (Name of student)

Abstract

Recent developments in precise Global Positioning System (GPS) geodesy allow to measure surface deformation at broad timescales with unprecedented global coverage and accuracy. This research mainly focuses on determination of tidal displacements in eight principal semidiurnal and diurnal frequencies using continuous GPS observations from both regional and global networks. The effects of GPS tidal displacement coefficients on long-period signals in position time-series are also investigated. Results from this research may provide independent constraints on dynamics of the Earth's interior.

Three-dimensional tidal displacement residuals of eight principal semidiurnal and diurnal constituents after removal of a priori modelled solid Earth tides were estimated from daily GPS observations using a modified precise point positioning (PPP) technique. The daily estimates of tidal displacement parameters and their variance-covariance matrices were then combined using an iterative Kalman filter to yield the final estimates. The tidal displacement estimates for all the constituents, except for K_1 and K_2 , can be resolved fairly well using more than 1,000 days of GPS observations. The K_1 and K_2 estimates with inferior accuracy are found to be strongly affected by the site's equipment (receiver and antenna) updates and the time-variable GPS constellation geometry, respectively.

Tidal displacement estimates at 12 sites in Hong Kong were determined using three to seven years of continuous GPS observations. The results were compared with

predictions from seven latest global ocean tide models. Tidal gravity measurements in Hong Kong were also used to validate the GPS results. The study shows that results from both the GPS and gravity measurements agree best with the GOT4.7 and NAO99b models, when the K_1 and K_2 constituents are excluded. The GPS/model agreements are generally at sub-millimetre level, except for S_2 , K_2 and K_1 with relatively larger errors. After removing the systematic biases between the GPS estimates and model predictions, the misfits of M_2 , S_2 , N_2 , O_1 , P_1 and Q_1 at all the sites are within 0.5 and 1.0 mm in the horizontal and vertical components, respectively, while K_1 and K_2 show relatively larger misfits of up to 2.5 mm. Compared with the modelled values, both the GPS and gravity estimates of S_2 exhibit large biases with unknown reasons.

Tidal displacement estimates at 125 IGS05 reference sites were also obtained from analysis of GPS observations from 1996 to 2006. The GPS estimates were compared with Very Long Baseline Interferometry (VLBI) estimates and seven ocean tide model predictions. The results show that GPS can determine tidal displacements with accuracy superior to VLBI for all the constituents except K_2 . The Weighted Root Mean Square (WRMS) misfits indicate that GPS is capable of estimating tidal displacements with sub-millimetre accuracy in all the three components for all the constituents except K_1 and K_2 . The AG06a model gives anomalous results compared with both the GPS and VLBI estimates, while the most recent four models (FES2004, TPXO7.1, GOT4.7 and EOT08a) fit the GPS estimates equally well at the global scale. The GPS/model residuals show large-scale spatial coherence for all

II

the constituents except K_2 . The estimates of the M_2 and O_1 constituents show the highest signal-to-noise ratios, indicating that both of the constituents are most appropriate to be used to test solid Earth tide models.

The GPS tidal displacement coefficients with the sub-millimetre accuracy for all the constituents except K_1 and K_2 have proved to effectively reduce spurious long-period signals in position time-series. This indicates that GPS tidal displacement coefficients can be used to substitute for model predictions in future global GPS data analysis. The K_1 and K_2 coefficients with poorer accuracy should be treated with caution. Including K_2 corrections, secular variations of more than 1 mm/yr are evident at some sites.

Acknowledgements

First and foremost, I would like to express my greatest thanks to my supervisors, Prof. Xiaoli Ding and Prof. Wu Chen for their enlightening guidance, constructive suggestion and constant encouragement throughout this research. Thanks also to Prof. Ding who has always allowed me enough freedom to pursue my own ideas.

I owe special thanks to Dr. Matt King at the University of Newcastle upon Tyne for his useful discussions and kind help with tidal displacement estimates using the GIPSY software. Prof. Duncan Agnew at the University of California kindly makes the SPOTL software freely available to the public and gives great help with the ocean tide loading calculation. I would like to thank Prof. Heping Sun and Dr. Jiangcun Zhou at Institute of geodesy and Geophysics, Chinese Academy of Sciences for providing the gravity results in Hong Kong and valuable discussions on tidal gravity observations. I am also grateful to Dr. Danan Dong at Jet Propulsion Laboratory (JPL) for his help and discussions about GPS data processing.

Thanks go to Prof. Dingfa Huang at Southwest Jiaotong University (SWJTU) for his continuous support, encouragement and understanding. I am also grateful to my teachers, colleagues and friends at SWJTU who helped me along the way.

I would like to acknowledge the academic and administrative staff members in the department for their help and encouragement during my studies. My fellow postgraduates and researchers over the past years are also appreciated for sharing

their research experience and making my life in Hong Kong more colorful.

The invaluable comments and suggestions from two external examiners, Prof. Will Featherstone at Curtin University of Technology and Prof. Benjamin Fong Chao at National Central University, are highly appreciated.

I especially want to thank my beloved, Dr. Ping Zhong. Without her unwavering support, encouragement and love, none of this would be possible. Finally, I am deeply grateful to my parents and sister for their support and encouragement all these years.

The providers of global and regional ocean tide models are appreciated. Thanks to JPL for providing the GIPSY software and global GPS products. The Lands Department of Hong Kong Special Administrative Region government is acknowledged for freely providing GPS observations in Hong Kong. GPS observations of globally distributed sites were furnished by the International GNSS Service (IGS). Some of the figures were generated using the GMT software (Wessel and Smith, 1998). This research was funded by the Ph.D. scholarship (RGLV) of the Hong Kong Polytechnic University.

Table of contents

Abstract	I
Acknowledgements	V
Table of contents.....	VII
List of figures	XI
List of tables.....	XVII
Chapter 1 Introduction	1
1.1 Background	1
1.2 Geodetic observations of Earth tides	2
1.3 Aims and scope of this research.....	5
Chapter 2 Tidal displacements: theory and modelling.....	9
2.1 The tidal force	9
2.2 The tidal potential	11
2.3 Solid Earth tides	17
2.4 Basic theory for computing surface loading	21
2.4.1 The load potential.....	22
2.4.2 Spherical harmonic approach.....	24
2.4.3 Green's function approach	25
2.5 Ocean tide loading	27
2.5.1 Ocean tide models.....	28
2.5.2 Computational methods	32
2.5.3 Geocentre motion due to ocean tides	34
2.6 Atmospheric tide loading.....	36
2.7 Pole tide.....	39
2.8 Summary	41

Chapter 3	GPS estimates of tidal displacements.....	43
3.1	Precise point positioning using the GIPSY/OASIS II software.....	45
3.2	Estimation strategy.....	47
3.2.1	Semi-diurnal/diurnal processing technique.....	48
3.2.2	Kalman filter combination.....	50
3.2.3	Nodal corrections.....	53
3.3	Technical issues related to GPS estimates of tidal displacements.....	55
3.3.1	Constituent convergence.....	55
3.3.2	Ambiguity resolution.....	56
3.3.3	Source of biases.....	57
3.4	Summary.....	60
Chapter 4	Estimates of tidal displacements using a dense GPS network in Hong Kong.....	63
4.1	Tidal characteristics in Hong Kong and GPS datasets.....	65
4.2	Data processing.....	67
4.3	Ambiguity resolution.....	71
4.4	Results.....	73
4.4.1	Comparison with modelled OTL displacements.....	75
4.4.2	Comparison with gravity results.....	83
4.5	Summary.....	85
Chapter 5	Tidal displacements derived from a global GPS network..	89
5.1	Dataset and data processing.....	90
5.2	Results.....	97
5.2.1	Comparison with modelled OTL displacements.....	97
5.2.2	Comparison with VLBI estimates.....	106
5.2.3	Spatial variations of tidal displacement residuals.....	109
5.3	Searching for mis-modelled or un-modelled tidal displacements.....	122
5.3.1	Tidal geocentre motion.....	122

5.3.2	Solid Earth tide modelling errors	123
5.3.3	OTL modelling errors.....	125
5.3.4	Atmospheric tide loading	126
5.3.5	GPS-related errors.....	129
5.4	Summary	130
Chapter 6 Effects of GPS tidal displacement estimates on long-period signals in position time-series.....		133
6.1	Spurious long-period signals in GPS position time-series.....	135
6.2	GPS data processing.....	139
6.3	Results from the GPS network in Hong Kong.....	140
6.4	Results from the global GPS network.....	150
6.4.1	Constituents except K_1 and K_2	151
6.4.2	K_1 constituent.....	155
6.4.3	K_2 constituent.....	160
6.5	Summary	166
Chapter 7 Conclusions and recommendations.....		169
7.1	Conclusions	169
7.2	Recommendations for future work	172
Appendix A Auxiliary materials for Chapter 4.....		175
Appendix B Auxiliary materials for Chapter 5.....		177
Appendix C Auxiliary materials for Chapter 6.....		179
References		181

List of figures

Figure 2.1 Graphic of tidal forces	10
Figure 2.2 Vertical displacements of the S_1 and S_2 tides derived from the Ray and Ponte (2003) model, using Farrell's (1972) elastic Green's functions in the centre of earth frame (CE)	38
Figure 3.1 The daily unit variances at the ALGO site after the first iteration of the combined processing.....	52
Figure 3.2 The time-dependent nodal correction parameters at the ALGO site during the period from 1996 to 2007.....	54
Figure 4.1 Location of 12 GPS sites and one gravity site in the coastal area of Hong Kong.....	66
Figure 4.2 Parameter convergence of the HKFN site showing the amplitudes of residual vectors after the addition of each daily ambiguity-free solution, relative to the final ambiguity-fixed estimates for east (top), north (middle) and vertical (bottom).....	68
Figure 4.3 Parameter convergence of the HKFN site showing the amplitudes of residual vectors after the addition of each daily ambiguity-fixed solution, relative to the final ambiguity-fixed estimates for east (top), north (middle) and vertical (bottom).....	69
Figure 4.4 Effects of different process noises of K_2 on GPS tidal displacement estimates.....	70
Figure 4.5 Parameter correlations of the tidal displacements from the ambiguity-free (left) and ambiguity-fixed (right) estimates at HKPC	72

Figure 4.6 Box and whisker plot of the amplitudes of the vector differences between the ambiguity-free and ambiguity-fixed estimates for each constituent 74

Figure 4.7 Misfits of the GPS ambiguity-fixed tidal displacement estimates to the model predictions 77

Figure 4.8 Misfits of the GPS-derived tidal displacement estimates to the NAO99b model estimates before (left panel) and after (right panel) removing the mean systematic biases 78

Figure 4.9 Phasor diagrams of tidal gravity estimates in Hong Kong..... 84

Figure 5.1 Histogram of daily solutions for global GPS sites..... 91

Figure 5.2 Effects of adding different process noises to K_2 on GPS tidal displacement estimates..... 92

Figure 5.3 Convergence plots of the inland site ALGO (left) and the coastal site MAC1(right), showing the amplitudes of residual vectors after the addition of each daily solution, relative to the final tidal estimates, for the east (top), north (middle) and vertical (bottom) components 93

Figure 5.4 Convergence plots of the WUHN site, showing the amplitudes of residual vectors after the addition of each daily solution, relative to the final tidal estimates, for the east (top), north (middle) and vertical (bottom) components..... 94

Figure 5.5 Parameter correlations of the tidal displacements at five representative sites..... 96

Figure 5.6 RMS misfits of the GPS tidal displacement estimates to the model predictions 98

Figure 5.7 Misfits of the GPS and VLBI estimates to the FES2004 predictions 100

Figure 5.8 Box and whisker plot of the amplitudes of the vector differences between the GPS estimates and FES2004 predictions for 45 inland sites (left panel) and 80 coastal sites (right panel)..... 102

Figure 5.9 The RMS misfits of the VLBI tidal displacement estimates to the model predictions 107

Figure 5.10 Box and whisker plot of the amplitudes of the vector differences between the VLBI estimates and FES2004 predictions for 18 inland sites (left panel) and 22 coastal sites (right panel)..... 108

Figure 5.11 Phasor diagrams of the M_2 tidal displacement residuals after removing the FES2004 predictions 112

Figure 5.12 Phasor diagrams of the S_2 tidal displacement residuals after removing the FES2004 predictions 113

Figure 5.13 Phasor diagrams of the N_2 tidal displacement residuals after removing the FES2004 predictions 114

Figure 5.14 Phasor diagrams of the K_2 tidal displacement residuals after removing the FES2004 predictions 115

Figure 5.15 Phasor diagrams of the K_1 tidal displacement residuals after removing the FES2004 predictions 116

Figure 5.16 Phasor diagrams of the O_1 tidal displacement residuals after removing the FES2004 predictions 117

Figure 5.17 Phasor diagrams of the P_1 tidal displacement residuals after removing the FES2004 predictions 118

Figure 5.18 Phasor diagrams of the Q_1 tidal displacement residuals after removing the FES2004 predictions 119

Figure 5.19 Phasor diagrams of the M_2 tidal displacement residuals after removing the FES2004 predictions in North America (left) and Europe (right)..... 121

Figure 5.20 Phasor diagrams of the S_2 tidal displacement residuals before (blue arrows) and after (red arrows) removing the effects of modelled atmospheric tide loading..... 128

Figure 6.1 Effect of different tidal displacement corrections on position time-series (ts21) at HKFN..... 144

Figure 6.2 Effect of different tidal displacement corrections on position time-series (ts31) at HKFN..... 145

Figure 6.3 Effect of different tidal displacement corrections on position time-series (ts24) at HKFN..... 146

Figure 6.4 Effect of different tidal displacement corrections on position time-series (ts43) at HKFN..... 147

Figure 6.5 Annual amplitudes with 3-sigma error bars of position time-series due to the propagation of different tidal corrections 148

Figure 6.6 Semiannual amplitudes with 3-sigma error bars of position time-series due to the propagation of different tidal corrections 149

Figure 6.7 Secular rates with 3-sigma error bars of position time-series due to the propagation of different tidal corrections..... 150

Figure 6.8 Annual variations due to the propagation of GPS/model tidal displacement corrections for all the principal constituents except K_1 and K_2 . 153

Figure 6.9 Semiannual variations due to the propagation of GPS/model tidal displacement corrections for all the principal constituents except K_1 and K_2 . 154

Figure 6.10 Annual variations due to the propagation of GPS/model tidal displacement corrections for the K_1 constituent 157

Figure 6.11 Semiannual variations due to the propagation of GPS/model tidal displacement corrections for the K_1 constituent 158

Figure 6.12 Velocity differences due to the propagation of GPS/model tidal displacement corrections for the K_1 constituent 159

Figure 6.13 Difference time-series (ts24) at sites PIE1 and KUNM..... 160

Figure 6.14 Difference time-series (ts43) at KUNM (left panel) and RABT (right panel)..... 162

Figure 6.15 Velocity differences due to the propagation of GPS/model tidal displacement corrections for the K_2 constituent. 163

Figure 6.16 Annual variations due to the propagation of GPS/model tidal displacement corrections for the K_2 constituent 164

Figure 6.17 Semiannual variations due to the propagation of GPS/model tidal displacement corrections for the K_2 constituent 165

List of tables

Table 2.1 Six astronomical arguments.....	15
Table 2.2 The largest degree-2 tidal harmonics, sorted by size of each species.....	16
Table 2.3 Global ocean tide models from the automatic loading service.....	29
Table 2.4 Coefficients for the tidally induced geocentre motion derived from the ocean tide model FES2004	36
Table 4.1 Chi-square per degree-of-freedom for the GPS and gravity estimates to the model predictions	82
Table 5.1 The WRMS misfits of the residual amplitudes of the GPS and VLBI tidal displacement estimates with respect to the FES2004 model	104
Table 5.2 The total WRMS misfits of the residual amplitudes of the GPS and VLBI tidal displacement estimates with respect to the model predictions	105
Table 6.1 Five maximum aliased long periods for eight principal semidiurnal and diurnal tidal constituents calculated using Eqs. (30) and (35) of Stewart et al. (2005).....	137

Chapter 1 Introduction

1.1 Background

The gravitational attractions of the Sun and the Moon cause deformations of the solid Earth and oceans. They are respectively called the solid Earth tides and ocean tides. The elastic response of the solid Earth to ocean tides is known as Ocean Tide Loading (OTL). Site displacements due to the solid Earth tides can reach several tens of centimeters in low-latitude regions, and those due to OTL may be up to more than ten centimeters in some coastal areas. Deformation caused by polar motion, the so-called pole tide, has also to be taken into account. Furthermore, contribution from atmospheric tides mainly generated by solar thermal effects, not gravitational attraction, can be as large as 1 to 2 mm in the vertical component at the semidiurnal and diurnal periods, but is generally neglected in geodetic analysis at present.

Investigation of tidal deformation has three main goals in geophysics (Agnew, 2007): 1) to remove tidal effects from geodetic and geophysical observations by modelling the tidal variations; 2) to investigate the structure of the Earth's interior using observations of Earth tides; and 3) to get insights into the influence of Earth tides on some geophysical events. For example, Earth tides may trigger earthquakes and volcanism (e.g., Kasahara, 2002; Cochran et al., 2004).

Earth tides were observed indirectly more than one hundred years ago (Brush, 1996), however, our knowledge of the Earth's interior mainly comes from other fields, especially from seismology. The development of tidal observation techniques, with

continually increasing accuracy, has gradually changed this situation. Recently, studies on Earth tides have become increasingly important in geodesy and geophysics. Modern geodetic techniques have been demonstrated to measure both site displacements with accuracy at millimetre level (Petrov and Ma, 2003; Thomas et al., 2007) and gravity variations with accuracy of less than $0.1 \mu\text{Gal}$ (10^{-8} m s^{-2}) (Baker and Bos, 2003; Hinderer and Crossley, 2004) at principal semidiurnal and diurnal tidal frequencies.

1.2 Geodetic observations of Earth tides

The earliest tidal measurements were made with tiltmeters and strainmeters (Agnew, 1986; Zürn, 1997). The resulting tidal deformations are heavily distorted by local heterogeneities in the Earth's crust so that the global or even regional response cannot be measured reliably. On the other hand, if the effects of the global Earth tides are removed from these observations, then we might be able to use the residuals to investigate local geological structure. This is an application where tides have proven useful (e.g., Thomas et al., 2009).

Relative gravimeters, especially Superconducting Gravimeters (SG), are considered conventionally the most accurate technique for estimating gravity variations due to Earth tides. A global network of SG stations under the global geodynamics project (GGP) (Crossley et al., 1999; Hinderer and Crossley, 2000) has brought substantial improvement in tidal studies. Sun et al. (2005) investigated the adaptability of the ocean and Earth tidal models comprehensively using observations from 22

high-precision SG stations. Their results show that the discrepancies between the global mean amplitude factors and theoretical values are less than 0.3%, and the largest calibration error of the instruments is less than 0.5%. The high sensitivity of SGs enables them to detect small-amplitude nonlinear ocean tides (Boy et al., 2004; Khan and Hoyer, 2004). The much smaller instrumental drift of SGs compared with mechanical spring meters permit more accurate studies on long-period tides (Ducarme et al., 2004; Iwano et al., 2005; Boy and Hinderer, 2006). SGs can also provide accurate measurements of the Nearly Diurnal Free Wobble (NDFW) resonance (Xu et al., 2002; Sato et al., 2004; Sun et al., 2004; Rosat and Lambert, 2009).

There still exist calibration issues when tidal gravity observations are used to test ocean tide or solid Earth tide models. An amplitude calibration accuracy of 0.1% or even better is required, but calibration to this level has proved to be difficult (Hinderer et al., 2007). Baker and Bos (2003) used tidal gravity observations from spring gravimeters and SGs to test solid Earth and ocean tide models. They concluded that the estimated calibration errors at the European stations are of the order 0.1%. It is therefore impossible to distinguish between the Dehant-Defraigne-Wahr (DDW) elastic and inelastic Earth models (Dehant et al., 1999) whose gravimetric factors differ only by 0.12%. Errors in calibration can reach 0.3% at some sites outside Europe. This has been confirmed by other studies (e.g. Boy et al., 2003; Sun et al., 2005).

The latest methods for measuring Earth tides come from the techniques of space geodesy. Very Long Baseline Interferometry (VLBI) observations have been used to observe Earth tides since the 1980s. Ryan et al. (1986) first estimated Love and Shida numbers using VLBI observations. Mitrovica et al. (1994a) estimated complex h_2 Love numbers within the diurnal band and resolved the Free Core Nutation (FCN) resonance period and phase lag. Estimates of vertical OTL parameters were presented by Sovers (1994) and Haas and Schuh (1998). The study by Petrov and Ma (2003) has shown that the accuracy of tidal displacements estimated using VLBI observations reaches up to 0.5 and 1.7 mm in the horizontal and vertical components, respectively. However, the uneven and sparse distribution of VLBI sites restricts, to some extent, the investigation of Earth tides. Another limitation of VLBI is that there are no continuous observations.

Compared with SG and VLBI techniques, the high spatial density and more complete temporal coverage of continuous Global Positioning System (GPS) sites makes this geodetic technique particularly attractive. Recent studies have demonstrated that GPS is capable of determining tidal displacements with accuracy comparable to those achieved by VLBI (e.g., King et al., 2005; Thomas et al., 2007).

Previous studies on GPS estimates of tidal measurements mainly focused on a few coastal areas where ocean tide modelling is generally considered to be deficient (e.g., Khan and Tscherning, 2001; King et al., 2005; Yun et al., 2007; Vergnolle et al., 2008) in order to validate ocean tide models. Few studies have been conducted using

observations from the global GPS network operated by the International GNSS Service (IGS). Schenewerk et al. (2001) firstly estimated vertical tidal displacements at eight principal semidiurnal and diurnal constituents for 353 globally distributed sites using three years of GPS observations. They found that there exist large scale systematic differences between the observations and predictions from ocean tide models. Unfortunately, the horizontal component was neglected in their study and the accuracy of the estimated tidal displacements is too poor to be used for testing ocean tide models, let alone solid Earth tide models (Petrov and Ma, 2003; King et al., 2005). From only 25 co-located GPS and VLBI sites analysed, Thomas et al. (2007) demonstrated that no apparent latitude or longitude dependence exists in residuals after modelled solid Earth tides and OTL effects are removed.

1.3 Aims and scope of this research

This research involves two main objectives: 1) using continuous GPS observations to estimate tidal displacements of eight principal semidiurnal and diurnal constituents, and 2) investigating the effects of GPS tidal displacement estimates on long-period signals in position time-series. This work makes a contribution to Earth science in that it opens a door to investigate solid Earth tides and ocean tide loading using a global continuous GPS network.

Chapter 2 provides an overview of fundamentals for modelling tidal displacements along with some existing modelling approaches and issues. The theory and computation methods of modelling solid Earth tides and so-called loading tides are

first presented. Current states of modelling solid Earth tides, OTL and Atmospheric Tide Loading (ATL) are also discussed. Additionally, rotational deformation due to polar motion is taken into account although it does not affect GPS estimates of subdaily tidal displacements (see Section 2.7 for reason).

The static estimation technique for tidal displacements from continuous GPS observations using a modified Precise Point Positioning (PPP) technique is developed in Chapter 3. A two-step processing strategy how to derive tidal displacement estimates from GPS observations is described in detail. Some key issues related to this method are then discussed in order to show how the method is dependent on the data quantity and processing strategy.

Chapter 4 assesses the accuracy of tidal displacement estimates using observations spanning three to seven years from a local dense continuous GPS network in the coastal areas of Hong Kong. This dense network distribution allows evaluation of the resolution and accuracy of tidal displacements estimated by GPS. The GPS-derived tidal displacements are compared with the predictions from seven of the latest global ocean tide models. Tidal gravity measurements in Hong Kong are also used to validate the GPS results and to identify technique-specific systematic errors. Impact of integer ambiguity fixing on tidal displacement solutions is also investigated in detail.

Three-dimensional tidal displacements for 125 globally distributed GPS sites at eight major semidiurnal and diurnal frequencies are determined using GPS

observations from 1996 to 2006 in Chapter 5. The GPS results are evaluated and compared with VLBI estimates and seven global ocean tide model predictions. Effects of uncertainties in existing models of displacements due to solid Earth tides, OTL, and ATL are also discussed.

To explore the necessity and potential of the GPS tidal displacement estimates as substitutes for predictions of ocean tide models, the effects of GPS tidal displacements on long-period signals in position time-series at 12 sites in Hong Kong and 125 IGS05 reference sites are investigated in Chapter 6. Different position time-series are generated using various tidal displacement coefficients to provide a convenient means of assessing how a particular GPS/model signal propagates in GPS data analysis.

Finally, conclusions and recommendations for future research are summarised in Chapter 7. Electronic auxiliary materials related to this thesis are attached in Appendices A-C.

Chapter 2 Tidal displacements: theory and modelling

Tides arise as result of the combination of the gravitational attraction of celestial bodies (mainly the Sun and Moon) and the centrifugal force of the rotation of the Earth itself. Tides produce site displacements that can be far larger than those caused by tectonic processes. Theoretical modelling of the tidal displacements is a necessary part of the analysis of space geodetic data. The tidal displacements can be classified into the following categories at present: solid Earth tides (the direct primary effect), Ocean Tide Loading (OTL), Atmospheric Tide Loading (ATL) and pole tide (secondary effects).

The aim of this chapter is to give a brief overview of basic theory for modelling tidal displacements and to present some of the current modelling approaches and issues. This chapter begins with a brief introduction of the tidal force, followed by a description of the tide-raising potential. Then modelling solid Earth tides is treated. After this, the theory and computation method of the so-called surface loading are presented. Current states of modelling OTL and ATL are discussed. Finally, the rotational deformation due to polar motion is taken into account.

2.1 The tidal force

The combined gravitational forces from the Sun and Moon hold the Earth in orbit about the Earth-Moon-Sun centre-of-mass. The gravitational acceleration is not constant at different parts of the Earth. One side of the Earth has greater acceleration

than its center-of-mass, and the other side of the Earth has lesser acceleration, as shown in Figure 2.1. It is usual to separate the luni-solar gravitational force into two parts: one that causes the orbital motion is constant over the Earth, and a small remainder which causes the tides is called the tidal force. The tidal force causes deformation of the solid Earth, ocean and atmosphere. These are respectively called Earth tides (also called body tides), ocean tides and atmospheric tides.

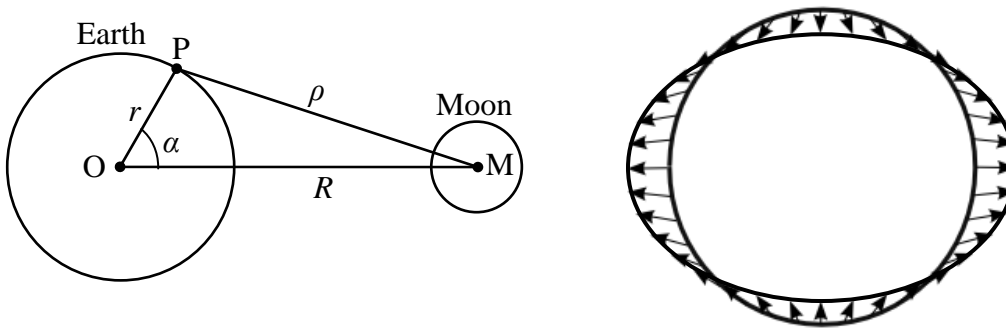


Figure 2.1 Graphic of tidal forces. The Moon's (or Sun's) gravity differential field at the surface of the Earth is known as the tide force. On the left is the geometry of the problem for computing the tidal force at a point P on the Earth, given an external body M (the Moon or Sun). The right plot shows the tidal forces (accelerations) at the surface of the Earth due to the body M. The elliptical line shows the equipotential surface under the tidal force, greatly exaggerated.

According to Newton's universal law of gravitation, the tidal acceleration vector

\vec{g}_{tid} at point P due to the attraction of an external body M is

$$\vec{g}_{\text{tid}} = \vec{g}_P - \vec{g}_C = \frac{GM_{\text{ext}}}{\rho^2} \cdot \frac{\vec{\rho}}{\rho} - \frac{GM_{\text{ext}}}{R^2} \cdot \frac{\vec{R}}{R} \quad (1.1)$$

where G is the Newtonian gravitational constant, M_{ext} the mass of the external body. The external body is considered to act as point mass due to its large distance from the Earth. The other variables are shown in Figure 2.1: $\vec{\rho}$ is the distance vector from P to M, \vec{R} the distance vector from O to M. At the geocentre O, the distances ρ and R to the external body are identical and therefore the tidal acceleration is zero.

2.2 The tidal potential

The scalar tidal potential V_{tid} is now derived instead of the vectorial tidal acceleration \vec{g}_{tid} in order to enable an expansion of the tidal potential into scalar spherical harmonics, following the development in Munk and Cartwright (1966). This will allow the separation of the tidal potential into time-dependent terms and space-dependent terms, and the spectral representation of the tidal potential by a tidal potential catalogue.

The tidal acceleration vector \vec{g}_{tid} is defined as the gradient of the tidal potential V_{tid}

$$\vec{g}_{\text{tid}} = \frac{\partial V_{\text{tid}}}{\partial \vec{r}} = \nabla V_{\text{tid}} \quad (1.2)$$

where \vec{r} describes the geocentric coordinates of the point P. Considering the additional constraint that the tidal potential vanishes at the geocentre O: $V_{\text{tid}} = 0$ for $\vec{r} = \vec{0}$, the solution of (1.2) is

$$V_{\text{tid}} = GM_{\text{ext}} \left(\frac{1}{\rho} - \frac{1}{R} - \frac{r \cdot \cos \alpha}{R^2} \right) \quad (1.3)$$

where α is the angular distance between P and the sub-body point of M. Writing Eq. (1.3) as a series of Legendre polynomials, yields

$$V_{\text{tid}}(t) = \frac{GM_{\text{ext}}}{R(t)} \sum_{n=2}^{\infty} \left(\frac{r}{R(t)} \right)^n P_n[\cos \alpha(t)] \quad (1.4)$$

where R and α , as they actually are, functions of time t , so the tidal potential V_{tid} is a function of time t as well.

Since the relation r/R is about 1/61 for the Moon and about 1/23481 for the Sun, the series expansion in Eq. (1.4) converges quickly with increasing n . In practice, only the $n = 2$ and $n = 3$ terms need to be considered for the Moon, while the degree-2 tides completely dominate for the Sun. Note also that for $n = 2$, the magnitude of V_{tid} is proportional to GM_{ext} / R^3 . If we normalise this quantity to make the value for the Moon equal to 1, the value for the Sun is about 0.46, for Venus 5×10^{-5} , and for Jupiter 6×10^{-6} , and even less for other planets. So only the lunisolar tides need to be considered in actual measurements.

Using the geographical coordinates of colatitude and longitude (θ, λ) for the observation point P (time invariant) and $(\theta'(t), \lambda'(t))$ for the sub-body point M, we may apply the addition theorem for spherical harmonics (Hobson, 1955) to get

$$V_{\text{tid}}(t) = \frac{GM_{\text{ext}}}{R(t)} \sum_{n=2}^{\infty} \left(\frac{r}{R(t)} \right)^n \frac{4\pi}{2n+1} \sum_{m=-n}^n Y_{n,m}^*(\theta'(t), \lambda'(t)) Y_{n,m}(\theta, \lambda) \quad (1.5)$$

where the fully normalised complex spherical harmonics $Y_{n,m}(\theta, \lambda)$ are defined by

$$Y_{nm}(\theta, \lambda) = (-1)^m \left[\frac{2n+1}{4\pi} \frac{(n-m)!}{(n+m)!} \right]^{1/2} P_n^m(\cos \theta) e^{im\lambda} \quad (1.6)$$

with P_n^m the associated Legendre function of degree n and order m .

The tidal potential is conventionally expressed as V_{tid}/g , where g is the Earth's mean gravitational acceleration. If, as is conventional, g is taken to have its value on the Earth's equatorial radius r_{eq} , and r is held fixed at the radius in Eq. (1.5), we get

$$\frac{V_{\text{tid}}(t)}{g} = r_{\text{eq}} \frac{M_{\text{ext}}}{M} \sum_{n=2}^{\infty} \left(\frac{r_{\text{eq}}}{R(t)} \right)^{n+1} \frac{4\pi}{2n+1} \sum_{m=-n}^n Y_{n,m}^*(\theta'(t), \lambda'(t)) Y_{n,m}(\theta, \lambda) \quad (1.7)$$

where M is the mass of the Earth.

Now adopt the approach of Cartwright and Tayler (1971) to separate the tide potential into the time-dependent and space-dependent parts a bit more explicitly. If define complex (and time-varying) coefficients $T_{n,m}(t) = a_n^m(t) + ib_n^m(t)$, we can write Eq. (1.7) as the following simple form

$$\begin{aligned} \frac{V_{\text{tid}}(t)}{g} &= \text{Real} \left[\sum_{n=2}^{\infty} \sum_{m=0}^n T_{n,m}^*(t) Y_{n,m}(\theta, \lambda) \right] \\ &= \sum_{n=2}^{\infty} \sum_{m=0}^n N_n^m P_n^m(\cos \theta) \left[a_n^m(t) \cos m\lambda + b_n^m(t) \sin m\lambda \right] \end{aligned} \quad (1.8)$$

Then the coefficients $T_{n,m}$ are, for $m = 0$

$$T_{n,0}(t) = \left(\frac{4\pi}{2n+1} \right)^{1/2} r_{\text{eq}} \frac{M_{\text{ext}}}{M} \left(\frac{r_{\text{eq}}}{R(t)} \right)^{n+1} P_n^0(\cos \theta'(t)) \quad (1.9)$$

and, for $m \neq 0$

$$T_{n,m}(t) = (-1)^m \frac{8\pi}{2n+1} r_{\text{eq}} \frac{M_{\text{ext}}}{M} \left(\frac{r_{\text{eq}}}{R(t)} \right)^{n+1} N_n^m P_n^m(\cos \theta'(t)) e^{i\lambda'(t)} \quad (1.10)$$

The coefficients $T_{n,m}$ dependent only on the geocentric position \vec{R} of the sub-body point M that evolves with time. The ephemeris of the celestial bodies (principally the Moon and Sun) are well-known in advance at a high degree of accuracy, e.g., the latest NASA Jet Propulsion Laboratory (JPL) Planetary and Lunar Ephemerides DE414 ^{<1>}. The tidal potential can thus be directly computed for any point P on the Earth's surface at any time t .

The motions of the Moon and the Sun as observed in the geocentric coordinate system are predictable to high accuracy by harmonic functions of the periodic variations of their respective elliptical orbits. So the coefficients $T_{n,m}$ can also be expressed as a sum of harmonic functions, whose frequencies are linear combinations of the astronomical frequencies inherent to the orbital properties of the Moon and Sun. In such an expansion, the coefficients $T_{n,m}$ can be written as

$$T_{n,m}(t) = \sum_{k=1}^{K_{n,m}} H_{n,mk} e^{i(2\pi f_{n,m,k}t + \varphi_{n,m,k})} \quad (1.11)$$

where, for each degree n and order m , we sum $K_{n,m}$ sinusoids with specified real amplitudes H , frequencies f , and phases φ . The individual sinusoids are called 'tidal harmonics'. The frequency and phase of each tidal harmonic are the linear

¹ <ftp://ssd.jpl.nasa.gov/pub/eph/export>

combination of the six astronomical arguments as listed in Table 2.1.

$$2\pi f_{n,m,k}t + \varphi_{n,m,k} = d_1\tau + (d_2 - 5)s + (d_3 - 5)h + (d_4 - 5)p + (d_5 - 5)N' + (d_6 - 5)P' - \delta(n,m)\frac{\pi}{2} \quad (1.12)$$

$$\delta(n,m) = \begin{cases} 1 & \text{if } n+m \text{ odd} \\ 0 & \text{if } n+m \text{ even} \end{cases}$$

where d_i are integers that constitute (Doodson, 1921) argument number $d_1d_2d_3 \cdot d_4d_5d_6$.

The digit of Doodson number d_1 defines the tidal ‘species’ (0, 1 and 2 cycles/day),

d_1d_2 defines the tidal ‘group’ number (each separated by 1 cycle/month) and $d_1d_2d_3$

defines the tidal ‘constituent’ number (each separated by 1 cycle/year). The

corresponding numbers with 5 subtracted are called Cartwright-Tayler codes

(Cartwright and Tayler, 1971).

Table 2.1 Six astronomical arguments

<i>i</i>	Symbeol	Argument	Period
1	τ	Lunar day	24 h 50 m 28.3 s
2	s	Moon’s longitude: tropical month	27.3216 d
3	h	Sun’s longitude: solar year	365.2422 d
4	P	Lunar perigee	8.847 yr
5	N'	Lunar node	18.613 yr
6	P'	Solar perigee	20941 yr

Darwin (1883) first formulated the harmonic expansion of the tidal potential. He

also assigned symbols (e.g. M_2 , S_2 , and K_1) to the harmonic components contained

in this catalogue, which are still in use today. Doodson (1921) used analytic methods

to expand on the work of Darwin by including the harmonic components not already

determined by Darwin. Doodson, as mentioned above, effectively separated the

lunisolar tidal potential into harmonic series with frequencies determined by linear combinations of the six astronomical arguments (Table 2.1). Cartwright and Tayler (1971) and Cartwright and Edden (1973) used spectral techniques to expand the lunar tidal potential to degree-3 and the solar tide potential to degree-2. More extensive computations of the tidal potential and its harmonic decomposition have been driven by the very high precision available from the ephemerides and the needs for more precision for tidal data. Particular expansions are those of Bullesfeld (1985), Tamura (1987), Xi (1987), Hartmann and Wenzel (1995) and Roosbeek (1996). The latest is that of Kudryavtsev (2004), with 26753 harmonics. Table 2.2 lists the amplitudes and frequencies of the principal degree-2 tidal harmonics.

Table 2.2 The largest degree-2 tidal harmonics, sorted by size of each species (Agnew, 2007)

Darwin Symbol	Doodson Number	Frequency (cycles/day)	Amplitude (cm)	<i>H</i>
<i>Long-period tides</i>				
M_0, S_0	055.555	0.0000000	-31.459	
M_f	075.555	0.0732022	-6.661	
M_m	065.455	0.0362916	-3.518	
S_{sa}	057.555	0.0054758	-3.099	
N	055.565	0.0001471	2.793	
	075.565	0.0733493	-2.762	
M_{tm}	085.455	0.1094938	-1.275	
M_{sm}	063.655	0.0314347	-0.673	
M_{sf}	073.555	0.0677264	-0.584	
	085.465	0.1096409	-0.529	
<i>Diurnal tides</i>				
K_1	165.555	1.0027379	36.864	
O_1	145.555	0.9295357	-26.223	
P_1	163.555	0.9972621	-12.199	
Q_1	135.655	0.8932441	-5.021	
	165.565	1.0028850	5.003	

	145.545	0.9293886	-4.947
J_1	175.455	1.0390296	2.062
M_1	155.655	0.9664463	2.061
OO_1	185.555	1.0759401	1.128
ρ_1	137.455	0.8981010	-0.953
	135.645	0.8930970	-0.947
σ_1	127.555	0.8618093	-0.801
	155.455	0.9658274	0.741
	165.545	1.0025908	-0.730
	185.565	1.0760872	0.723
π_1	162.556	0.9945243	-0.713
$2Q_1$	125.755	0.8569524	-0.664
ϕ_1	167.555	1.0082137	0.525
<i>Semidiurnal tides</i>			
M_2	255.555	1.9322736	63.221
S_2	273.555	2.0000000	29.411
N_2	245.655	1.8959820	12.105
K_2	275.555	2.0054758	7.991
	275.565	2.0056229	2.382
	255.545	1.9321265	-2.359
ν_2	247.455	1.9008389	2.299
μ_2	237.555	1.8645472	1.933
L_2	265.455	1.9685653	-1.787
T_2	272.556	1.9972622	1.719
$2N_2$	235.755	1.8596903	1.602
ε_2	227.655	1.8282556	0.467
λ_2	263.655	1.9637084	-0.466

2.3 Solid Earth tides

The solid Earth's tidal deformation can be conventionally computed by convolving the tidal potential with tidal transfer functions for a nonrigid Earth (Agnew, 2007).

In simple case of a Spherical, Non-Rotating, Elastic, Isotropic and Oceanless (SNREIO) Earth, the displacements \vec{u} at the surface of the Earth ($r = a$) induced by the tidal potential Eq. (1.8) of degree n have the following form in spherical polar coordinates (θ, λ)

$$\bar{\mathbf{u}} = \begin{bmatrix} u_r \\ u_\theta \\ u_\lambda \end{bmatrix} = \begin{bmatrix} \frac{h_n V_n}{g} \\ \frac{l_n}{g} \frac{\partial V_n}{\partial \theta} \\ \frac{l_n}{g \sin \theta} \frac{\partial V_n}{\partial \lambda} \end{bmatrix} \quad (1.13)$$

where h_n and l_n are dimensionless parameters and are usually called Love or Shida numbers. The Love number h was introduced by Love (1909), and the Shida number l was introduced by Shida and Matsuyama (1912). For a spherical, non-rotating and elastic earth, the Love numbers are totally independent of order m and are nearly the same at all tidal frequencies.

For the real Earth, the effective Love numbers are dependent on site latitude and tidal frequency (Wahr, 1981; Mathews et al., 1995; Dehant et al., 1999). To attain an accuracy of better than 1 mm in modelling of site displacements, the following effects on the Love numbers have to be considered. The Earth's ellipticity and Coriolis force due to Earth rotation couple the response to forcing of degree n to spherical harmonics of other degrees, and spheroidal to toroidal modes of deformation. As a result, the Love numbers become slightly latitude dependent and small order m dependent.

Another important feature to be taken into account is the Nearly Diurnal Free Wobble (MDFW) resonance. Its frequency falls within the diurnal band, which causes a resonant response in the Love numbers near 1 cycle/day. The resonance in the deformation due to OTL also influences the values of the Love numbers. In the

long-period tidal band, the anelasticity of the mantle further leads to corrections to the elastic Earth Love numbers.

Instead of two Love numbers h and l as used for a spherical Earth, Mathews et al. (1995) used seven Love numbers $(h^{(0)}, h^{(2)}, h')$ and $(l^{(0)}, l^{(1)}, l^{(2)}, l')$ to describe the surface tidal displacements of an ellipsoidal Earth. The surface displacements \vec{u} due to a tidal term of frequency f can then be expressed in terms of frequency- and latitude-dependent Love numbers as (Mathews et al., 1995; Dehant et al., 1999)

$$\begin{aligned} \vec{u} = H_f e^{i\varphi_f} \left\{ \left[h(\theta) Y_{n,m} + h' Y_{n-2,m} \right] \hat{e}_r \right. \\ \left. + \left[l(\theta) \frac{\partial Y_{n,m}}{\partial \theta} + l^{(1)} P_1(\cos \theta) \frac{m}{\sin \theta} Y_{n,m} + l' \frac{m}{\sin \theta} Y_{n-1,m} \right] \hat{e}_\theta \right. \\ \left. + \left[l(\theta) \frac{m}{\sin \theta} Y_{n,m} + l^{(1)} P_1(\cos \theta) \frac{\partial Y_{n,m}}{\partial \theta} + l' \frac{\partial Y_{n-1,m}}{\partial \theta} \right] i \hat{e}_\lambda \right\} \end{aligned} \quad (1.14)$$

where H_f is the amplitude of the tide term of frequency f as defined in Eq. (1.11), h' and l' are independent of site's position, and $h(\theta)$ and $l(\theta)$ depend on colatitude θ as

$$\begin{aligned} h(\theta) &= h^{(0)} + h^{(2)} P_2(\cos \theta) \\ l(\theta) &= l^{(0)} + l^{(2)} P_2(\cos \theta) \end{aligned} \quad (1.15)$$

Explicit expressions for the components of the tidal displacements can be derived from Eq. (1.14). Since the effect of latitude dependence of Love numbers due to degree-3 or higher-degree tides are negligible, the seven Love number parameters need to be used only for degree-2 tides in practice. The components of the tidal displacements of degree-2 can be explicitly expressed as

For a long-period tide of frequency f :

$$\begin{aligned} \bar{u} = \sqrt{\frac{5}{4\pi}} H_f \left\{ \left[h(\theta) \left(\frac{3}{2} \sin^2 \theta - \frac{1}{2} \right) + \sqrt{\frac{4\pi}{5}} h' \right] \cos \varphi_f \hat{e}_r \right. \\ \left. + 3l(\theta) \sin \theta \cos \theta \cos \varphi_f \hat{e}_\theta \right. \\ \left. + \left[3l^{(1)} \sin^2 \theta - \sqrt{\frac{4\pi}{5}} l' \right] \cos \theta \sin \varphi_f \hat{e}_\lambda \right\} \end{aligned} \quad (1.16)$$

For a diurnal tide of frequency f :

$$\begin{aligned} \bar{u} = -\sqrt{\frac{5}{24\pi}} H_f \left\{ 3h(\theta) \sin \theta \cos \theta \sin(\varphi_f + \lambda) \hat{e}_r \right. \\ \left. + \left[3l(\theta) \cos 2\theta - 3l^{(1)} \sin^2 \theta + \sqrt{\frac{24\pi}{5}} l' \right] \sin(\varphi_f + \lambda) \hat{e}_\theta \right. \\ \left. + \left[\left(3l(\theta) - \sqrt{\frac{24\pi}{5}} l' \right) \sin \theta - 3l^{(1)} \sin \theta \cos 2\theta \right] \cos(\varphi_f + \lambda) \hat{e}_\lambda \right\} \end{aligned} \quad (1.17)$$

For a semidiurnal tide of frequency f :

$$\begin{aligned} \bar{u} = \sqrt{\frac{5}{96\pi}} H_f \left\{ 3h(\theta) \cos^2 \theta \cos(\varphi_f + 2\lambda) \hat{e}_r \right. \\ \left. - 6 \left[l(\theta) + l^{(1)} \right] \sin \theta \cos \theta \cos(\varphi_f + 2\lambda) \hat{e}_\theta \right. \\ \left. - 6 \left[l(\theta) + l^{(1)} \sin^2 \theta \right] \cos \theta \sin(\varphi_f + 2\lambda) \hat{e}_\lambda \right\} \end{aligned} \quad (1.18)$$

The expressions of Eqs. (1.16)-(1.18) assume that the Love number parameters are all real. Generalisation to the case of complex parameters is done simply by making the following replacements for the combinations $L \cos(\varphi_f + m\lambda)$ and $L \sin(\varphi_f + m\lambda)$, wherever they occur in those equations

$$\begin{aligned} L \cos(\varphi_f + m\lambda) &\rightarrow L^R \cos(\varphi_f + m\lambda) - L^I \sin(\varphi_f + m\lambda) \\ L \sin(\varphi_f + m\lambda) &\rightarrow L^R \sin(\varphi_f + m\lambda) + L^I \cos(\varphi_f + m\lambda) \end{aligned} \quad (1.19)$$

where L is a generic symbol for $(h^{(0)}, h^{(2)}, h')$ and $(l^{(0)}, l^{(1)}, l^{(2)}, l')$, and L^R and L^I stand for their respective real and imaginary parts.

The numerical values of these frequency-dependent Love numbers $(h^{(0)}, h^{(2)}, h')$ and $(l^{(0)}, l^{(1)}, l^{(2)}, l')$ can be obtained from Table 7.4 in McCarthy and Petit (2004). Computation of site displacements by summation of Eqs. (1.16)-(1.18) over the tidal constituents is inefficient because a very large number of tidal constituents have to be included. IERS Conventions 2003 (McCarthy and Petit, 2004) adopt a two-step procedure proposed by Mathews et al. (1997) for reasons of computational efficiency. By adopting nominal values independent of frequency for the Love number parameters in the first step, one can make use of relatively simple formulas in the time domain for the full degrees 2 and 3 tidal potential. Computation of corrections to take account of the frequency dependence of the Love numbers is then carried out as a second step. The full scheme of computation is described in (McCarthy and Petit, 2004). A FORTRAN 77 program for computing all these corrections is available at <ftp://tai.bipm.org/iers/convupdt/chapter7>. The accuracy of the solid Earth tidal displacement corrections generated using IERS Conventions 2003 is considered better than 1 mm.

2.4 Basic theory for computing surface loading

The circulation and redistribution of the fluid mass (oceans, atmosphere, and

² <ftp://tai.bipm.org/iers/convupdt/chapter7>

continental water) over the surface of the Earth cause the deformation of the underlying solid Earth, which is called surface mass loading. To model the loading effects, we require surface mass data for all relevant loads. The surface mass loads can then be convolved with the Earth's response either in the "wave number domain" or the "space domain" (Agnew, 2007). Therefore, the loading responses of the solid Earth to surface mass loads are usually computed in the following two ways:

1) Spherical harmonic approach: the surface mass loads are expanded into a series of scalar spherical harmonics. The Earth's deformation response can be calculated using the spherical harmonic series of the surface load and multiplying each the degree- n terms in the load potential by the corresponding load Love number (Agnew, 2007; Schrama, 2005).

2) Green's function approach: the response of the solid Earth to an arbitrary surface mass load can be computed in space domain via a surface convolution of the surface mass load with an appropriate Green's function associated with the elasticity of the Earth (Agnew, 2007; Schrama, 2005).

2.4.1 The load potential

Consider a spherical solid Earth of mean radius a , plus surface masses which are free to redistribute in a thin surface layer ($\ll a$). Formally, the density of the surface mass loads can be simply expressed as the equivalent height of a column of seawater $H(\theta', \lambda')$ which is a function of geographical position (θ', λ') . The surface mass

load can be expressed as a spherical harmonic expansion

$$H(\theta', \lambda') = \sum_{n=0}^{\infty} \sum_{m=-n}^n H_{nm} Y_{nm}(\theta', \lambda') \quad (1.20)$$

where the Y_{nm} are as in Section 2.2, and the coefficients H_{nm} are

$$H_{nm} = \int_{\Omega} H(\theta', \lambda') Y_{nm}^* d\Omega \quad (1.21)$$

The mass distribution H causes an incremental gravitational potential on the surface of the Earth, which is called the “load potential”. This load potential is given by the integral over the surface of potential function times H

$$V^L(\theta, \lambda) = G\rho_s a^2 \int_{\Omega} \frac{H(\theta', \lambda')}{r} d\Omega \quad (1.22)$$

with ρ_s the density of surface mass, r is the distance from the location (θ, λ) to the mass at (θ', λ') , and, may be expressed in terms of angular distance Δ

$$\begin{aligned} \frac{1}{r} &= \frac{1}{2a \sin(\Delta/2)} = \frac{1}{a} \sum_{n=0}^{\infty} P_n(\cos \Delta) \\ &= \frac{1}{a} \sum_{n=0}^{\infty} \sum_{m=-n}^n \frac{4\pi}{2n+1} Y_{nm}(\theta', \lambda') Y_{nm}^*(\theta, \lambda) \end{aligned} \quad (1.23)$$

Using the last expression in (1.23) and the spherical harmonic expansion (1.20) in the load potential (1.22) yields

$$V^L(\theta, \lambda) = \sum_{n=0}^{\infty} V_n(\theta, \lambda) = G\rho_s a \sum_{n=0}^{\infty} \sum_{m=-n}^n \frac{4\pi}{2n+1} H_{nm} Y_{nm}(\theta, \lambda) \quad (1.24)$$

2.4.2 Spherical harmonic approach

According to load Love number theory (Munk and Macdonald, 1960), the surface displacement $u_r(\theta, \lambda)$ in the vertical component and $u_l(\theta, \lambda)$ in the horizontal component are defined by

$$\begin{aligned} u_r(\theta, \lambda) &= \sum_{n=0}^{\infty} h'_n \frac{V_n(\theta, \lambda)}{g} \\ u_l(\theta, \lambda) &= \sum_{n=1}^{\infty} l'_n \frac{\nabla V_n(\theta, \lambda)}{g} \end{aligned} \quad (1.25)$$

where the h'_n and l'_n are called degree- n load Love numbers, with the prime used to distinguish Love numbers used in loading theory from those used in body tidal theory. The surface gradient operator is defined as $\nabla = \hat{e}_\theta \partial_\theta + \hat{e}_\lambda (1/\cos \theta) \partial_\lambda$ where \hat{e}_θ and \hat{e}_λ are unit vectors in the north and east components, respectively. Only the degree-1 Love numbers h'_1 and l'_1 are relevant to the reference frame (Blewitt, 2003).

To compute the surface loading deformation, we substitute Eq. (1.24) into Eq. (1.25)

and obtain the following expressions

$$\begin{aligned} u_r(\theta, \lambda) &= \frac{G\rho_s a}{g} \sum_{n=0}^{\infty} \sum_{m=-n}^n \frac{4\pi h'_n}{2n+1} H_{nm} Y_{nm}(\theta, \lambda) \\ &= \frac{\rho_s}{\rho_E} \sum_{n=0}^{\infty} \sum_{m=-n}^n \frac{3h'_n}{2n+1_n} H_{nm} Y_{nm}(\theta, \lambda) \\ u_l(\theta, \lambda) &= \frac{\rho_s}{\rho_E} \sum_{n=0}^{\infty} \sum_{m=-n}^n \frac{3l'_n}{2n+1_n} H_{nm} \nabla Y_{nm}(\theta, \lambda) \end{aligned} \quad (1.26)$$

where ρ_E is the mean density of the solid Earth.

We usually require many high-degree terms in the series of Eq. (1.26) to converge. The problem associated with truncation of an the infinite harmonic series, which is known as Gibbs's phenomenon (Hewitt and Hewitt, 1979), has to be accounted for. The main advantage of this method is that it provides the complete displacement field over the whole Earth. In the past, this approach has been adopted by some researchers (Ray and Sanchez, 1989; Mitrovica et al., 1994b; Le Meur and Hindmarsh, 2000) for loading calculations. Recently, the spherical harmonic approach has also been widely applied to the inversion of surface mass loads from geodetic displacements (Blewitt et al., 2001; Wu et al., 2003; Wu et al., 2006; Clarke et al., 2007) and the interaction between loading dynamics and the terrestrial reference frame (Blewitt, 2003; Dong et al., 2003; Lavallee et al., 2006).

2.4.3 Green's function approach

If we compute the crustal loading at a particular place, the most efficient approach is to multiply the surface mass model by a Green's function (Farrell, 1972) which gives the Earth's response to a point load, integrating over the whole mass's area. That is, this method works in the space domain rather than the in the wave number domain as shown in previous section. Nonetheless, the Green's function approach is fundamentally based on load Love number theory. Green's function approach has other advantages, such as the ability to combine different surface mass models easily, conduct the Gibbs's phenomenon efficiently, and include more detail close to the point of observation.

We combine Eqs. (1.22) and (1.25) using the sum in $P_n(\cos \Delta)$ in Eq. (1.23) and give the following convolution integral

$$u(\theta, \lambda) = \rho_s a^2 \int_{\Omega} G(\Delta) H(\theta', \lambda') d\Omega \quad (1.27)$$

Here the Green's function $G(\Delta)$ for the vertical and horizontal displacements is

$$\begin{aligned} G_r(\Delta) &= \frac{a}{M} \sum_{n=0}^{\infty} h'_n P_n(\cos \Delta) \\ G_l(\Delta) &= \frac{a}{M} \sum_{n=1}^{\infty} l'_n \frac{\partial P_n(\cos \Delta)}{\partial \Delta} \end{aligned} \quad (1.28)$$

As the Green's function Eq. (1.28) is formed by the infinite summation of the load Love numbers, it is necessary to truncate up to a given degree N . When n gets large enough, h'_n and nl'_n , become constant. So we can define the limit values by Farrell (1972)

$$\lim_{n \rightarrow \infty} \begin{bmatrix} h'_n \\ nl'_n \end{bmatrix} = \begin{bmatrix} h'_\infty \\ l'_\infty \end{bmatrix} \quad (1.29)$$

Substituting Eq. (1.29) into Eq. (1.28) gives

For the vertical displacement:

$$\begin{aligned} G_r(\Delta) &= \frac{ah'_\infty}{M} \sum_{n=0}^{\infty} P_n(\cos \Delta) + \frac{a}{M} \sum_{n=0}^{\infty} (h'_n - h'_\infty) P_n(\cos \Delta) \\ &= \frac{ah'_\infty}{2M \sin(\Delta/2)} + \frac{a}{M} \sum_{n=0}^N (h'_n - h'_\infty) P_n(\cos \Delta) \end{aligned} \quad (1.30)$$

For the horizontal displacement:

$$\begin{aligned}
 G_l(\Delta) &= \frac{al'_\infty}{M} \sum_{n=1}^{\infty} \frac{1}{n} \frac{\partial P_n(\cos \Delta)}{\partial \Delta} + \frac{a}{M} \sum_{n=1}^{\infty} (nl'_n - l'_\infty) \frac{1}{n} \frac{\partial P_n(\cos \Delta)}{\partial \Delta} \\
 &= -\frac{al'_\infty}{2M} \frac{\cos(\Delta/2)[1 + 2\sin(\Delta/2)]}{\sin(\Delta/2)[1 + \sin(\Delta/2)]} + \frac{a}{M} \sum_{n=1}^N (nl'_n - l'_\infty) \frac{1}{n} \frac{\partial P_n(\cos \Delta)}{\partial \Delta} \quad (1.31)
 \end{aligned}$$

The new sum will converge much more rapidly than the infinite sum in Eq. (1.28).

Several numerical methods are now applied to further accelerate the convergence (Farrell, 1972; Scherneck, 1991; Agnew, 1997; Schrama, 2005). The Green's functions based on the Gutenberg-Bullen A model, which are tabulated by Farrell (1972), are most prevalent for the calculation of tidal loading. Jentzsch (1997) listed a set of Green's functions derived from the Preliminary Reference Earth Model (DREM) (Dziewonski, Anderson, 1981). Pagiatakis (1990) developed the Green's functions for a self-gravitating, layered, compressible, viscoelastic, anisotropic, and rotating, with a solid inner core and fluid outer core. The differences between different Green's functions produced by different elastic Earth models are small, usually less than 2%.

2.5 Ocean tide loading

Ocean tides cause the redistribution of the global seawater mass. The elastic response of the solid Earth to ocean tides is known as Ocean Tide Loading (OTL). The vertical displacement due to OTL may reach over 10 cm. This section deals with the modelling of OTL displacements.

2.5.1 Ocean tide models

As mentioned in section 2.4, global ocean tide models are needed to calculate the OTL effects. The ocean tides can be modelled as a harmonic series of the main tidal constituents, each of which have their own frequencies, amplitudes and phases. Global ocean tide models are usually provided for the main tidal constituents, e.g. the semidiurnal tides M_2 , S_2 , N_2 , K_2 , and the diurnal tides K_1 , O_1 , P_1 , Q_1 . Since the launch of satellite altimeter TOPEX/Poseidon (T/P) with its unprecedented precise sea surface height data, ocean tide modelling has now experienced a significant improvement especially in the deep ocean (Shum et al., 1997). There is still a large deficiency in modelling shallow water tides. The space gravity observations, i.e., CHAMP and GRACE, are expected to help further improve global ocean tide models (Ray et al., 2001; Han et al., 2007).

Global tide models generally fall into three categories: (1) empirical models only based on the direct tidal observational data; (2) hydrodynamic models which employ the hydrodynamic modelling approach to represent the ocean tides; (3) assimilation models which combine these two approaches. The leading global ocean tide models available at the automatic loading service ³ are listed in Table 2.3, and a brief description of these models is given below. Most of the models assimilate tide gauge and satellite altimetry data.

³ <http://www.oso.chalmers.se/%7Eloading/index.html>

Table 2.3 Global ocean tide models from the automatic loading service

Model	Type ^a	Resolution ^b	Reference
Schwiderski	hydrodyn. + TG	1° × 1°	Schwiderski (1980)
CSR3.0	T/P	1° × 1°	Eanes (1994)
CSR4.0	T/P	0.5° × 0.5°	Eanes and Shuler (1999)
TPXO.5	hydrodyn. + T/P	0.5° × 0.5°	Egbert et al. (1994)
TPXO6.2	hydrodyn. + T/P	0.25° × 0.25°	Egbert and Erofeeva (2002)
TPXO7.0, TPXO7.1	hydrodyn. + T/P	0.25° × 0.25°	Egbert and Erofeeva (2002)
FES94.1	Num.	0.5° × 0.5°	Le Provost et al. (1994)
FES95.2	Num. + T/P	0.5° × 0.5°	Le Provost et al. (1998)
FES98	Num. + TG	0.25° × 0.25°	Lefevre et al. (2000)
FES99	Num. + TG and T/P	0.25° × 0.25°	Lefevre et al. (2002)
FES2004	Num. + T/P	0.125° × 0.125°	Lyard et al. (2006)
GOT99.2b	T/P	0.5° × 0.5°	Ray (1999)
GOT00.2	T/P+ERS	0.5° × 0.5°	Ray (1999)
GOT4.7	Multi-mission altimetry	0.5° × 0.5°	Ray (1999)
EOT08a	Multi-mission altimetry	0.125° × 0.125°	Savcenko and Bosch (2008)
AG06a	Multi-mission altimetry	0.25° × 0.25°	Andersen et al. (2006)
NAO.99b	num. + T/P	0.5° × 0.5°	Matsumoto et al. (2000)

^a Hydrodyn., Hydrodynamic model; TG, tide gauge data assimilated; T/P, TOPEX/Poseidon altimetry data assimilated; ERS, ERS altimetry data assimilated.

^b Latitude × longitude.

The Schwiderski (1980) model used an interpolation scheme in order to constrain a priori hydrodynamic model to a large number of tide gauge data. This model has been used as a standard in geophysical research before the satellite altimetry data was available in the 1990s.

The CSR3.0 ocean tide model (Eanes, 1994) developed by The University of Texas uses a response analysis of 2.4 years of T/P data to apply long wavelength adjustments to the FES94.1 hydrodynamic model (Le Provost et al., 1994). CSR4.0 is an update of this model using a longer T/P data set. For the tidal values outside the $\pm 66^\circ$ latitudes covered by the T/P satellite, these two models are equal to FES94.1.

TPXO.5 through TPXO7.1 (Egbert et al., 1994; Egbert and Erofeeva, 2002) are four latest versions of a global model of ocean tides, which best-fits, in a least-squares sense, the Laplace tidal equations and along track averaged data from T/P and Jason (on T/P tracks since 2002) obtained with OTIS-OSU Tidal Inversion Software ^{<4>}. The methods used to compute the model are described in detail by Egbert et al. (1994) and further by Egbert and Erofeeva (2002). Each version of the TPXO model is of better quality compared to the earlier versions, due to some improvements in the following several aspects: (a) it assimilates longer satellite time-series; (b) more data sites are included into assimilation; (c) bathymetry is improving from version to version; (d) resolution of global and local grids is improving from version to version.

FES94.1 (Le Provost et al., 1994) is a pure hydrodynamic tide model tuned to fit tide gauges globally. It has been calculated on a finite element of 200 km in the deep ocean reducing to 10 km in coastal area and has been transformed on to a regular 0.5° grid for its distribution. In FES95.2 (Le Provost et al., 1998), the tides in the Arctic were improved and TOPEX/Poseidon data has been used to adjust the long-wavelength behaviour of FES94.1. FES98 (Lefevre et al., 2000) is again a pure hydrodynamic model and has assimilated approximately 700 coastal, island and deep ocean tide gauge data. Another improvement is the fact that it has been

⁴ <http://www.coas.oregonstate.edu/research/po/research/tide/otis.html>

computed on a global grid instead of computing the ocean tides in a few ocean basins separately and then gluing the solutions together. FES99 (Lefevre et al., 2002) is an update of FES98 and has T/P data assimilated into it. FES2004 (Lyard et al., 2006) is a most recent version of the FES series. FES2004 has a higher resolution of 0.125° and has a quite good fit to the coastline.

GOT99.2b and GOT00.2 (Ray, 1999) are again long wavelength adjustments of FES94.1 using T/P data and are given on a 0.5 by 0.5 degree grid. GOT99.2b also becomes equal to FES94.1 outside the 66° latitudes. GOT00.2 is different from FES94.1 in the polar region because it uses ERS1/2 data in the assimilation process. The recently revised GOT4.7 model assimilates T/P, Jason-1, ERS and GFO altimetry data. The new version significantly improves variance reduction (1-2 cm accuracy in the open ocean), especially for the larger coastal tides.

EOT08a (Savcenko and Bosch, 2008) is derived by empirical analysis of 13 years multi-mission altimetry data (T/P, Jason-1, ERS1, ERS2, ENVISAT, and GFO). The resolution of $0.125^\circ \times 0.125^\circ$ is identical with FES2004 which was used as reference model for the residual tide analysis.

AG06a is an update of the AG95 global ocean model (Andersen et al., 2006). AG06a is also an adjustment of the FES94.1 model to multi-mission altimetry (T/P, Jason-1, ERS1, ERS2, ENVISAT, and GFO). Its resolution is 0.25 by 0.25 degrees, including 12 major tidal constituents.

NAO.99b is based on the same hydrodynamics as the Schwiderski (1980) model but assimilates tide gauge and T/P data into it. This model includes 16 major constituents with a spatial resolution of $0.5^\circ \times 0.5^\circ$. Benefiting from fine-scale along-track tidal analysis of T/P data, NAO.99b is more accurate in shallow waters than the other two models CSR4.0 and GOT99.2b (Matsumoto et al., 2000).

2.5.2 Computational methods

As previously mentioned, the OTL displacements due to a given tidal harmonic can be computed by either the spherical harmonic or Green's function approach. In practice, the accuracy of the computation with the spherical harmonic approach is generally less than that of the Green's function approach (Agnew, 2007). So all OTL programs usually adopt the Green's function method which performs the convolution directly, either over the grid of ocean cells (perhaps more finely divided near the load) or over a radial grid. Three different OTL software packages are widely used and freely distributed, namely SPOTL (Agnew, 1997) available at ⁵, OLFG/OLMPP (Scherneck, 1991) available at ⁶ and GOTIC2 (Matsumoto et al., 2000) available at ⁷. The main characteristics of each program are discussed in Bos and Baker (2005). In this research, the SPOTL software is used to compute the

⁵ <http://igpphelp.ucsd.edu/~agnew/spotlmain.html>

⁶ <http://www.oso.chalmers.se/~hgs/README.html>

⁷ http://www.miz.nao.ac.jp/staffs/nao99/index_En.html

OTL displacements.

The accuracy of modelled OTL displacements depends on the ocean tide model, Green's function, coastline and the numerical scheme of loading computation (Schrama, 2005; Penna et al., 2008). The differences of OTL displacements derived from different Green's functions are small, less than 2%. Numerical errors in the convolution scheme are about 2~5%. Currently, the largest contributors to the uncertainty of OTL displacements are still the errors from ocean tide models.

Following the above computation, the OTL displacements in terms of amplitudes and phases are generally obtained only for some main tidal constituents. The 11 main constituents considered in the IERS Conventions 2003 (McCarthy and Petit, 2004) are the semidiurnal waves M_2 , S_2 , N_2 , K_2 , the diurnal waves K_1 , O_1 , P_1 , Q_1 , and the long-period waves M_f , M_m , and S_{sa} . Therefore, the effects of the waves with very small amplitudes, for which no models exist, should be considered for accurate OTL corrections. For simple instance, if the modulation with the 18.6 year period of the lunar node is included, the site displacements due to OTL are computed by McCarthy and Petit (2004)

$$\Delta c_k = \sum_{j=1}^{11} f_j A_{k,j} \cos(\omega_j t + \chi_j(t_0) + \mu_j - \Phi_{k,j}) \quad (1.32)$$

where $A_{k,j}$ and $\Phi_{k,j}$ denote the amplitude and phase of the tidal constituent j in the local north, east and vertical ($k = 1, 2, 3$) components, respectively. χ_j is the astronomical argument at some reference time t_0 , and ω_j is the constituent angular

frequency. f_j and μ_j are used to account for the modulating effects of the lunar node.

Instead of using the nodal modulations of f and μ , a more fully interpolated loading tide spectrum is expected to give better precision (Le Provost et al., 1991). Neglecting the minor tides and nodal modulations may lead to errors of several mm, up to 5 mm RMS at high latitudes (McCarthy and Petit, 2004).

Additional contributions to OTL displacements come from the dependence of the load Love numbers due to the NDFW in the diurnal tidal band. The effect of this dependence has been considered by increasing the body tide Love numbers as explained in Section 2.3 (Wahr and Sasao, 1981).

A FORTRAN program (`hardisp.f`) provided by D. Agnew has been recommended in the IERS Conventions 2003 to compute the OTL displacements for any given site using the amplitudes and phases of the 11 main tides in the BLQ format. This program considers a total of 141 tidal constituents whose amplitudes and phases are founded by spline interpolation of the tidal admittance based on the 11 main tides. A precision of about 1% is expected. The code can be downloaded freely from [⟨?⟩](#).

2.5.3 Geocentre motion due to ocean tides

When the solid Earth and the fluid masses (oceans, atmosphere, and continental water) are considered to be a system without any external forces on it, then the centre of mass of the combined solid Earth and fluid masses system (CM) will

remain fixed in space. Since a phenomenon, such as ocean tides, causes redistribution of fluid masses, the centre of mass of the fluid masses will move periodically and must be compensated by an opposite motion of the centre of mass of the solid Earth (CE), which is generally called “geocentre motion”. The sites, being fixed to the solid Earth, are subject to this geocentre motion. Satellite range measurements, such as Satellite Laser Ranging (SLR) and GPS, are fixed in space and are affected by geocentre motion. Conventional geodetic techniques are insensitive to this motion.

As mentioned in Section 2.4, only the degree-1 load Love numbers are relevant to the reference frame (Blewitt, 2003). So we can use the Green’s functions in different reference frames to directly calculate the surface loading in the corresponding reference frame. Alternatively, we can use the centre of mass coefficients for different ocean tide models provided by Scherneck at ⁸. According to this method, the geocentre-corrected OTL coefficients for each tidal constituent j are obtained by

$$\begin{bmatrix} Z_{n,j}^{(c)} \\ Z_{e,j}^{(c)} \\ Z_{u,j}^{(c)} \end{bmatrix} = \begin{bmatrix} A_{n,j} \exp(i\Phi_{n,j}) \\ A_{e,j} \exp(i\Phi_{e,j}) \\ A_{u,j} \exp(i\Phi_{u,j}) \end{bmatrix} + \begin{bmatrix} -\sin \theta \cos \lambda & -\sin \theta \sin \lambda & \cos \theta \\ -\sin \lambda & \cos \lambda & 0 \\ \cos \theta \cos \lambda & \cos \theta \sin \lambda & \sin \theta \end{bmatrix} \begin{bmatrix} C_{x,j} \\ C_{y,j} \\ C_{z,j} \end{bmatrix} \quad (1.33)$$

$[C_{x,j} \ C_{y,j} \ C_{z,j}]$ denote coefficients for the tidally induced geocentre motion. Table 2.4 lists the coefficients for geocentre tides derived from the ocean tide model FES2004.

⁸ <http://www.oso.chalmers.se/~loading/CMC/>

Table 2.4 Coefficients for the tidally induced geocentre motion derived from the ocean tide model FES2004 <⁸>

Tide	$C_{x,j}$ (mm)		$C_{y,j}$ (mm)		$C_{z,j}$ (mm)	
	Re	Im	Re	Im	Re	Im
M ₂	-1.372	0.821	1.148	0.230	-1.266	-1.430
S ₂	-0.534	-0.316	-0.051	0.282	-0.178	-0.573
N ₂	-0.271	0.198	0.260	-0.143	-0.324	-0.290
K ₂	-0.112	-0.011	-0.016	0.124	-0.118	-0.153
K ₁	-1.854	-0.864	-0.910	-1.782	-1.137	4.484
O ₁	-1.399	-0.230	-0.889	-0.650	-0.168	2.970
P ₁	-0.614	-0.291	-0.293	-0.575	-0.365	1.494
Q ₁	-0.278	-0.029	-0.217	-0.042	0.031	0.455
M _f	-0.221	0.415	-0.102	0.082	-0.506	-0.073
M _m	0.047	0.184	-0.007	0.013	-0.279	0.021
S _{sa}	0.137	0.035	-0.024	0.000	-0.149	0.003

2.6 Atmospheric tide loading

Atmospheric tides are global-scale surface pressure oscillations at diurnal and higher harmonics (Chapman and Lindzen, 1970). Atmospheric tides, unlike solid Earth tides and ocean tides, are excited primarily by the Sun's heating of the atmosphere. The gravitational forces of the Moon and Sun have only minor effects on atmosphere dynamics. The atmospheric tides are greatest at the equator and at some continental locations, with a diurnal S₁ component of 0.3 to 0.5 mb, and a semidiurnal S₂ component of 1-2 mb, for a total range of 3 to 4 mb daily. Towards the poles, the atmospheric tides are not generally discernible.

These atmospheric tides also load the solid Earth and the resulting deformation should be precisely modelled. For the atmospheric tide loading calculation, globally well-resolved barometric tides S₁ (p) and S₂ (p) are required. However, the global

representation of these tidal signals is difficult due to model deficiency and data noise. Comparison of global barometric tides derived from the European Centre for Medium-Range Weather Forecasts (ECMWF) (Molteni et al., 1996) and National Center for Atmospheric Research Reanalysis (NCEPR) (Kalnay et al., 1996) global analyses with the meteorological site data reveals significant inadequacies in the representation of $S_2(p)$ in both of the reanalyses (Ray, 2001). Similar detailed comparisons for $S_1(p)$ are missing, but significant discrepancies between theoretical and observations have been noted (Braswell and Lindzen, 1998; Ray, 1998). Recently, Ray and Ponte (2003) developed a superior $S_1(p)$ and $S_2(p)$ tidal model which has been recommended as the conventional atmospheric tidal model ⁹. The model is derived from the ECMWF operational global surface pressure fields using a procedure outlined by van den Dool et al. (1997). T. M. van Dam and R. D. Ray provided an online atmospheric tide loading calculator based on the proposed IERS conventions, which is available at ⁹. Another atmospheric tide loading service developed by L. Petrov can also be obtained from ¹⁰.

Figure 2.2 shows the amplitudes and phases of the predicted vertical displacements from the S_1 and S_2 atmospheric tides. For the S_1 tide, maximum deformation occurs in low latitudes over large continental land masses, with displacements of order 2 mm peak-to-peak. For the S_2 tide, deformation is more regular, with maximum

⁹ <http://www.ecgs.lu/atm/>

¹⁰ <http://gemini.gsfc.nasa.gov/aplo/>

deformation of order 3 mm peak-to-peak along the equator. Horizontal deformations are a factor of ten smaller in magnitude. It is worth noting that both of these tides have significant seasonal modulations. Moreover, the atmospheric tides over the oceans induce a highly dynamic ocean response. The response at S_2 is already included in most models of the S_2 ocean tide. The response at S_1 has been generally ignored, but recent modelling efforts (Ray and Egbert, 2004) can now be adopted to account for this effect.

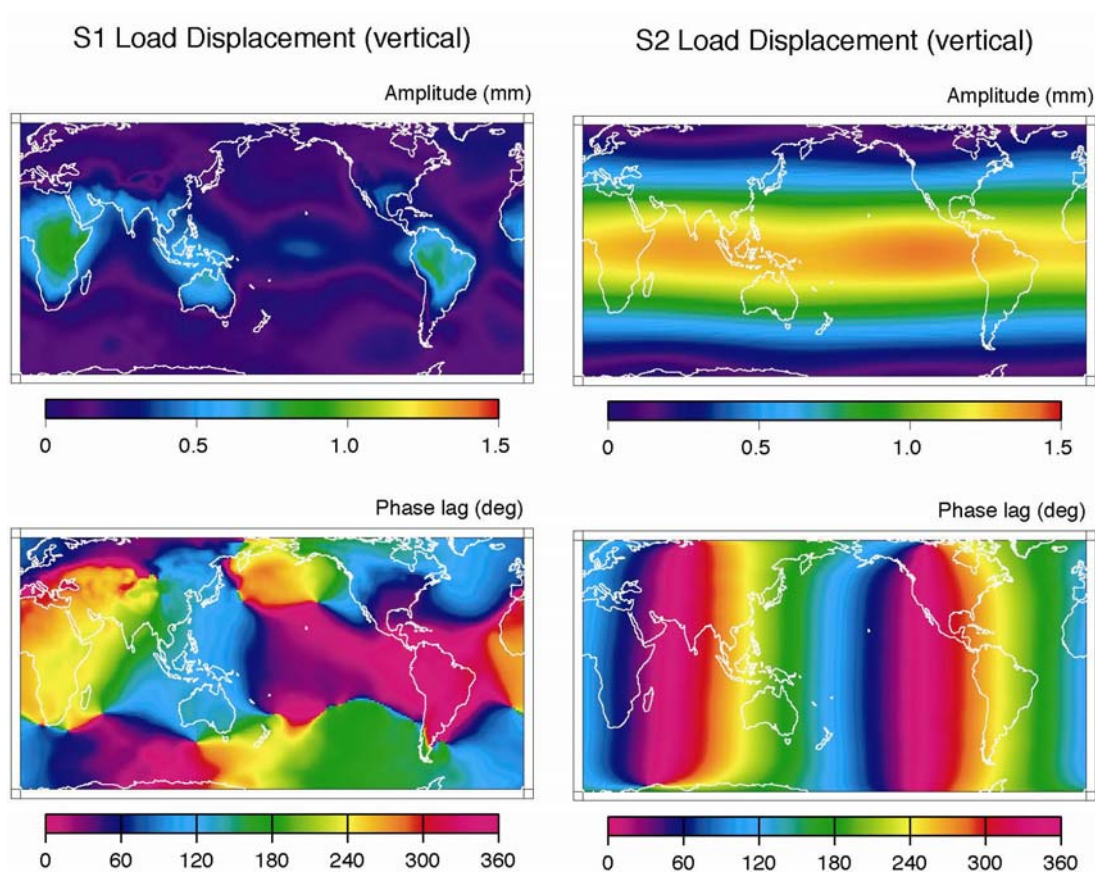


Figure 2.2 Vertical displacements of the S_1 and S_2 tides derived from the Ray and Ponte (2003) model, using Farrell's (1972) elastic Green's functions in the centre of earth frame (CE). Source: van Dam ⁹.

2.7 Pole tide

The centrifugal force associated with variations in the Earth's rotation rate and in the geocentric position of the rotation axis (polar motion) causes the Earth to deform. This deformation is referred to as the pole tide. The deformation caused by variation of the rotation rate is negligible compared to that caused by polar motion. Polar motion is dominated by two periodic variations: an elliptical motion at an annual period (the annual wobble) and an almost circular motion at a period of 14 months (the Chandler wobble). The induced deformation is linear in the amplitudes of polar motion. So these two periodic components also dominate the time-dependent deformation. The pole tide can be derived by applying classical Love number theory (see Section 2.3) to the centrifugal potential.

Let us define a right-handed coordinates system as follows: \hat{z} is oriented along the Earth's mean rotation axis, \hat{x} is oriented along the Greenwich meridian, and \hat{y} is orthogonal to the \hat{x} and \hat{z} axes and in the plane of the 90°E meridian. The instantaneous position of the Earth's rotation is specified by the vector

$$\vec{\Omega} = \Omega_0 [m_1 \hat{x} + m_2 \hat{y} + (1 + m_3) \hat{z}] \quad (1.34)$$

where Ω_0 is the mean angular velocity of the Earth's rotation, the quantities m_1 and m_2 describe polar motion, and m_3 describes the change in the rotation rate.

The centrifugal potential caused by the Earth's rotation at a point \vec{r} is

$$V = \frac{1}{2} (\vec{\Omega} \times \vec{r})^2 = \frac{1}{2} [r^2 |\Omega|^2 - (\vec{r} \cdot \vec{\Omega})^2] \quad (1.35)$$

The m_3 term in Eq. (1.35) causes vertical displacements which are below the millimetre level (Wahr, 1985) and is neglected in IERS Conventions 2003. Thus the m_1 and m_2 terms give a first order perturbation in the potential of

$$V(r, \theta, \lambda) = \frac{\Omega^2 r^2}{2} \sin 2\theta (m_1 \cos \lambda + m_2 \sin \lambda) \quad (1.36)$$

The vertical displacement S_r and the horizontal displacements S_θ and S_λ due to the centrifugal potential V can be obtained using the formalism of tidal Love numbers (see Section 2.3)

$$\begin{aligned} S_r &= \frac{h_2}{g} V(r, \theta, \lambda) \\ S_\theta &= \frac{l_2}{g} \partial_\theta V(r, \theta, \lambda) \\ S_\lambda &= \frac{l_2}{g \sin \theta} \partial_\lambda V(r, \theta, \lambda) \end{aligned} \quad (1.37)$$

where h_2 and l_2 are the second-order solid Earth tide displacement Love numbers.

It is worth noting that the values of the Love numbers recommended by IERS Conventions 2003 (McCarthy and Petit, 2004) include the anelastic contribution to the real part which leads to the displacement at the 1 mm level, but do not include the contribution to the imaginary part whose effects are about five times smaller. The maximum vertical displacement due to pole tide is approximately 25 mm, whereas the horizontal displacement can reach up to 7 mm.

In addition to the direct effect of the pole tide, the ocean pole tide generated by the centrifugal effect of polar motion on the oceans also loads the solid Earth. We call

this effect “ocean pole tide loading”. The model of ocean pole tide loading proposed by Desai (2002) recently has been adopted by the IERS conventions, which is available at [<2>](#). The ocean pole tide loading deformation is typically no larger than about 1.8 mm and 0.5 mm in the vertical and horizontal components, respectively, but it may occasionally be larger.

2.8 Summary

The basic theory and principles of tidal displacement modelling have been briefly discussed in this chapter along with some current modelling issues. Some important aspects of modelling tidal displacements are summarized as follows:

- 1) The theoretical and numerical framework for modelling site displacements due to solid Earth tides has been well established. The solid Earth tide models for site displacements recommended by IERS Conventions 2003 are generally considered to reach the desired accuracy of 1 mm.
- 2) OTL displacements are generally modelled via surface convolution of a global ocean tide model with appropriate Green’s function associated with the elasticity of the Earth. The accuracy of modelled OTL displacements mainly comes from the errors in ocean tide models.
- 3) Atmospheric tides excited mainly by solar heating also induce the Earth’s surface deformation. The deformation due to ATL can reach 1~2 mm in low latitudes in the vertical component, which are neglected in current geodetic analysis.

Chapter 3 GPS estimates of tidal displacements

As mentioned in Chapter 2, the tide-generating force not only causes the tidal response of the solid Earth periodically, but also produces ocean tides as well as atmospheric tides. Apart from the gravitational force, the atmospheric tides are mainly caused by solar irradiation. Both the oceanic and atmospheric tides also cause deformations of the solid Earth, which have the same periods as the solid Earth tides. The observed signal is indeed the sum of all these three parts. Strictly speaking, it is impossible to separate these different contributions to the total tidal signals. A general way to resolve this is to make an additional assumption that some of these contributions are well modelled or can be neglected at a reasonable accuracy level. The solid Earth tide is relatively well understood and has a relatively simple spatial structure which is identical to the tidal force. The atmospheric tide loading is so small that it is generally neglected at the present observation accuracy. OTL deformation, however, is more difficult to predict. The OTL effect has a more irregular spatial structure and depends strongly on the ocean tide in the region around the observing site.

The tidal displacements are investigated in this project by removing a priori modelled solid Earth tides from the observations. Here concentrate on the eight principal semi-diurnal (M_2 , S_2 , K_2 , and N_2) and diurnal (K_1 , O_1 , P_1 , and Q_1) tidal constituents, which account for approximately ~ 98 percent of the total tidal signal. The effects of the long-period constituents (the largest magnitude constituents are M_f ,

M_m and S_{sa}) are at least an order of magnitude smaller than those of the principal diurnal and semidiurnal constituents. The accuracy limitation of observations raises additional difficulties for the estimation of the long-period tidal displacements.

Methods for determining tidal displacements using GPS fall into two categories: the kinematic and static estimation techniques (e.g., King, 2006). The kinematic estimation technique generally involves two steps. First, subdaily GPS position time-series (usually 1-4 hour solutions) are estimated using conventional GPS positioning techniques. Second, the position time-series are analysed using a conventional least-squares tidal analysis method to derive the harmonic coefficients of tidal displacements (Khan and Tscherning, 2001; Vey et al., 2002; Yun et al., 2007; Vergnolle et al., 2008). This method can be implemented easily as it does not require changes to standard GPS processing software. However, an appropriate tropospheric zenith delay modelling method must be adopted in order to avoid absorption of tidal displacement effects into the tropospheric zenith delay estimates (Khan and Scherneck, 2003). Carrier-phase ambiguity parameters must also be fixed to their correct integer values to avoid aliasing effects of the displacement signals from the vertical component into the horizontal component (Vey et al., 2002; King et al., 2003).

The static estimation technique, on the other hand, treats the harmonic coefficients of tidal displacements as additional parameters in daily GPS data processing. The harmonic parameters and their full variance-covariance matrices extracted from

daily solutions are combined to obtain the estimates of tidal displacements (Schenewerk et al., 2001; Allinson et al., 2004; King et al., 2005; Thomas et al., 2007). It requires significant modifications to GPS processing software, as well as longer periods of observations in order to effectively de-correlate the tidal displacement parameters. Although this method is more complicated to implement, the static technique generally shows better performance than the kinematic technique (King, 2006).

The static estimation technique similar to that used in Allinson et al. (2004) and King et al. (2005) is employed in this study. The processing strategy how to derive tidal displacement estimates from GPS observations will be first described in detail. Some main technique issues related to this method are then investigated in order to show how dependant the method is on the quantity of data and processing strategy.

3.1 Precise point positioning using the GIPSY/OASIS II software

The GIPSY/OASIS II software (Version 4.04) developed at the Jet Propulsion Laboratory (JPL) was used in this study (Gregorius, 1996; Webb and Zumberge, 1997). GIPSY (GPS Inferred Positioning SYstem) and OASIS (Orbit Analysis and Simulation Software) are actually two separate packages although they use common modules. GIPSY has been designed for standard geodetic applications, whereas OASIS is a covariance analysis package for Earth orbiting and deep space missions. The software currently runs only under UNIX/Linux operating systems. It is

composed of a series of binary executable codes (both FORTRAN 77/90 and ANSI C) with C and Bourne shell scripts. The latter can be modified by the user if necessary, but not the former.

The major difference with respect to other precise GPS data analysis software is that double-differencing is not implemented in the GIPSY software, but instead un-differenced observations are processed and clock biases are estimated. GIPSY uses the Square Root Information Filter (SRIF) algorithm, a modified Kalman filter with high numerical stability, for parameter estimation (Lichten, 1990). This allows any parameter to vary in time according to a stochastic model. This is especially useful for clock biases, tropospheric delay and unmodelled spacecraft accelerations through the use of appropriate stochastic models. The site position can also be treated as stochastic parameters. GIPSY can estimate the site coordinates in all modes from static to fully kinematic.

The GIPSY/OASIS II software offers one special processing strategy which is called the Precise Point Positioning (PPP) technique (Zumberge et al., 1997). PPP has been demonstrated to be a powerful tool in geodetic and geodynamic applications. It makes use of precise GPS orbits, clocks and Earth orientation parameters as well as satellite eclipse information provide by global solution analysis centres, such as JPL and IGS. Then, observations from each site can be individually analysed by estimating receiver-specific parameters (position, clock, troposphere delay parameters and phase biases), while satellite-dependent parameters are held fixed at

their values in the global solution.

This technique results in a considerable reduction of computation time, since computational time increases linearly with the number of sites, not geometrically (exponentially) as in full network solution. Another advantage of the PPP method is that absolute site coordinates can be directly estimated in the global reference system, and errors at one site will not propagate into other sites. The accuracy of site coordinates derived from PPP solutions is comparable to that from global network solutions (Zumberge et al., 1997). The only major shortcoming is that PPP can not account for correlations between sites. Also, the covariance matrix of estimated parameters may not properly represent the accuracy of results so that the formal errors of estimated parameters will need scaling (may be a factor of two or so).

3.2 Estimation strategy

Neglecting three long-period terms, the locally referenced three-dimensional displacement Δc_k ($k = 1, 2$ and 3 denote the local east, north and vertical component, respectively) due to OTL can be modelled as a sum of displacements from the eight principal semidiurnal and diurnal constituents (McCarthy and Petit, 2004)

$$\Delta c_k = \sum_{j=1}^8 f_j A_{k,j} \cos(\omega_j t + \chi_j(t_0) + \mu_j - \Phi_{k,j}) \quad (1.38)$$

where all the notations are the same as in Eq. (1.32). Here, the reference time t_0 is

chosen to be J2000, and the phase lag is relative to Greenwich and lag positive. To permit linear parameter estimation, Eq. (1.38) needs to be linearised into sine and cosine terms

$$\Delta c_k = \sum_{j=1}^8 A_{ck,j} \cos(\omega_j t + \chi_j(t_0)) + A_{sk,j} \sin(\omega_j t + \chi_j(t_0)) \quad (1.39)$$

where

$$\begin{aligned} A_{ck,j} &= f_j A_{k,j} \cos(\Phi_{k,j} - \mu_j) \\ A_{sk,j} &= f_j A_{k,j} \sin(\Phi_{k,j} - \mu_j) \end{aligned} \quad (1.40)$$

The constituent-related parameters $A_{ck,j}$ and $A_{sk,j}$ in Eq. (1.39) can then be estimated along with other unknown parameters in GPS data analysis. In contrast to conventional GPS data analysis, an additional set of 48 tidal displacement parameters needs to be estimated for each site.

The practical data processing strategy is realised in two steps. Firstly, the harmonic coefficients of tidal displacements are estimated at the daily GPS data processing stage. The harmonic parameters and their full variance-covariance matrices extracted from daily solutions are then combined to obtain the final estimates of tidal displacements. The nodal corrections f_j and μ_j to each tidal constituent in Eq. (1.38) also needs to be taken into account in the second step.

3.2.1 Semi-diurnal/diurnal processing technique

The daily GPS observations were processed at each site using the PPP technique of

the GIPSY/OASIS II software. The merit of employing the PPP technique is that the absolute tidal displacements can be directly estimated. Additionally, this method greatly decreases the computational burden since massive GPS observation data are included in this project.

In contrast to a conventional PPP analysis, additional 48 tidal displacement parameters were simultaneously estimated together with other site-specific parameters (position, clock, troposphere delay parameters and phase biases). As mentioned above, the 48 parameters represent the harmonic motions (amplitudes of the sine and cosine components) for each of the eight principal semidiurnal and diurnal constituents in each of the local coordinate components. The a priori values of the tidal displacement parameters were set to 0.00 m. To avoid numerical instabilities in the daily PPP solutions, loose constraints of 0.02 m and 0.20 m were applied for the horizontal and vertical components, respectively. These constraints were chosen to be several times larger than the largest possible tidal displacement estimates in order to not over-constrain the estimates.

The non-fiducial precise orbits, clocks and Earth orientation parameters derived from the global GPS data analysis provided by JPL were held fixed. Using non-fiducial orbits benefits that they do not suffer from reference frame errors (Blewitt et al., 1992). Solid Earth tides and pole tides were corrected according to the IERS Conventions 2003 (McCarthy and Petit, 2004), but no a priori OTL model was applied. Both pseudorange and carrier-phase observations for each site were

decimated to five minute intervals and the pseudorange measurements were smoothed using the carrier phases. An elevation cutoff angle of 7° was used and no elevation-dependent weighting was assigned. The IGS relative receiver antenna phase centre variation models were applied. The priori zenith hydrostatic delays were calculated using the Saastamoinen model (Saastamoinen, 1972), and the Niell Mapping Function (Niell, 1996) was used. The tropospheric wet zenith delays and their gradients were estimated as random walk parameters with process noise values of $10.2 \text{ mm}/\sqrt{\text{h}}$ and $0.3 \text{ mm}/\sqrt{\text{h}}$, respectively. The receiver's clock was modelled as a white noise process updated at every epoch.

Carrier-phase ambiguities can also be fixed at this stage, and will be discussed in Section 3.3.2. Tidal displacement estimates and their variance-covariance matrices (VCM) were extracted from daily solutions for further processing.

3.2.2 Kalman filter combination

Daily tidal displacement estimates of each constituent vary greatly from day to day and have large formal errors. Moreover, it is more important to note that daily parameter estimates are highly correlated with each other due to the close banding of tidal frequencies. The tidal constituents cannot be separated with each other from a single daily solution. A method of stacking or combining daily tidal displacement estimates is then required before final estimates with sufficient accuracy can be obtained.

According to the Raleigh criterion, if two tidal constituents with frequencies f_1 and f_2 can be separated, the time span T of the observations need satisfy the following equation (Foreman, 1979)

$$|f_1 - f_2|T \geq R \quad (1.41)$$

where R is the Raleigh constant with default value 1. It is usually larger if the noise in the signal is colored. In this case, at least 182.6 days are required if daily tidal displacement estimates of S_2 and K_2 can be separable.

Daily tidal displacement estimates and their VCMs were combined using a standard Kalman filter method to produce the final estimates. It is equivalent to a sequential least-squares solution when the time variation of the estimated parameters is not considered. Process noises of each parameter can be conveniently added in the Kalman filter combination.

In the combination, daily estimates of unit variance were used to rescale each daily VCMs to ensure a final unit variance close to unity in two iterations. During the first iteration the daily VCMs were initially scaled by a factor of 30, and the unit variances were calculated and saved for the next processing step. The formal errors of daily coordinates derived from the conventional PPP solutions with the same data processing scheme are usually scaled by a factor close to 4 (King et al., 2006). The increase of the unit variance is caused by the addition of the tidal harmonic parameters. In the second iteration, the VCMs were rescaled by the respective unit

variances calculated from the first iteration to obtain the final estimates and their formal errors.

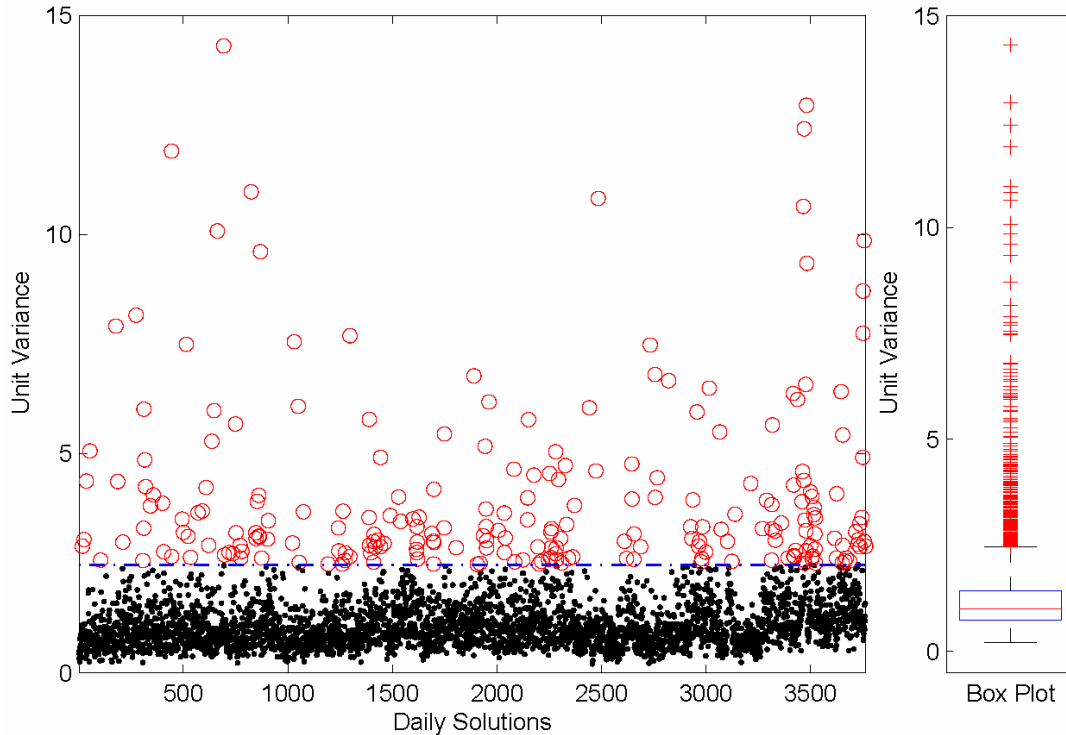


Figure 3.1 The daily unit variances at the ALGO site after the first iteration of the combined processing. The box plot on the right shows the statistical threshold for the outliers is 2.5 (also denoted by the dash-dotted lines on the left), which is far lower than the experimental value of 15. Only five daily solutions have the unit variances larger than 15 and are not shown here.

The unit variances were also used to identify outliers in daily solutions. A cutoff value of 15 (which is 450 times the original VCM due to the initial scale factor of 30) was chosen to remove the outliers in the processing. This value is relatively large to avoid excluding too many daily solutions (see Figure 3.1 for example). On average, only about 5% of daily solutions were removed in the final combined solution.

Various threshold values were also tested, and results shows that these values have negligible effect on the combined tidal displacement estimates.

3.2.3 Nodal corrections

For each of eight principal tidal constituents, the amplitude and phase estimates obtained actually include the effect of the nodal modulation (see Eqs. (1.39) and (1.40)). So the modal modulation correction is required so that only the contribution to the main constituent is found.

When one considers a main constituent j with satellites with indices jl , the relation between the estimated results for a main constituent and the actual cluster contribution is (Foreman, 1979)

$$f_j A_{k,j} \cos(\omega_j t + \chi_j(t_0) + \mu_j - \Phi_{k,j}) = A_{k,j} \left[\cos(\omega_j t + \chi_j(t_0) - \Phi_{k,j}) + \sum_l r_{jl} \cos(\omega_j t + \chi_j(t_0) - \Phi_{k,j} + \Delta_{jl}) \right] \quad (1.42)$$

where $\Delta_{jl} = V_{jl} - V_j + \alpha_{jl}$, the definition of α_{jl} is referred to Foreman (1979), and r_{jl} is the ratio of the tidal equilibrium amplitudes of the satellite l to the major contributor j . Expanding Eq. (1.42), the following explicit formulas can be derived for f and μ

$$f_j = \left[\left(1 + \sum_l r_{jl} \cos \Delta_{jl} \right)^2 + \left(\sum_l r_{jl} \sin \Delta_{jl} \right)^2 \right]^{1/2} \quad (1.43)$$

$$\mu_j = \arctan \left[\frac{\sum_l r_{jl} \sin \Delta_{jl}}{1 + \sum_l r_{jl} \cos \Delta_{jl}} \right]$$

The magnitudes of the nodal corrections for K_1 , K_2 , O_1 and Q_1 are large (up to 30% for K_2), whereas it can be neglected for the other four constituents (see Figure 3.2).

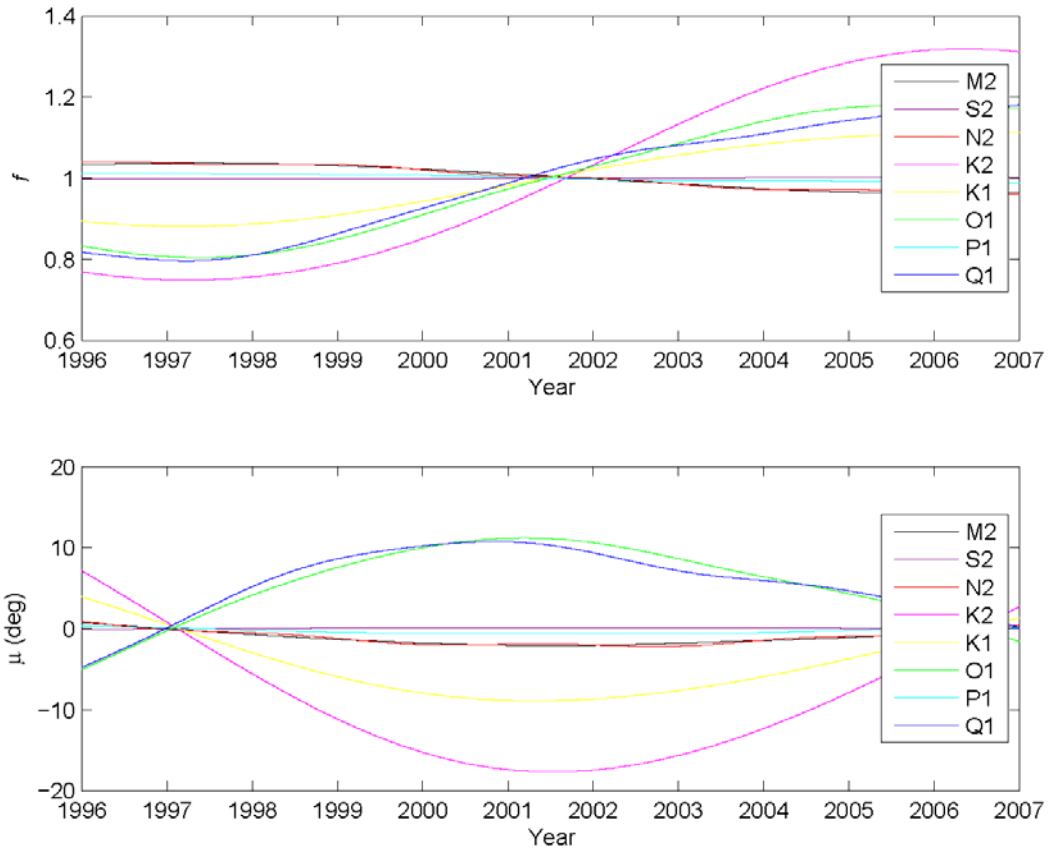


Figure 3.2 The time-dependent nodal correction parameters at the ALGO site during the period from 1996 to 2007.

Theoretically speaking, the nodal corrections should be applied to individual daily estimates of all constituents. In fact, it is improper to do so due to high correlations of daily estimates between these constituents. The parameters are only properly separated after they have been run through the Kalman filtering processing over a period of time. On one hand, if the corrections are applied too early during the filtering processing, the nodal corrections for each of the constituents would be

mixed. On the other hand, for the long-term data of up to ten years, it is also inappropriate that the mean modal corrections are applied to the final combined estimates since the nodal corrections will have undergone large temporal variations with a 18.6-year period (see Figure 3.2).

As a compromise, the nodal correction procedure described by Thomas et al. (2007) was adopted in this study. The daily tidal displacement solutions were combined into yearly batch solutions, to which the yearly average nodal corrections were applied. The yearly corrected solutions were then combined further to derive the final parameter estimates.

3.3 Technical issues related to GPS estimates of tidal displacements

In order to further understand the GPS estimates of tidal displacement using the GIPSY software, some technical issues are discussed in this section.

3.3.1 Constituent convergence

As discussed in Section 3.2.2, a long enough dataset is required to reliably determine the tidal displacement parameters of the eight main constituents. Therefore, it is interesting and necessary to know how long the dataset should be considered to obtain the reliable and accurate tidal displacements. By processing a ~1000-day span of GPS data, Allinson et al. (2004) has shown that a minimum of ~90 days of data is required to sufficiently resolve the principal semidiurnal and diurnal tidal

components at the 1 mm level (except for the K_1 and K_2 constituents). Results of King et al. (2005) and King (2006) have shown that estimates of tidal displacements of most constituents are generally well resolved with ~1,000 daily solutions. Additionally, King (2006) and Thomas et al. (2007) demonstrated that the K_2 constituent shows a time-variable behaviour, which has an impact on the other constituents (especially for S_2) through the covariance matrix.

Sites with more than 1,000 daily solutions after removing outliers were selected for this study. The results show that the estimates of the M_2 , N_2 , O_1 and Q_1 harmonics converge earlier than the S_2 , P_1 , K_2 and K_1 estimates (see Chapter 4 and Chapter 5 for details). The estimates of coastal sites for each constituent converge slower than those of inland sites. On the whole, that estimates of most of the constituents (except for K_1 and K_2) generally converge fairly well with more than the threshold of 1,000 daily solutions. However, the K_1 or K_2 constituent estimates does not stabilise at some sites. Tests reveal that some updates of the site equipments (antenna and receiver) appear to influence the convergence of K_1 , and the time-variable behaviour of K_2 is relevant to the GPS satellite geometry. Hence, the estimates of K_1 and K_2 should be regarded with caution.

3.3.2 Ambiguity resolution

Ambiguity parameters are highly correlated with the east component of coordinates, especially for sites at low latitude (Blewitt, 1989). Integer ambiguity fixing has been shown to significantly improve the east component of subdaily position estimates

(Larson et al. 2001; King et al. 2003). A limited number of previous studies have accounted for the impact of integer ambiguity fixing on the tidal displacements using the GIPSY software. Thomas et al. (2007, 2008) demonstrated that integer ambiguity fixing with the relatively low fixing success rates (about 30-50%) has a marginal improvement on the tidal displacement estimates. It is also worth noting that the network they used is very large and this is the main reason why ambiguity fixing rates were so low. It is still an open question whether integer ambiguity fixing is needed for tidal estimates.

Initially, integer ambiguities are left unresolved in daily PPP solutions since ambiguity resolution requires GPS observations at least two sites. After the daily PPP solutions for all the sites in a GPS site network are obtained, double-differencing GPS observations from sites observed simultaneously can be formed for ambiguity resolution in GIPSY (Blewitt, 1989). However, it brings back the problem of the computational burden into the data analysis because the processing time of the full network ambiguity resolution is generally scaled by $O(n^4)$. For this reason, interger ambiguity fixing was performed only in a regional network (see Chapter 4 for more details). Results have shown that the fixing of integer ambiguities results in marginal improvement on the tidal displacement estimates.

3.3.3 Source of biases

This study shows that the GPS technique can detect tidal displacements with millimetre precision, and sub-millimetre precision at some frequencies. However,

the GPS/model tidal displacement residuals exhibit a strong spatial coherence. Besides the modelled OTL displacement uncertainty, other sources of noises or model uncertainties at the tidal frequencies should also be considered. The GPS/model tidal displacement residuals cannot be distinguished from these systematic biases at this time. They generally involve the solid Earth tide model uncertainties Δc_{SE} , tidal geocentric motions Δc_{CM} , ATL Δc_{ATM} , and GPS-related errors ε_{GPS} . The GPS-observed tidal displacements Δc can be described as

$$\Delta c = \Delta c_{OTL} + (\Delta c_{SE} + \Delta c_{CM} + \Delta c_{ATM}) + \varepsilon_{GPS} \quad (1.44)$$

where Δc_{OTL} represents the actual tidal displacement values and Δc is the GPS estimates of tidal displacement.

In this study, the solid Earth tide models (Δc_{SE}) were corrected following the IERS Conventions 2003 implemented in GIPSY (McCarthy and Petit, 2004). The solid Earth models are developed on the basis of Mathews et al. (1997) and Dehant et al. (1999). The accuracy of solid Earth tide corrections in the IERS Conventions 2003 is usually considered to be about the 1% level, and the uncertainty of displacements due to solid Earth tides is at 1 mm level.

The uncertainty of solid Earth tide models is mainly dependent on the accuracy of the basic Earth models used (PREM) and on that of the modelling of anelasticity. The mantle anelasticity are included in the IERS Conventions 2003 using the mantle Q model developed by Widmer et al. (1991) with the assumption an ω^α frequency

dependence of Q with $\alpha = 0.15$ between a 200 s reference period and tidal periods. Unfortunately, there is still considerable uncertainty in the mantle anelasticity since the reference period and the value of α are not well constrained by observational data. The effects of the mantle's laterally heterogeneous structure on solid Earth tide deformations cannot be neglected either. The study of Metivier and Conrad (2008) shows that radial perturbations of surface displacements may reach no more than 0.3 mm, almost at the same precision level as obtained by GPS measurements in this study.

Subdaily tidal geocentric motions (Δc_{CM}) can reach several millimetres. Surface gravity measurements are insensitive to this motion, while space geodetic measurements, such as SLR and GPS, are fixed in space and are subject the geocentric motion. The centre-of-mass correction (CMC) was not applied at the JPL global analysis center before 05/11/2006. Pervious studies have shown that the frame origin of GPS appears to be insensitive to the mass center variations (Scherneck et al., 2000). In the regional analysis in Hong Kong (see Chapter 4 for details), the effect of CMC changes on the tidal displacements is tested, and results shows that the tidal displacement estimates appear insensitive to the center-of-mass variations. As only about one-year observations are available after 1400 GPS week in this study, one cannot infer that the influence of the center-of-mass variations on tidal displacement estimates can be simply ignored.

Diurnal and semidiurnal atmospheric tides (Δc_{ATM}) can cause periodic surface

deformation with maximum vertical magnitudes of around 2 mm and 3 mm peak-to-peak, respectively. Horizontal deformations are a factor of ten smaller in magnitude than the vertical deformations. Almost all geodetic GPS analyses do not model ATL effects at present. This study does not either find applying semidiurnal ATL corrections has any discernible effects on the S_2 tidal displacement estimates (see Section 5.3.4).

Unmodelled systematic errors related to the GPS technique themselves (ε_{GPS}) have significant influences on tidal displacement estimates of the K_1 and K_2 constituents (King et al., 2005; Thomas et al., 2007). The period of the GPS satellite orbits (one half a sidereal day) is almost equal to that of the K_2 constituent, and the satellite constellation repeat period (one sidereal day) is close to that of the K_1 constituent. Previous studies have suggested that GPS satellite orbit errors and multipath effects related to these two periods directly result in large uncertainties of K_1 and K_2 tidal displacement estimates (Schenewerk et al., 2001; King, 2006). Up to now, there is not yet an effective method of modelling multipath effects, and the accuracy of modelling GPS satellite orbits also needs to be further improved. In addition, higher-order ionospheric effects may likely bias the estimates of the solar-related K_1 , P_1 and S_2 constituents (Kedar et al., 2003), and errors in modelling of the tropospheric delay affect the S_2 estimates.

3.4 Summary

Three-dimensional tidal displacements at semi-diurnal and diurnal frequencies can

be directly estimated from continuous GPS observations via a modified PPP processing strategy. The two-step processing strategy not only minimises processing time and maximizes efficiency, but also preserves the long observational arcs that are required for the most accurate tidal displacement estimation. The parameterisation of the tidal displacement parameters makes ambiguity resolution unnecessary to determine unbiased horizontal displacement signals, although it would improve the overall accuracy of the solution. Several key technical issues concerning the data processing method and estimation technique have also been clarified in this chapter.

It has been disclosed that tidal displacements of most subdaily constituents (except for K_1 and K_2) can be resolved fairly well using more than 1,000 daily solutions. However, the K_1 or K_2 constituent estimates can not stabilise at some sites even if more than 3,000 daily solutions are used. This is mostly due to site-dependent multipath effects and GPS orbit errors. Chapter 4 will assess in detail the accuracy of tidal displacement estimates using a dense GPS network and the effect of ambiguity resolution is also tested.

Chapter 4 Estimates of tidal displacements using a dense GPS network in Hong Kong

The model accuracy for site displacements should be at least as good as geodetic observations in precise geodetic positioning, often thought of as being at the 1 mm level or better (Ray et al., 2007). There has been significant progress made in theoretical descriptions and numerical predictions for solid Earth tides in recent years (Wahr, 1981; Mathews et al., 1997; Dehant et al., 1999; Metivier and Conrad, 2008). The solid Earth tide models for site displacements recommended by the IERS Conventions 2003 are generally considered to reach the desired accuracy of 1 mm (McCarthy and Petit, 2004).

However, present OTL model predictions have not yet met the accuracy requirements for modelling the site displacements. Therefore, improvement of ocean tide modelling is still an important issue in high-precision geodetic OTL corrections. For a specific site, an alternative approach is to use the observations instead of the model predictions if the tidal displacements can be estimated with a better accuracy level by the means of geodetic techniques. The question arises as to whether the GPS-derived tidal displacements with sufficient accuracy can substitute for the modelled predictions, especially at coastal sites.

The formal errors of GPS-derived tidal displacements using the adopted strategy in Chapter 3 may be still over optimistic, since only time-independent noises are taken

into account in the combinations. In addition, the formal errors are almost equal for all the semidiurnal and diurnal tidal frequencies, but it is actually not the case. For example, the estimates of K_1 and K_2 do not generally converge well. Therefore, the formal errors for the two constituents should be scaled down. The estimates of the other two solar-related constituents, namely S_2 and P_1 , have notable seasonal fluctuations. The formal errors for these two constituents may be amplified accordingly. Therefore, the accuracy of GPS estimated tidal displacements should be assessed by comparison with model predictions or other independent measurements.

To explore the necessity and potential of the GPS tidal displacement estimates as substitutes for predictions using ocean tide models, the three-dimensional tidal displacements of 12 sites are determined using observations spanning three to seven years from a local dense continuous GPS network in the coastal areas of Hong Kong. This dense network distribution allows evaluation of the resolution and precision of tidal displacements estimated by GPS. The GPS-derived tidal displacements are compared with the predictions from seven recent global ocean tide models. Tidal gravity measurements in Hong Kong are also used to validate the GPS results and to identify technique-specific systematic errors. The impact of integer ambiguity fixing on tidal displacement solutions is also investigated.

The rest of this chapter begins with a description of GPS data sets in the study region and the data processing strategy. This is followed by comparison of the GPS-derived tidal displacements, the model predictions and gravity estimates.

Finally, discussion and conclusions are given.

4.1 Tidal characteristics in Hong Kong and GPS datasets

Hong Kong is located at a low-latitude coastal region on the northwest side of the South China Sea (SCS). The SCS is the biggest marginal sea in Southeast Asia. The basin occupies the central-east part of the SCS with the greatest depth exceeding 5000 m, whilst its shelf region occupies about 55% of the SCS. The tidal patterns are quite simple in the deep basin whilst the tidal regimes on the shelf are complex and tidal currents are strong (Fang et al., 1999). The dominant tidal constituents in the SCS are the principal diurnal constituents K_1 and O_1 , and the principal lunar semidiurnal constituent M_2 .

Moreover, due to the complex geometry of the coastline and the limited knowledge of the bathymetry, the shallow-water tides are amplified in this coastal area and the coastal tides become non-linear (Fang et al., 1999). Therefore, it is difficult to accurately model the ocean tides in this region. Figure 4.1 shows the maximum obtainable vertical OTL effects in Hong Kong, with a contour interval of 1 mm. The vertical displacement amplitudes caused by OTL effects reach around 27 mm to 38 mm. The effects of the prominent constituents K_1 , O_1 , and M_2 are about 7-10 mm, 7-9 mm and 6-8 mm, respectively.

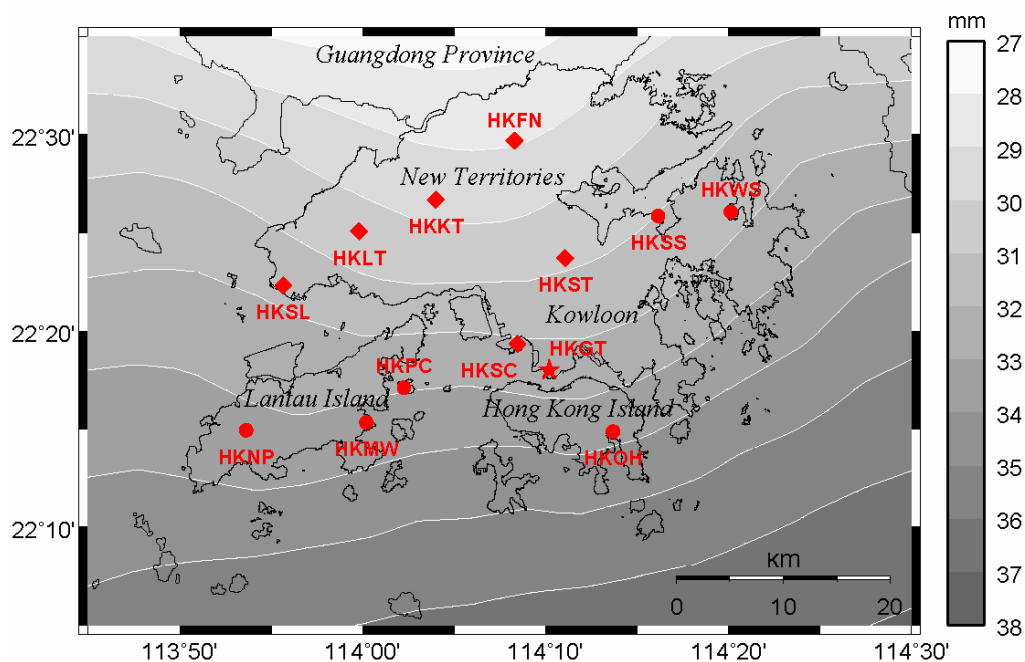


Figure 4.1 Location of 12 GPS sites and one gravity site in the coastal area of Hong Kong. Contours show the sum of the vertical OTL displacement amplitudes (mm) predicted using the NAO99b model of the eight major diurnal and semi-diurnal constituents (K_1 , O_1 , P_1 , Q_1 , M_2 , S_2 , K_2 , and N_2). GPS sites locations are shown for sites with about seven years of observations (marked as diamonds) and more than three years of observations (marked as round dots). The gravity site location is shown as a solid star.

A continuously operating GPS reference site network has been established by the Lands Department of Hong Kong Special Administrative Region (SAR) government since 2000. The network was implemented in two phases. In Phase I, six permanent GPS reference sites were constructed in the northwest and northern part of Hong Kong in 2000. In Phase II, another six sites in Lantau Island, Hong Kong Island and eastern part of the territory were established in early 2004 to extend the coverage of

the network. The network now consists of 12 continuously operating reference sites evenly distributed over Hong Kong, with a site spacing of about 10 km to 15 km. The location of the GPS sites is shown in Figure 4.1. GPS observations over the time span 01/01/2001 to 31/12/2007 were considered in this study. Six of the sites have seven years of observations while the other six sites have more than three years of observations for this study (see Appendix A.1).

4.2 Data processing

Daily GPS observations from each site were processed using the PPP model of the GIPSY/OASIS-II (Version 4.04) software on a site-by-site base. Ambiguity resolution was implemented after this, which will be discussed in Section 4.3. The daily estimates of tidal parameters along with their variance-covariance matrices were then stacked using the Kalman filter, and yearly nodal corrections were accounted for. Detailed processing procedure and parameter settings are listed in Chapter 3.

Parameters convergence plot of the HKFN site is presented in Figures 4.2-4.3 showing the amplitudes of residual vectors for each of eight constituents after the addition of each daily solution, relative to the final estimates. The HKFN site is selected as representative of the results of all sites, as can be seen from parameters convergence plots of all 12 sites in Appendix A.2. It can be seen from Figures 4.2-4.3 that the K_1 and K_2 constituents exhibit slower convergence than other constituents. The estimates of K_1 can not converge in the east and vertical

component during the whole observation period. The amplitudes of K_2 do not also stabilise on its final estimate in the vertical component. The amplitudes of four solar-related constituents, namely S_2 , K_2 , K_1 and P_1 , have notable seasonal fluctuations that are probably related to temperature variations. In addition, by comparing convergences of the ambiguity-free (Figure 4.2) and ambiguity-fixed (Figure 4.3) results, it is shown that ambiguity fixing slightly improves the convergence rate of parameter estimates.

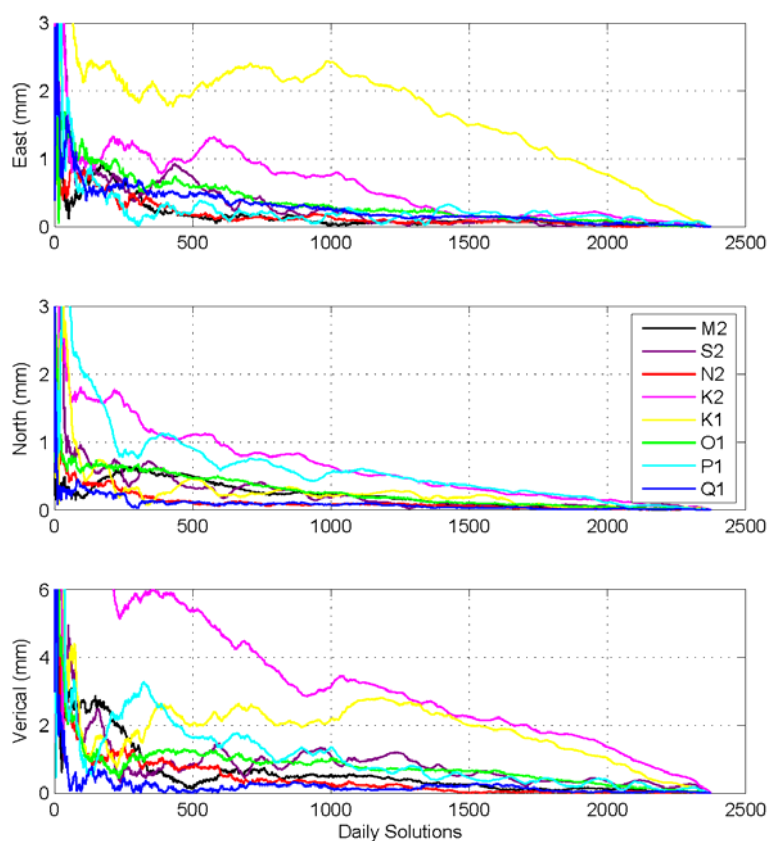


Figure 4.2 Parameter convergence of the HKFN site showing the amplitudes of residual vectors after the addition of each daily ambiguity-free solution, relative to the final ambiguity-fixed estimates for east (top), north (middle) and vertical (bottom).

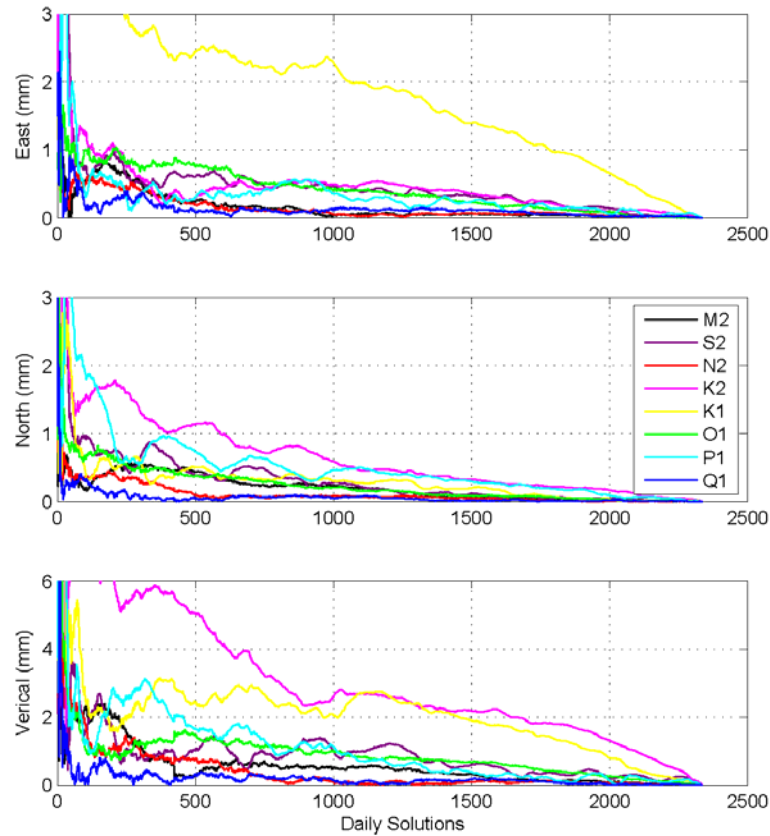


Figure 4.3 Parameter convergence of the HKFN site showing the amplitudes of residual vectors after the addition of each daily ambiguity-fixed solution, relative to the final ambiguity-fixed estimates for east (top), north (middle) and vertical (bottom).

King (2006) and Thomas et al. (2007) demonstrated that the time-variable behaviour in K_2 has an impact on the other constituents through the covariance matrix, which can be mitigated by addition of process noises to each K_2 parameter in the daily solution combination. To obtain insights into the performance of the additional process noises, different process noises were added (1, 15 and 25 mm^2 , respectively) to the K_2 parameters. The test results are different from previous studies (King 2006; Thomas et al. 2007). It is found that the addition of process noise indeed reduces the

agreement between the GPS and model estimates of K_2 and S_2 (see Figure 4.4) and significantly increases the correlations between the two constituents, with insignificant effects on other constituents. As the process noise increases, the agreement between the GPS and model estimates of K_2 and S_2 reduces gradually. Therefore, I did not add any process noises to the parameters in the combinations.

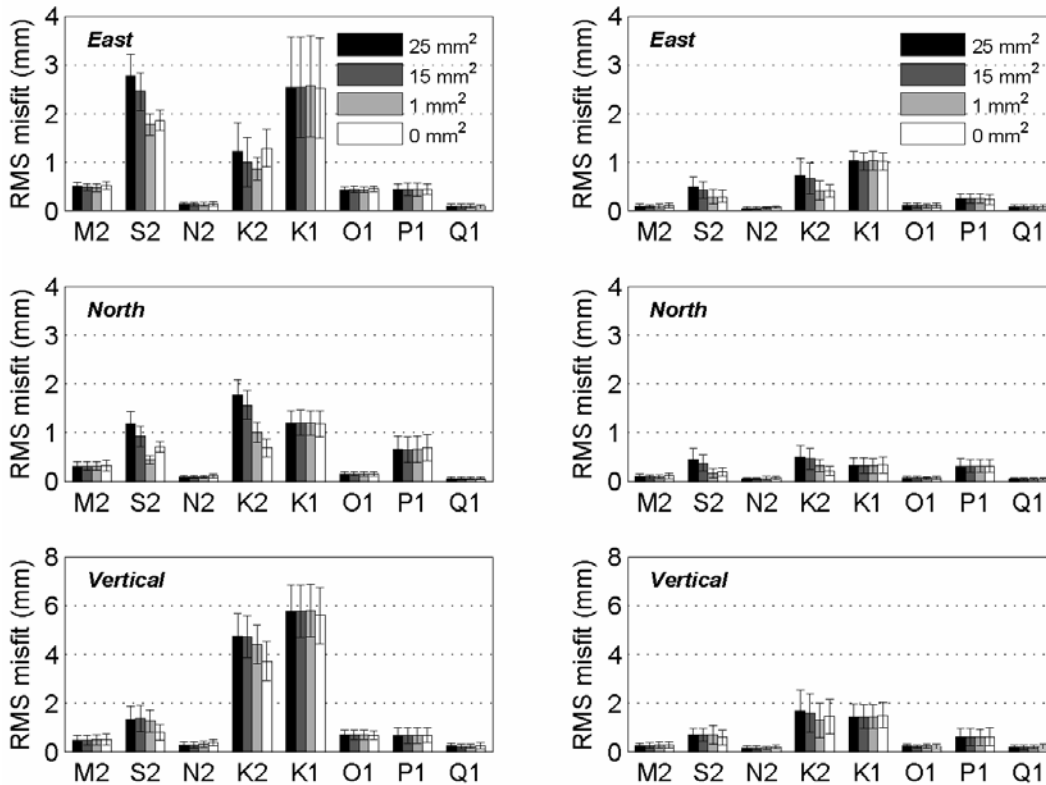


Figure 4.4 Effects of different process noises of K_2 on GPS tidal displacement estimates. The bars show misfits of the GPS tidal estimates to the NAO99b model values before (left) and after (right) removing the systematic biases. The misfit bars from left (black) to right (white) represent the addition of different process noises to K_2 (25, 15, 1 and 0 mm², in turn). One sigma formal error bars are also shown.

Another factor that needs to be considered is that JPL has started to include the

centre-of-mass correction (CMC) along with other model changes in the global GPS data analysis since 05/11/2006 (IGSMail-5438¹¹). Previous studies have shown that the frame origin of GPS appears to be insensitive to the mass centre variations (Scherneck et al. 2000). If there was orbit sensitivity to CMC, then this change may influence the tidal displacement estimates when the JPL non-fiducial orbit solutions spanning this date are used. The results using GPS observations from three different periods were compared (i.e., 01/01/2001 - 04/11/2006, 01/01/2001 - 31/12/2007 and 05/11/2006 - 31/12/2007, respectively). It is found that the tidal displacement estimates appear insusceptible to the centre-of-mass variations, at least at the measurement noises. Since it is expected that more observations achieve higher accuracy, the tidal displacement estimates combining all the daily solutions will be used in the following analysis.

4.3 Ambiguity resolution

In this study, all the sites in the local network processed using the PPP mode were brought together for integer ambiguity fixing. On average, ambiguities were successfully fixed on around 98% of the days. The mean success rate of daily integer ambiguity fixing is about 97% due to the short baselines (less than 100 km) in the network. Since the correlations of the tidal parameter estimates between sites are not obvious in the daily ambiguity-fixed solutions (i.e., correlation coefficients < 0.001),

¹¹ <http://igscb.jpl.nasa.gov/mail/igsmail/2006/msg00161.html>

the daily ambiguity-fixed tidal parameter estimates were combined in the Kalman filter on a site-by-site basis (Thomas et al., 2007), as described for the ambiguity-free solutions.

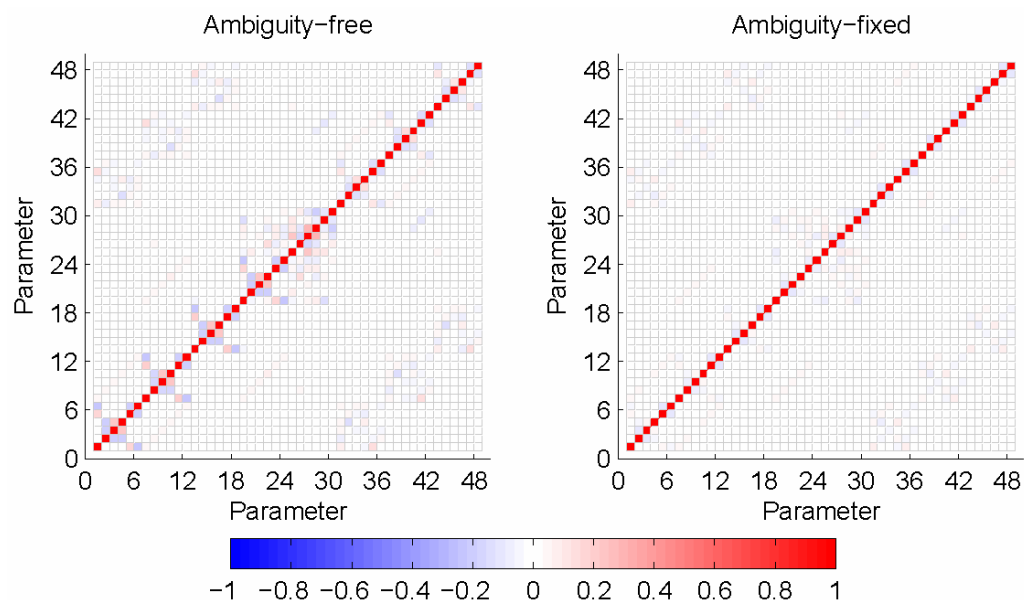


Figure 4.5 Parameter correlations of the tidal displacements from the ambiguity-free (left) and ambiguity-fixed (right) estimates at HKPC. Parameter numbers 1-6 are the M_2 east, north, vertical cosine coefficients, followed by their sine coefficients. The other constituent parameters (S_2 , N_2 , K_2 , K_1 , O_1 , P_1 and Q_1 in turn) are followed in the same way.

Integer ambiguity fixing slightly accelerates the parameter convergence, but significantly decreases the parameter correlations. The parameter correlation matrices derived from the final ambiguity-free and ambiguity-fixed solutions at HKPC are shown in Figure 4.5. HKPC with the least daily solutions (1109 ambiguity-free and ambiguity-fixed daily solutions after removal of outliers) is

selected for the comparison, since the differences between the ambiguity-free and ambiguity-fixed solutions decrease with the addition of daily solutions. Appendix A.3 also gives the results of all sites. It is seen from Figure 4.5 that ambiguity-fixing can effectively decorrelate the parameters. In addition, it is interesting that the correlations between M_2 and O_1 , S_2 and P_1 , N_2 and Q_1 , seem to be clearer after integer ambiguity fixing.

4.4 Results

The GPS tidal displacement estimates of both the ambiguity-free and ambiguity-fixed solutions in Hong Kong are listed in Appendix A.4. The distribution of differences between the ambiguity-free and ambiguity-fixed estimates for each constituent is illustrated in Figure 4.6. The K_1 and K_2 constituents have larger differences for all the three components compared to the other constituents. The K_2 vector difference at site HKWS abnormally reaches up to 2.2 mm in the east component. The exact reason for this outlier is unknown. For other sites, the K_2 vector differences are less than 1 mm in the east component.

The lunar-only constituents, M_2 , N_2 , O_1 and Q_1 , have relatively small differences of less than 0.2 mm, 0.1 mm and 0.4 mm for the east, north and vertical components, respectively. Overall, integer ambiguity fixing mainly influences the solar-related constituents, namely, S_2 , K_2 , K_1 and P_1 . Moreover, the differences between the ambiguity-free and ambiguity-fixed estimates in the east and vertical components are much larger than those in the north component for all the constituents. The

formal errors of the tidal displacement estimates in the east component are reduced by about 30% after integer ambiguity fixing, whereas the north and vertical components change insignificantly.

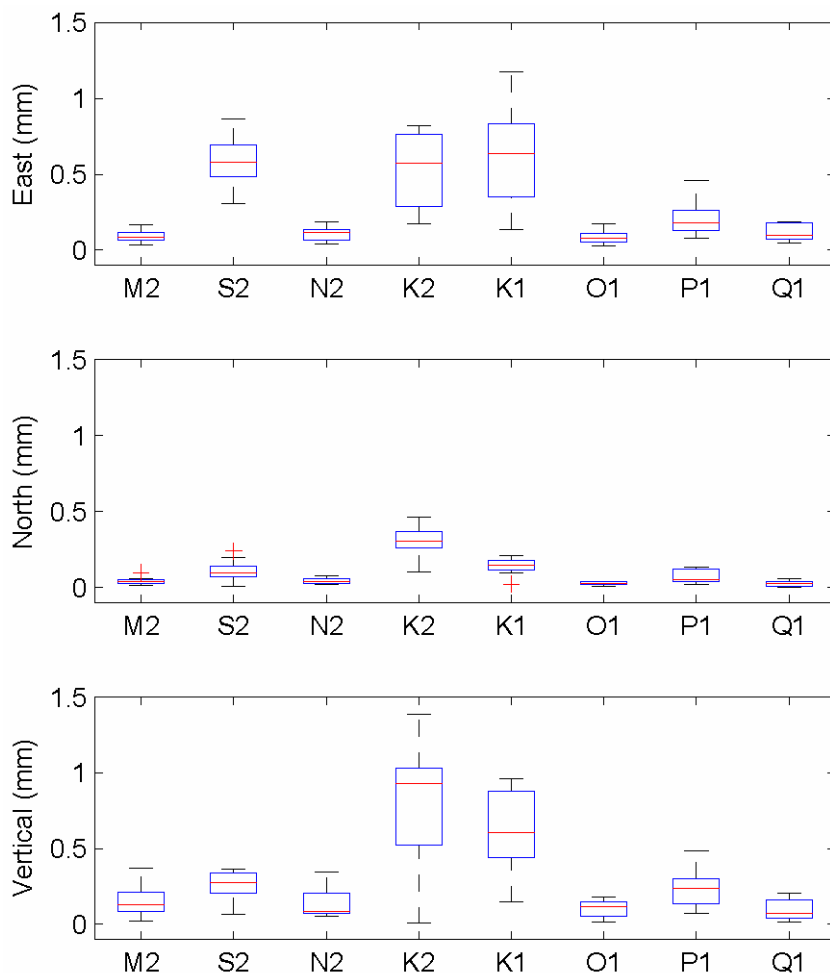


Figure 4.6 Box and whisker plot of the amplitudes of the vector differences between the ambiguity-free and ambiguity-fixed estimates for each constituent. The box describes the lower quartile, median and upper quartile values. The whiskers represent 1.5 times the interquartile range, and the plus signs represent outliers beyond the ends of the whiskers. The K_2 vector difference of HKWS is abnormally 2.2 mm in the east component and is not shown.

4.4.1 Comparison with modelled OTL displacements

To evaluate the accuracy of GPS-derived tidal displacement estimates, they have been compared with the model predictions. Amplitudes and phase lags of the modelled OTL displacements were computed for each of the 12 sites using the SPOTL software (Agnew, 1997) that convolves the input ocean tide model with the Green's function calculated from the Gutenberg-Bullen A Earth model (Farrell, 1972). Seven recent global ocean tide models were used to calculate the model values: AG06a (Andersen et al., 2006), CSR4.0 (Eanes and Shuler, 1999), EOT08a (Savcenko and Bosch, 2008), FES2004 (Lyard et al., 2006), TPXO7.1 (Egbert and Erofeeva, 2002), GOT4.7 (Ray, 1999) and NAO99b (Matsumoto et al., 2000). It is worth noting that two local ocean tide models of South China Sea (Fang et al., 1999) and East China Sea (Fang et al., 2004) were also tested. Only four principal constituents, namely, M_2 , S_2 , K_1 and O_1 , are included in these two models. It was found that the results improve insignificantly when including these two local tide models. So the results of these two local models are excluded from the following analysis.

The agreement between the GPS and model estimates were assessed by comparing their RMS misfits (Thomas et al., 2007; Melachroinos et al., 2008). For each of the eight tidal constituents j in each coordinate component k , the GPS/model RMS misfits for the $n = 1, \dots, N$ sites are defined as

$$\text{GPS/model RMS misfit}_{j,k} = \left(\frac{1}{N} \sum_{n=1}^N |Z_{j,k,n}|^2 \right)^{1/2}$$

with

$$Z_{j,k,n} = [A_{\text{GPS}} (\cos \Phi_{\text{GPS}} + i \sin \Phi_{\text{GPS}})_{j,k,n} - A_{\text{model}} (\cos \Phi_{\text{model}} + i \sin \Phi_{\text{model}})_{j,k,n}] \quad (4.1)$$

where A is the amplitude and Φ is the Greenwich phase lag.

The RMS misfits between GPS ambiguity-fixed estimates and the predictions from seven ocean tide models along with the one-sigma error bars are shown in Figure 4.7. The AG06a model exhibits the worst agreement with the GPS estimates, especially for M_2 , whose misfit can reach up to 4.5 mm in the vertical component. The CSR4.0 model shows the second worst agreement, mainly for the M_2 constituent in all the three components and the N_2 constituent in the north component. The models with better agreements are EOT08a, FES2004, TPXO7.1, GOT4.7 and NAO99b, and differences between them become insignificant. The NAO99b model is then taken as a reference model and the misfits of ambiguity-fixed and ambiguity-free estimates to the model predictions are compared as shown in Figure 4.8. Integer ambiguity fixing only has a slight influence on the GPS/model misfit, except for the K_2 constituent. The GPS/model misfits of the K_2 constituent in the horizontal components are significantly improved after ambiguity fixing.

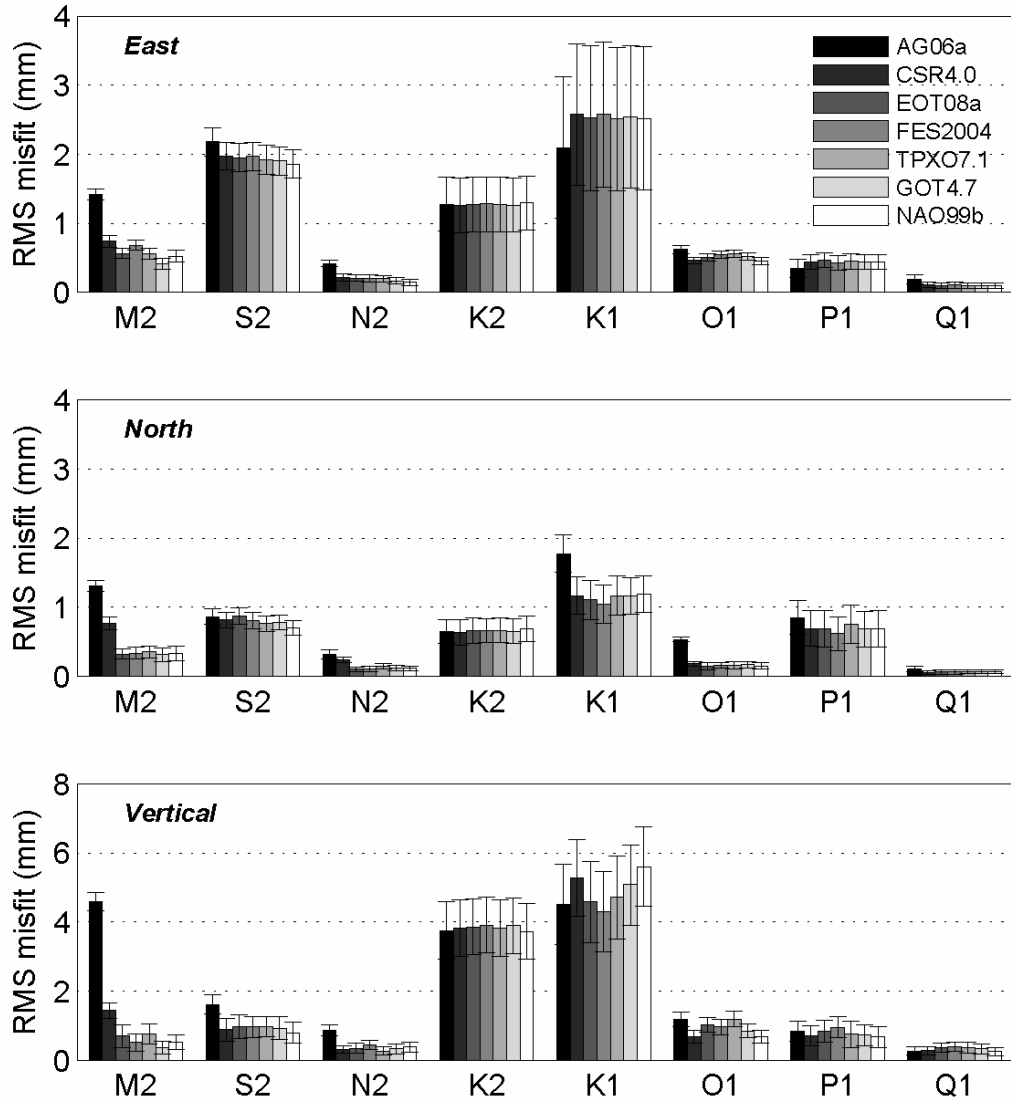


Figure 4.7 Misfits of the GPS ambiguity-fixed tidal displacement estimates to the model predictions. The misfit bars from left (black) to right (white) represent AG06a, CSR4.0, EOT08a, FES2004, TPXO7.1, GOT4.7 and NAO99b, respectively. One sigma formal error bars are also shown on top of the misfit bars.

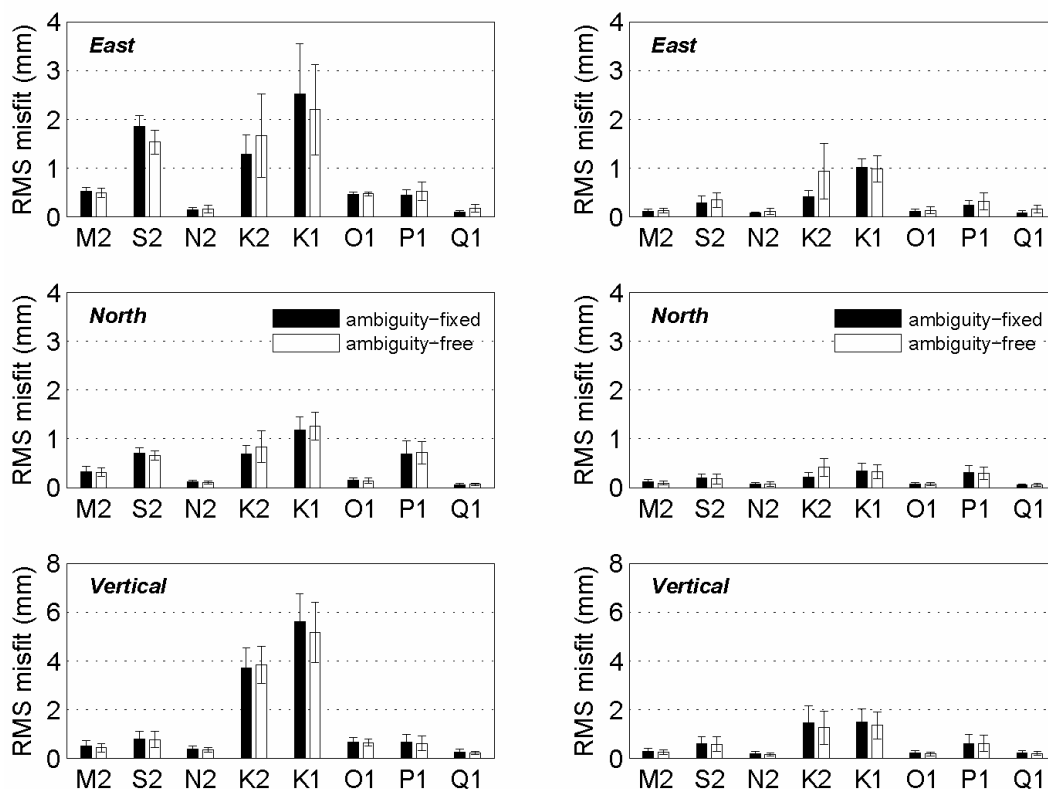


Figure 4.8 Misfits of the GPS-derived tidal displacement estimates to the NAO99b model estimates before (left panel) and after (right panel) removing the mean systematic biases. The misfit bars are (1) GPS (ambiguity-fixed)/model (black), (2) GPS (ambiguity-free)/model (white). One sigma formal error bars are also shown.

It can be seen from Figure 4.7 and the left panel of Figure 4.8 that the K_1 constituent shows the worst GPS/model agreement for all the three components, which is different from the results of Thomas et al. (2007). Their results show that the worst is K_2 . It is considered that the discrepancy is caused by addition of 15 mm^2 process noise to the K_2 parameters in their filtering combination. As discussed in Section 4.2, I believe that the addition of process noise to the K_2 parameters indeed increases the GPS/model misfits of K_2 . The K_2 constituent in my results is the second worse

agreement with the model. The GPS/model misfits are also relatively larger for S_2 in the horizontal components and P_1 in the north component. The misfits for the lunar constituents, M_2 , N_2 , O_1 and Q_1 , are quite small at the sub-millimetre level.

The residuals between the GPS-derived and modelled values exhibit a strong spatial coherence for all the constituents in our study region. In this study, the systematic biases are considered to be constant due to the small region (about 40 km×50 km) and thus define the following equation as the observed RMS misfits:

$$\text{Observed RMS misfit}_{j,k} = \left(\frac{1}{N} \sum_{n=1}^N |Z_{j,k,n} - \text{mean}(Z_{j,k,n})|^2 \right)^{1/2} \quad (4.2)$$

where $\text{mean}(Z_{j,k,n})$ is the mean value of residual vectors of 12 sites between the GPS-derived and modelled tidal displacement estimates.

The observed RMS misfits are almost the same for the seven models mentioned earlier. Therefore, only the NAO99b model is taken as an example in the analysis below. Here, the misfits can be regarded as being caused by site-dependent errors and observation noises. Sources of the systematic bias generally involve the solid Earth tide model uncertainties, atmospheric tide loading, tidal geocentric motions, GPS orbit errors and higher-order ionosphere effects (King et al., 2005). The GPS/model tidal displacement residuals cannot be distinguished from these systematic biases at this time.

The observed RMS misfits based on the NAO99b model are also shown in Figure

4.8. Comparison of the left and right panels in Figure 4.8 shows that removal of the systematic biases can greatly reduce the GPS/model misfits for all the eight tidal constituents. When the systematic biases have been removed, the misfits of the ambiguity-fixed estimates are slightly less than the ambiguity-free estimates for all the constituents in the east component except for K_1 . The observed misfits of both the ambiguity-fixed and ambiguity-free estimates are quite small for the M_2 , N_2 , O_1 and Q_1 constituents, i.e., less than 0.3 mm (east), 0.2 mm (north) and 0.5 mm (height). The next smallest observed misfits are S_2 and P_1 . Both of their misfits are within 0.5 mm and 1.0 mm, for the horizontal and vertical components, respectively. The constituents with the worst misfits are K_1 and K_2 . Their observed misfits can reach up to 2.5 mm for the vertical component. This is likely due to site-dependent error sources such as multipath effects at the K_1 and K_2 frequencies (King et al., 2005).

To assess the differences in scatter between the GPS and model estimates, a weighted chi-square statistic for the GPS tidal displacement estimates was calculated using all the seven models (Thomas et al., 2007; Melachroinos et al., 2008). The chi-square statistic per degree-of-freedom is defined by

$$\chi_{\text{dof}}^2 = \frac{1}{N} \sum_{j=1}^{8(6)} \sum_{k=1}^{3(1)} \sum_{n=1}^N \left(\frac{|Z_{j,k,n}|}{\sigma_{\text{GPS}(j,k,n)}} \right)^2 \quad (4.3)$$

Table 4.1 gives the values of χ_{dof}^2 of the ambiguity-fixed and ambiguity-free estimates for all the 3D, east, north and vertical components. The values of χ_{dof}^2

with bias removal based on the NAO99b model are also calculated for comparison. Since the large systematic biases (likely GPS-related) are present in the K_1 and K_2 constituents, the chi-square statistics for the six constituents (excluding K_1 and K_2) are also given in Table 4.1.

It is seen from Table 4.1 that the values of χ_{dof}^2 of the ambiguity-fixed estimates are larger than those of the ambiguity-free estimates for the east component. This is due to the smaller formal errors of the east ambiguity-fixed estimates. With the exception of K_1 and K_2 , the NAO99b and GOT4.7 models show better agreement with the GPS estimates of tidal displacements than the TPXO7.1, FES2004, EOT08a and CSR 4.0 models. The AG06a model shows the poorest fit to the GPS estimates.

Table 4.1 Chi-square per degree-of-freedom for the GPS and gravity estimates to the model predictions

Model	All the eight constituents									Excluding the K ₁ and K ₂ constituents								
	3D		E		N		U		gravity	3D		E		N		gravity		
	fixed	free	fixed	free	fixed	free	fixed	free		fixed	free	fixed	free	fixed	free			
AG06a	28.56	25.81	12.41	5.79	10.96	13.85	5.19	6.17	6423	16.20	12.91	8.07	3.55	5.81	6.46	2.32	2.90	5601
CSR4.0	20.54	16.36	11.17	4.89	5.48	7.05	3.88	4.42	1238	8.58	5.79	5.22	2.07	3.01	3.32	0.34	0.40	824
EOT08a	18.56	14.48	10.70	4.73	4.57	6.00	3.29	3.75	1368	7.50	4.85	4.92	1.97	2.28	2.54	0.29	0.34	980
FES2004	18.33	13.85	11.16	4.92	4.06	5.37	3.11	3.56	1389	7.43	4.57	5.19	2.09	1.96	2.15	0.28	0.33	908
TPXO7.1	18.62	14.77	10.55	4.64	4.70	6.24	3.37	3.89	1233	7.34	4.77	4.82	1.88	2.22	2.51	0.31	0.38	917
GOT4.7	18.49	14.70	10.35	4.53	4.54	6.07	3.60	4.10	977	6.77	4.27	4.52	1.75	2.04	2.30	0.20	0.22	656
NAO99b	18.63	14.93	10.20	4.45	4.51	6.02	3.91	4.46	960	6.43	4.01	4.39	1.70	1.88	2.13	0.16	0.18	588
NAO99b ^a	2.20	2.22	1.25	1.00	0.50	0.75	0.45	0.47	-	0.49	0.49	0.16	0.13	0.25	0.27	0.08	0.09	-

^a Chi-square per degree-of-freedom for the GPS tidal estimates to the NAO99b model estimates after removal of the systematic biases.

4.4.2 Comparison with gravity results

In order to further validate the reliability and accuracy of the GPS tidal displacement estimates, the results were compared with independent tidal gravity observations. Sun et al. (2006) used 483 days of gravity observations made by a La-Coste-Romberg (LCR)-ET20 gravimeter in Hong Kong to derive precise tidal gravity estimates. The location of the gravity site is shown in Figure 4.1, and the site coordinates are attached in Appendix A.1. Air pressure effects on the gravity observations were removed during the gravity processing by using the air pressure admittance, which was obtained by a linear regression between gravity observations and local air pressure data.

The theoretical solid Earth tides were corrected using the DDW99 non-hydrostatic inelastic Earth model (Dehant et al., 1999) and the Hartmann-Wenzel tidal potential (Hartmann and Wenzel, 1995). Detailed data processing is described in Sun et al. (2006). The observed gravity tidal loading and the corresponding formal errors are listed in Appendix A.4, while observed and model estimates in terms of a phasor diagram are shown in Figure 4.9. The formal errors of the observed estimates are quite small, only about $0.01\sim 0.02 \times 10^{-8} \text{ m/s}^2$. The χ_{dof}^2 statistics are also listed in Table 4.1.

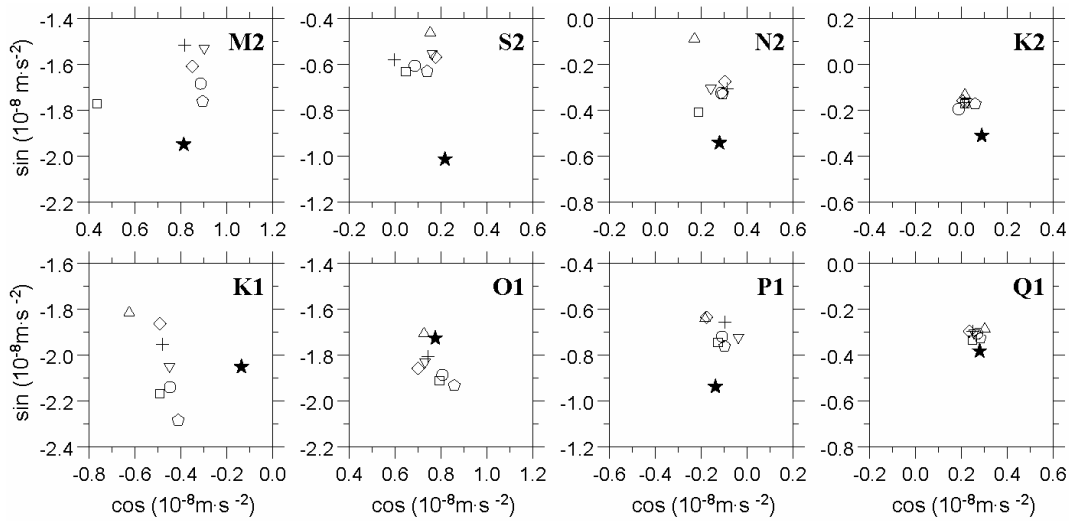


Figure 4.9 Phasor diagrams of tidal gravity estimates in Hong Kong. The gravity estimates are represented by solid stars, and their formal errors are too small to be shown. Seven model values (AG06a, triangles; CSR4.0, squares; EOT08a, crosses; FES2004, diamonds; TPXO7.1, inverted triangles; GOT4.7, circles; NAO99b, pentagons) are also illustrated. The M_2 vector difference between the observed and AG06 estimates is too large so that the M_2 value of AG06 can not be shown.

It can be seen from Figure 4.9 and Table 4.1 that the AG06 estimates have the worst agreement with the gravity observations among the seven models, which is consistent with the GPS results. It is noticed that the CSR4.0 model offers the second worst agreement with the GPS estimates, mainly for the M_2 constituents. However, gravity observations show that CSR4.0 is the best model, except for GOT4.7 and NAO99b. Closer inspection of Figure 4.9 shows that there is a significant systematic bias between the CSR4.0 value and the other model estimates of M_2 . It indicates that the CSR4.0 model is unreliable for OTL correction in this region and the GPS results may be more suitable for validating ocean tide models

than the gravity observations. In addition, the CSR4.0 estimate of N_2 in the north component exhibits the worse agreement with the GPS estimate, whereas the gravity measurement shows that CSR4.0 exhibits the best performance for N_2 .

Both the GPS and gravity results of S_2 have significant biases with the model estimates. The GPS/model misfits can reach up to 1.8 mm in the east component and the misfits of gravity/model estimates reach $0.4 \times 10^{-8} \text{ m/s}^2$. The gravity results also suggest that the poor accuracy of the GPS-derived tidal displacements for the K_1 and K_2 constituents is mainly due to the GPS-related error sources, such as satellite orbit error and multipath effects. When the K_1 and K_2 constituents are excluded, the χ_{dof}^2 statistics (Table 4.1) show that both GPS and gravity techniques can be used to validate ocean tide models in Hong Kong and they yield highly consistent results. Moreover, the CSR4.0 model can be effectively excluded by using the GPS estimates. Both the GPS and gravity estimates suggest that GOT4.7 and NAO99b are the most suitable ocean tide models in this region.

4.5 Summary

Three to seven years of GPS observations from the dense continuous GPS network in Hong Kong have been analysed to accurately measure the subdaily 3D tidal displacements. By comparing with the predictions from seven recent global ocean tide models and the results of gravity observations, we found that the GOT4.7 and NAO99b models are most suitable for OTL corrections in Hong Kong at present. The GPS estimates for the constituents M_2 , N_2 , O_1 , P_1 and Q_1 are consistent with the

NAO99b model predictions at the sub-millimetre level for all the three components. However, the S_2 , K_1 and K_2 constituents show larger discrepancies between the GPS and model estimates. Integer ambiguity fixing improves the agreement between the east tidal displacement estimates and the model predictions, especially for the K_2 constituents. The north component of K_2 has also been improved significantly after ambiguity fixing.

The residuals between the GPS and model values exhibit strong regional coherence. After the systematic biases between the GPS and model values are removed, the observed misfits between sites for the six major subdaily constituents (except for K_1 and K_2) are all less than 0.5 and 1.0 mm for the horizontal and vertical components, respectively. For the K_1 and K_2 constituents, the observed misfits are large (less than 2.5 mm for all the three components).

The GPS results have shown the large systematic horizontal biases relative to the model values at the S_2 frequency. The gravity results also systematically deviate from the model estimates. Though sources of the biases cannot be identified at this moment, the GPS and gravity observations indicate the presence of some common errors sources, such as OTL modelling errors, residual solid Earth tides and atmospheric tide loading. By comparing the bias with the S_2 atmospheric tide loading calculated by T. M. van Dam¹², it is found that the horizontal atmospheric

¹² <http://www.ecgs.lu/atm/>

tide loading displacements are too small (0.1 mm) to explain the large biases of around 1.8 mm (east) and 0.7 mm (north). Other possible GPS-related causes for the S_2 signals include residual tropospheric delay errors, higher order ionospheric effects, GPS orbits and clock errors.

As shown in previous studies by Schenewerk et al. (2001), King et al. (2005) and Thomas et al. (2007), discrepancies between the GPS and model estimates for K_1 and K_2 are relatively large. Our results have shown that the residual displacements still exhibit some spatial coherence. This is possibly due to the GPS orbit errors. The site-dependent errors, such as multipath effects are at the same magnitude level. Local environment changes, such as the addition of an antenna domes, appear to have significant influence on the K_1 estimates. Adding process noise to K_2 made our S_2 tidal displacement estimates further from the model values.

Penna et al. (2008b) have demonstrated that present OTL modelling cannot meet the accuracy requirements for precise geodetic positioning at one millimetre level mostly due to ocean tide model uncertainties in some coastal areas. Our results have shown that the GPS tidal estimates of principal diurnal and semidiurnal constituents (excluding K_1 and K_2) with the sub-millimetre accuracy can provide an alternative to the model predictions at the Hong Kong sites. The K_1 and K_2 estimates should be used with caution due to their relatively large misfits between the GPS and model estimates. This study is also limited to a small region. To obtain a deeper insight into the systematic biases between the GPS and model values, globally distributed sites

(the IGS05 reference sites) will be further investigated in Chapter 5.

Chapter 5 Tidal displacements derived from a global GPS network

The global GPS network, currently composed of thousands of continuous GPS sites worldwide, offers the possibility of studying tidal displacements with the great spatial density. Most of previous studies about GPS tidal measurements, conducted with the main purpose of testing ocean tide models, focused on a few coastal areas where ocean tide modelling is generally considered to be deficient (e.g., Khan and Tscherning, 2001; King et al., 2005; Yun et al., 2007; Vergnolle et al., 2008). The observed and modelled differences are considered mainly due to the errors in ocean tide models and the poor accuracy of GPS measurements.

Schenewerk et al. (2001) first determined the vertical tidal displacements at eight major semidiurnal and diurnal constituents for 353 sites using three years of GPS observations at the global scale. They found that there exist large-scale systematic differences between the observed signal and models. Unfortunately, the horizontal components have been neglected and the accuracy of the tidal displacement estimates is too low to be used for testing the latest ocean tide models (Petrov and Ma, 2003; King et al., 2005). Based on analysis of 25 co-located GPS and VLBI sites, Thomas et al. (2007) demonstrated that there is no apparent spatial pattern in amplitude or phase of the GPS/model misfits in either latitude or longitude.

The regional analysis in Chapter 4 has shown that the misfits between sites for the

six major constituents (except for K_1 and K_2) are all less than 0.5 mm and 1.0 mm for the horizontal and vertical components, respectively, after the systematic biases between the GPS and model values are removed. To better understand the spatial distribution of the systematic biases, three-dimensional tidal displacements of eight major semidiurnal and diurnal frequencies at 125 globally distributed GPS sites are estimated. The results are evaluated and compared with the VLBI estimates and model values. The effects of possible error sources are also discussed in detail.

5.1 Dataset and data processing

GPS observations at 132 IGS05 reference sites were collected over the period from 01/01/1996 to 04/11/2006 in this study. GPS observations after 04/11/2006 were excluded because the centre-of-mass corrections (CMC) have been introduced along with other model changes in the global GPS analysis since that day. The regional test results in Chapter 4 have shown that the tidal displacement estimates appear to be insensitive to the centre-of-mass motions. Therefore, I did not attempt to further test the effects of the CMC, but discarded GPS observations after 04/11/2006 to avoid confusion in explaining the results. Sites with more than 1,000 daily solutions after removing outliers were further selected in this study. Seven sites (CONZ, ISPA, LHAZ, MDVJ, NOVJ, OHI3 and REUN), which did not satisfy this criterion, were excluded from the following analysis. There are 67 of total 125 sites with more than 3,000 daily solutions, and only 20 sites with 1,000-2,000 daily solutions (see Figure 5.1).

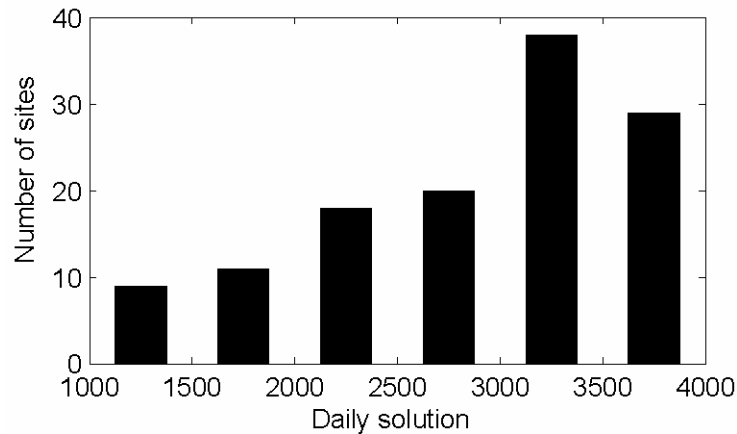


Figure 5.1 Histogram of daily solutions for global GPS sites

GPS observations from each site were processed using the PPP strategy in GIPSY/OASIS-II (Version 4.04) software on a daily basis. Ambiguity resolution was not implemented due to large processing time at this stage. From the regional results in Chapter 4, I believe that ambiguity resolution just provides marginal improvement in the accuracy of the tidal displacement estimates at present. Even now, the effects of ambiguity resolution on the tidal displacement estimates still need to be further investigated at a global scale. It is expected that some of the rapid ambiguity resolution algorithms, such as Ambizap (Blewitt, 2008), can be applied to global network solutions. After this, the daily estimates of tidal parameters along with their variance-covariance matrices were combined using a Kalman filter. Yearly nodal corrections were applied during the combinations. Details on the processing procedure and parameter settings have been described in Chapter 3.

To obtain further insights into the global performance of the additional process noises, different process noises (i.e. 1, 15 and 25 mm²) to the K_2 parameters were

added using the same method as in the regional analysis (see Section 4.2). Test results are shown in Figure 5.2. The addition of process noises reduces the agreement between the GPS and model estimates of K_2 . As the process noise increases, the agreement between the GPS and model estimates of K_2 reduces gradually. In addition, the addition of process noises has a slight influence on the GPS/model misfits of S_2 and no effects on the other constituents at all. Therefore, I did not add any process noises to the parameters in the combination process.

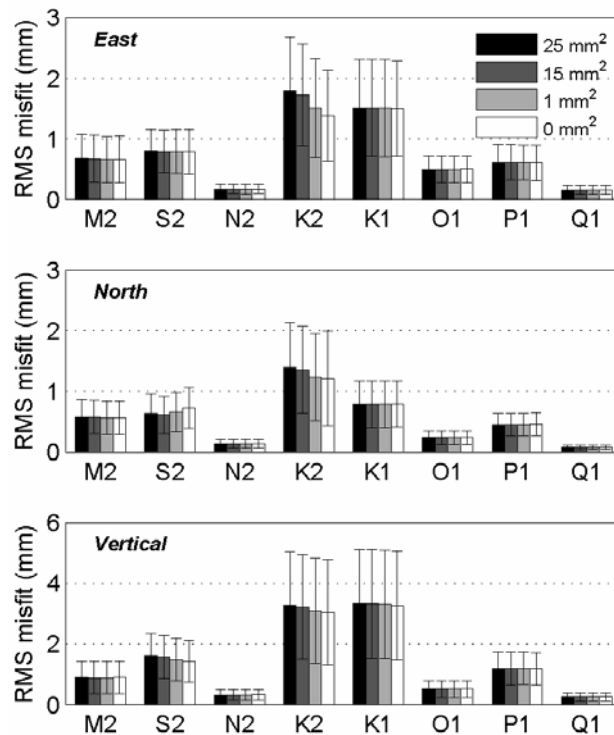


Figure 5.2 Effects of adding different process noises to K_2 on GPS tidal displacement estimates. The bars show misfits of the GPS tidal estimates to the FES2004 model predictions. The misfit bars from left (black) to right (white) represent the addition of different process noises to K_2 (25, 15, 1 and 0 mm², in turn). One sigma formal error bars are also shown.

The time-variation of the tidal parameter estimates may be examined from the constituent convergence plot of each site. Figure 5.3 shows, as an example, the amplitudes of residual vectors for each of the eight constituents after the addition of each daily solution, relative to the final estimates, at the inland site ALGO and the coastal site MAC1. Convergence plots of all the 125 sites can be found in Appendix B.1. The results show that the estimates of the M_2 , N_2 , O_1 and Q_1 constituents converge much faster than those of S_2 , P_1 , K_2 and K_1 . Also convergences of the estimates at coastal sites are slower than those at inland sites since the coastal sites have larger tidal signals. The notable seasonal fluctuations of the two solar-related constituents, S_2 and P_1 , can be seen from the convergence plots of each site.

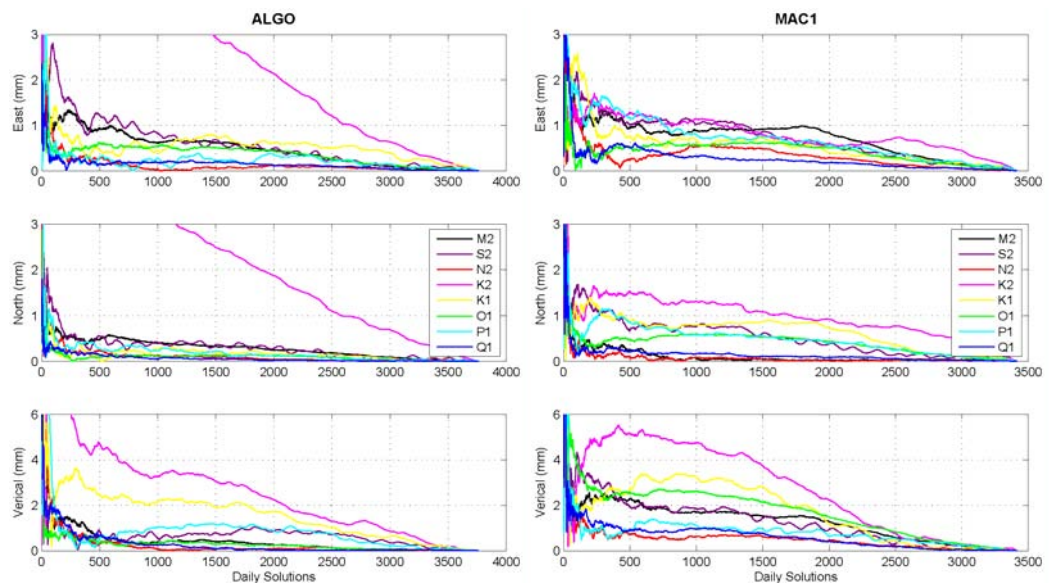


Figure 5.3 Convergence plots of the inland site ALGO (left) and the coastal site MAC1(right), showing the amplitudes of residual vectors after the addition of each daily solution, relative to the final tidal estimates, for the east (top), north (middle) and vertical (bottom) components.

On the whole, the tidal estimates using more than 1,000 daily solutions can converge well for most of the constituents except for K_1 and K_2 . The K_1 or K_2 estimates can not stabilise at some sites (e.g., the K_2 constituent at the ALGO site in Figure 5.3 and at Figure 5.4). Convergence plots also reveal that updates of the site equipment (e.g., antenna and receiver) appear to influence the convergence of K_1 . For example, the antenna and receiver changes on 08/06/2000 seem to seriously affect the convergence of the K_1 constituent at the WUHN site (see the convergence plot of the WUHN site in Figure 5.4). The time-variable behaviour of K_2 relative to the GPS satellite geometry is considered to contribute to its slow convergence. So the tidal parameter estimates of K_1 and K_2 need to be treated with caution.

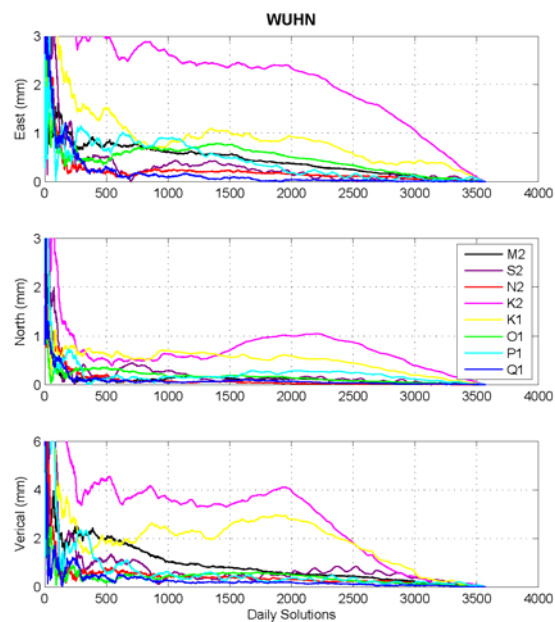


Figure 5.4 Convergence plots of the WUHN site, showing the amplitudes of residual vectors after the addition of each daily solution, relative to the final tidal estimates, for the east (top), north (middle) and vertical (bottom) components.

The parameter correlations of tidal displacement estimates exhibit a latitude-dependent pattern. The parameter correlation matrices derived from the final solutions of five representative sites at different latitudes are shown in Figure 5.5. The five sites with more than 3,000 daily solutions are selected for comparison, since the parameter correlations decrease with the addition of daily solutions. Appendix B.2 gives the results of all the 125 global sites. It can be seen from Figure 5.5 that for each the constituents at most sites, except for the equatorial site MALI, the east cosine component is correlated with the north sine component and the north cosine component is correlated with the east sine component (King, 2006). The higher the site latitude, the stronger the correlation of this pattern. Also the correlations for diurnal constituents are lower than those for semidiurnal constituents. It is seen from the regional results in Section 4.3 that ambiguity-fixing can effectively de-correlate the tidal parameters. It has been previously demonstrated that choosing not to fix integer ambiguities may introduce correlations between the east and vertical coordinates (Blewitt, 1989; King et al., 2003). Nevertheless, the effect of ambiguity resolution on the tidal displacements needs to be further investigated at a global scale.

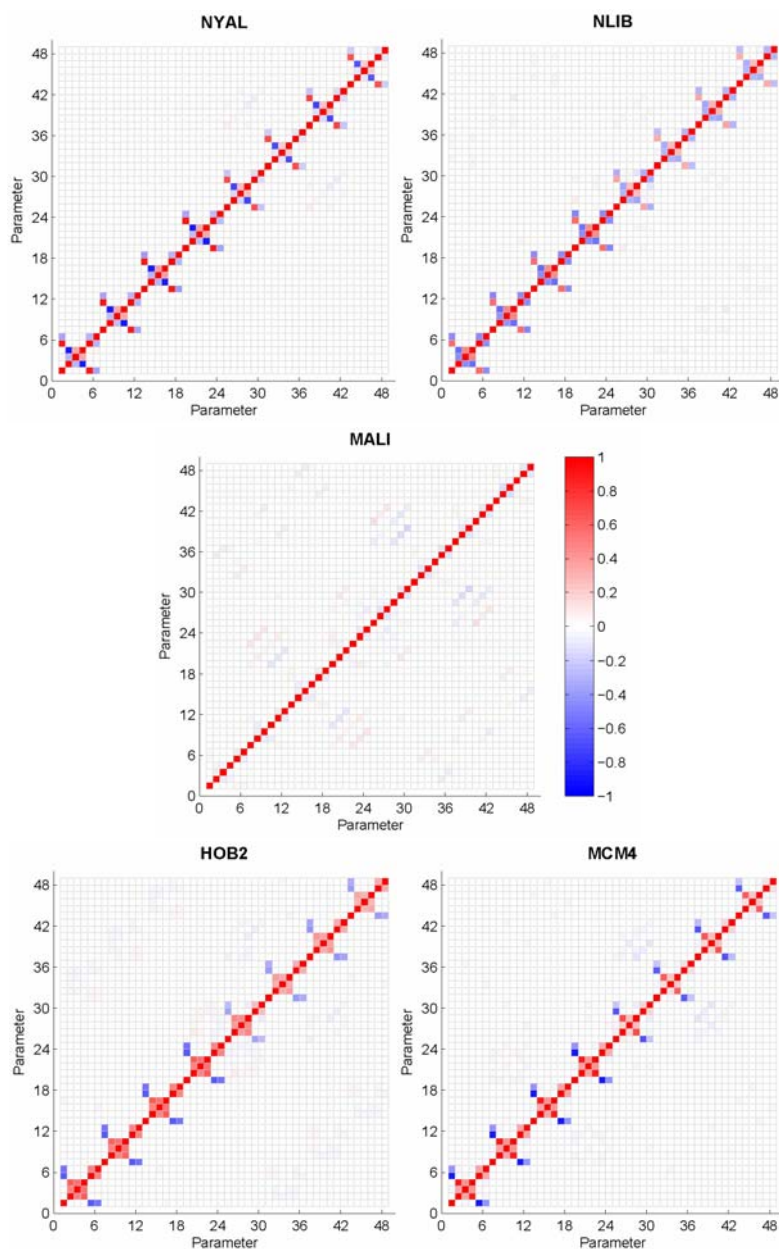


Figure 5.5 Parameter correlations of the tidal displacements at five representative sites. Parameter numbers 1-6 are the east, north, vertical cosine coefficients of M_2 , followed by their sine coefficients. The other constituent parameters (S_2 , N_2 , K_2 , K_1 , O_1 , P_1 and Q_1 in turn) are followed in the same way. The latitudes and longitudes of these sites are about $(78.9^\circ, 11.9^\circ)$ for NYAL, $(41.8^\circ, 268.4^\circ)$ for NLIB, $(-3.0^\circ, 40.2^\circ)$ for MALI, $(-42.8^\circ, 147.4^\circ)$ for HOB2, and $(-77.8^\circ, 166.7^\circ)$ for MCM4.

5.2 Results

The three-dimensional tidal displacement estimates and their formal errors (one standard deviation) for all the 125 global GPS sites are listed in Appendix B.3. The formal errors vary from 0.1 mm to 0.5 mm in the horizontal components and from 0.4 mm to 1.0 mm in the vertical component, depending on the time span and quality of GPS observations and the amplitudes of tidal displacements. Moreover, the formal errors in the east and vertical components are about 1~2 times and 2~3 times larger, respectively, than those in the north component.

5.2.1 Comparison with modelled OTL displacements

The modelled OTL displacements were calculated using the SPOTL software (Agnew, 1996). The motions of the centre of mass of the solid Earth due to the ocean tides were not corrected. Seven global ocean tide models, AG06a, NAO99b, CSR4.0, FES2004, TPXO7.1, GOT4.7 and EOT08a, were used for comparison. The summary of the ocean tide models is given in Section 2.5.1.

Figure 5.6 shows the RMS misfits between the GPS tidal estimates and seven model predictions calculated using Eq. (4.1). It can be seen from Figure 5.6 that AG06a has the worst agreement with the GPS estimates for almost all the constituents, especially for M_2 , indicating that this model is not suitable for OTL corrections in geodetic data analysis. The NAO99b and CSR4.0 models seem to offer the second worst agreement, mainly for the M_2 and O_1 constituents. However, the differences

are insignificant compared with the four most recent models. The GOT4.7 and EOT08a models appear to have a good agreement for M_2 in the vertical component, due to the improvements in tidal modelling in shallow-water areas. Overall, from a global view, FES2004, TPXO7.1, GOT4.7 and EOT08a exhibit the quite similar, best performance in terms of agreement with the GPS estimates.

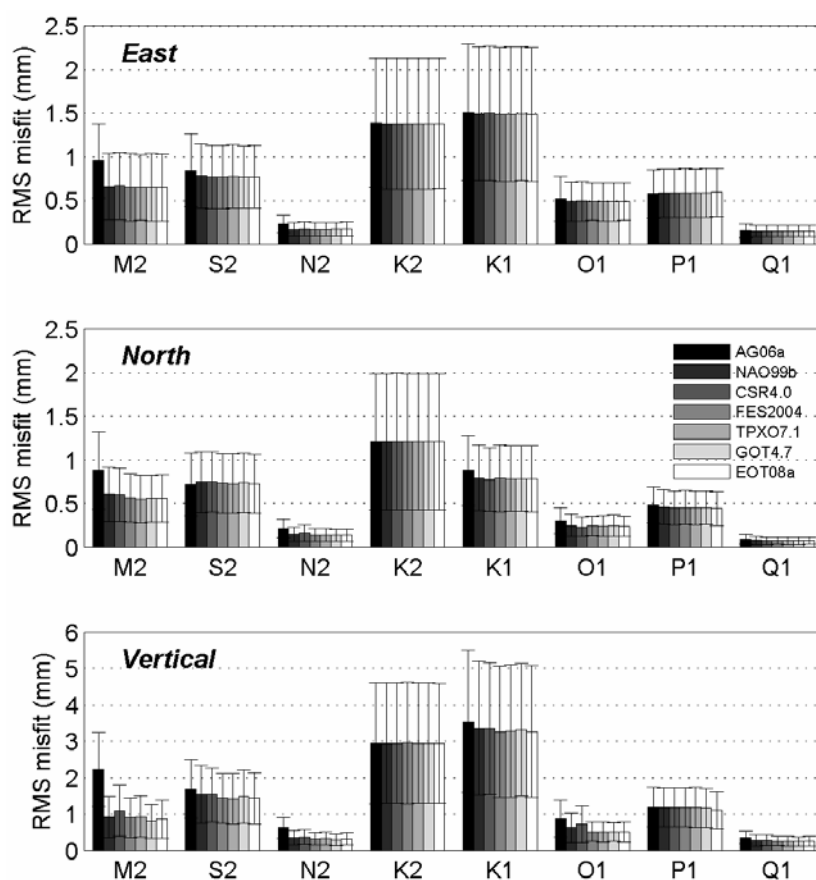


Figure 5.6 RMS misfits of the GPS tidal displacement estimates to the model predictions. The misfit bars from left (black) to right (white) represent AG06a, NAO99b, CSR4.0, FES2004, TPXO7.1, GOT4.7 and EOT08a, respectively. One sigma formal error bars are also shown.

Among all of the eight tidal constituents, N_2 and Q_1 have the best agreement with

the GPS estimates. The K_1 and K_2 constituents show the poorest GPS/model misfits with the largest scatters, consistent with the results from previous studies (King, 2006; Thomas et al., 2007). Their misfits of K_1 and K_2 can reach more than 1.0 mm and 3.0 mm for the horizontal and vertical components, respectively. The RMS misfits of the other four constituents, M_2 , S_2 , O_1 and P_1 , are roughly of the same order of magnitude.

Penna et al. (2008) have shown that the errors of M_2 modelled OTL displacements calculated by different software are about 1~2 mm at coastal sites adjacent to complicated coastlines and shallow seas, and better than 0.2 mm for sites more than ~150 km inland. The RMS of the vector differences between different model predictions is less than 0.4 mm at a large number of IGS sites, particularly for those inland, while discrepancies of about 3 mm arise for some of the coastal sites.

To further investigate the effects of errors in modelling OTL corrections, I have compared the RMS misfits between the GPS estimates and FES2004 model predictions for all the 125 sites, 45 inland sites located more than 150 km from the coast and 80 coastal sites within 150 km of the coastline (see Figure 5.7). The misfits for inland sites are less than those for coastal sites at the M_2 , N_2 , O_1 , P_1 and Q_1 frequencies. The differences in the vertical component are more significant. For example, the misfits of M_2 in the vertical component are 0.4 mm and 1.0 mm for inland and coastal sites, respectively. Since the poorest GPS/model misfits of K_1 and K_2 are mainly caused by the GPS-related errors, we cannot distinguish the misfit

differences between the inland and coastal sites. It is interesting to notice that the misfits of S_2 have no reduction for inland sites, indicating that the errors in modelling OTL is negligible compared to other error sources.

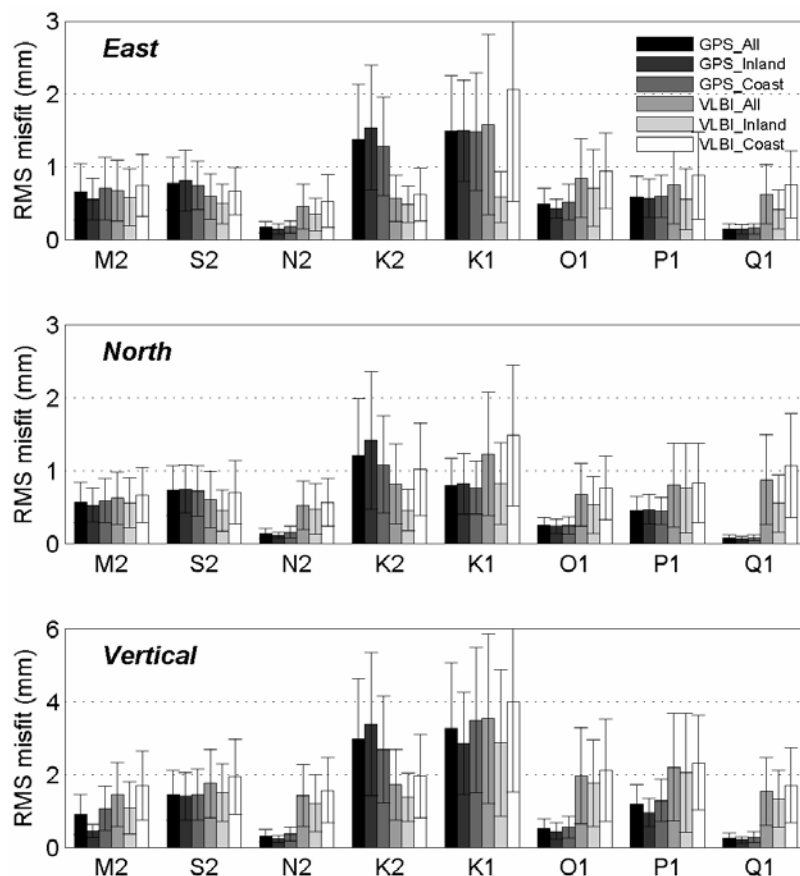


Figure 5.7 Misfits of the GPS and VLBI estimates to the FES2004 predictions. The misfit bars from left (black) to right (white) are based on all the 125 GPS sites, 45 inland GPS sites located more than 150 km from the coast, 80 coastal GPS sites within 150 km of the coastline, all the 40 VLBI sites, 18 inland VLBI sites located more than 150 km from the coast and 22 coastal VLBI sites within 150 km of the coastline, respectively. One sigma formal error bars are also shown on top of the misfit bars.

Figure 5.8 shows a box-and-whisker plot of the residuals (magnitudes of the vector differences between the GPS estimates and FES2004 model values) for both the inland sites and coastal sites. Large residuals exist at some of the coastal sites in the M_2 , N_2 , O_1 , P_1 and Q_1 frequencies. The largest residual in the vertical component reaches up to 2.7 mm for the M_2 constituent (at site QAQ1 in Greenland), and 1.6 mm for the O_1 constituent (at site KERG in Kerguelen Islands). The residuals for the S_2 , K_2 and K_1 constituents display a relatively large distribution range. The magnitudes in the vertical component reach up to 2.9 mm (DGAR), 9.1 mm (BJFS) and 8.7 mm (SEY1) for the S_2 , K_2 and K_1 constituents, respectively, which are two times larger than those for the horizontal components.

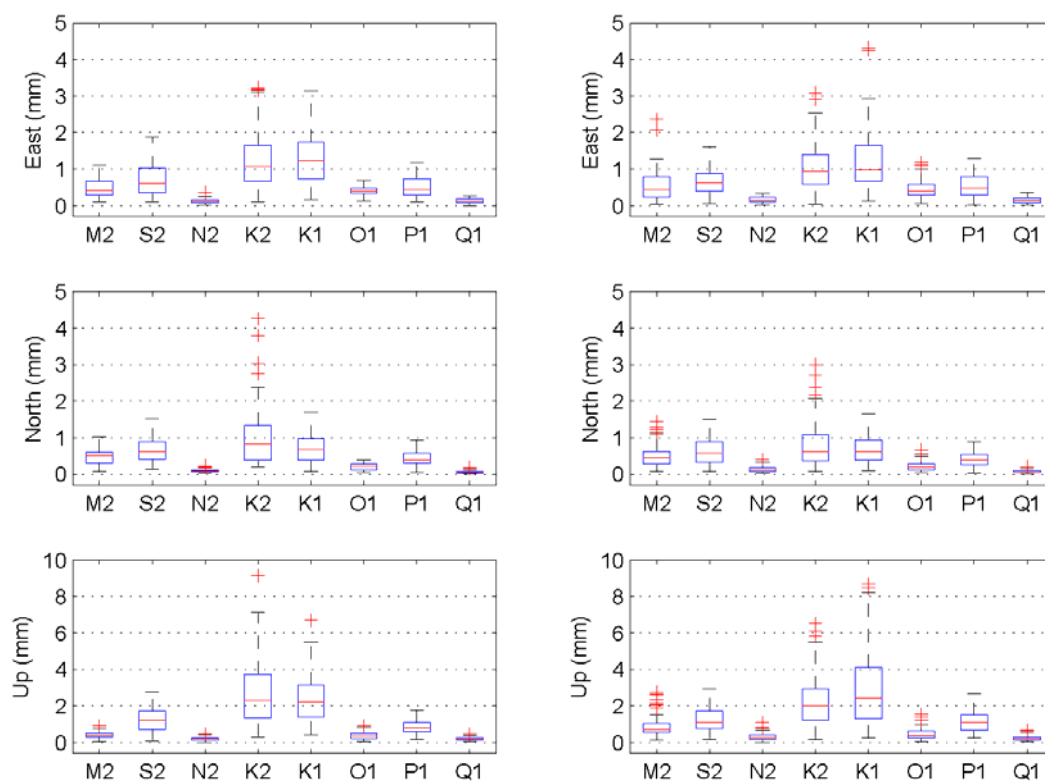


Figure 5.8 Box and whisker plot of the amplitudes of the vector differences between the GPS estimates and FES2004 predictions for 45 inland sites (left panel) and 80 coastal sites (right panel). The box describes the lower quartile, median and upper quartile values. The whiskers represent 1.5 times the interquartile range, and the plus signs represent outliers beyond the ends of the whiskers.

To assess the level of agreement of the GPS and model estimates, a weighted root-mean-square (WRMS) statistic was calculated. The WRMS of the vector differences between the GPS and model estimates for constituent j in each coordinate component k is defined as

$$\text{WRMS}_{j,k} = \left(\frac{\sum_{n=1}^N \left(\frac{|Z_{j,k,n}|}{\sigma_{j,k,n}} \right)^2}{\sum_{n=1}^N \frac{1}{\sigma_{j,k,n}^2}} \right)^{1/2} \quad (5.1)$$

where $Z_{j,k,n}$ is the complex misfit between the tidal displacement estimate and the model predictions, $\sigma_{j,k,n}$ is the formal error of the corresponding tidal displacement estimate, and N is the number of the observation sites. The two indicators (RMS and WRMS) can be seen later to lead to slightly different conclusions. The RMS is an absolute value that does not take into account the formal errors, while the WRMS is probably more realistic in terms of model evaluation.

The total WRMS of the eight semidiurnal and diurnal constituents for each coordinate component k is defined as

$$\text{WRMS}_k = \left(\sum_{j=1}^8 \text{WRMS}_{j,k}^2 \right)^{1/2} \quad (5.2)$$

Table 5.1 displays the WRMS differences between the GPS tidal displacement estimates and the FES2004 model predictions for the eight constituents. The statistical results are basically similar to the RMS misfits in Figure 5.6. It is again apparent that the WRMS misfits for the inland sites are smaller than those for the coastal sites in the M_2 , N_2 , O_1 , P_1 and Q_1 frequencies. The WRMS misfit of M_2 in the vertical component is about 0.43 mm for the inland sites, more than two times

smaller than that for the coastal sites. However, the S_2 constituent has larger RMS misfits for the inland sites than the coastal sites in all the three components. The K_1 and K_2 have the largest WRMS misfits (up to 1.5 mm and 3 mm in the horizontal and vertical components, respectively). The WRMS misfits of the N_2 and Q_1 constituents for the inland sites are less than 0.15 mm and 0.22 mm in the horizontal and vertical components, respectively, and even less than the formal errors of the GPS estimates.

Table 5.1 The WRMS misfits of the residual amplitudes of the GPS and VLBI tidal displacement estimates with respect to the FES2004 model

Obs.	k	Sites ^a	M_2	S_2	N_2	K_2	K_1	O_1	P_1	Q_1	Total
GPS	East	All	0.64	0.72	0.16	1.32	1.43	0.44	0.55	0.14	2.29
		Inland	0.55	0.78	0.14	1.46	1.47	0.40	0.53	0.14	2.39
		Coast	0.69	0.68	0.17	1.22	1.40	0.47	0.56	0.14	2.23
	North	All	0.55	0.70	0.13	1.03	0.78	0.24	0.43	0.07	1.65
		Inland	0.54	0.75	0.12	1.21	0.84	0.24	0.47	0.06	1.82
		Coast	0.56	0.67	0.14	0.89	0.74	0.24	0.41	0.08	1.53
	Vertical	All	0.86	1.33	0.29	2.77	2.75	0.45	1.09	0.22	4.39
		Inland	0.43	1.37	0.22	3.05	2.50	0.37	0.89	0.19	4.31
		Coast	1.06	1.30	0.33	2.55	2.93	0.51	1.21	0.24	4.45
VLBI	East	All	0.40	0.44	0.25	0.41	0.70	0.49	0.36	0.36	1.25
		Inland	0.35	0.39	0.22	0.39	0.43	0.41	0.30	0.29	1.00
		Coast	0.48	0.50	0.28	0.45	0.99	0.59	0.45	0.46	1.58
	North	All	0.43	0.35	0.28	0.41	0.61	0.32	0.37	0.40	1.14
		Inland	0.42	0.30	0.22	0.31	0.52	0.25	0.32	0.31	0.97
		Coast	0.44	0.42	0.36	0.53	0.74	0.41	0.44	0.51	1.39
	Vertical	All	0.84	1.29	0.87	1.14	1.58	1.03	1.12	0.87	3.16
		Inland	0.69	1.11	0.70	1.13	1.39	0.99	0.95	0.87	2.83
		Coast	1.04	1.53	1.11	1.14	1.85	1.10	1.34	0.87	3.63

All values are in millimetres.

^a For the GPS sites, All, Inland and Coast represent all the 125 sites, 45 inland sites more than 150 km from the coast and 80 coastal sites within 150 km of the coastline, respectively; for the VLBI sites, All, Inland and Coast represent all the 40 sites, 18 inland sites more than 150 km from the coast and 22 coastal sites within 150 km of the coastline, respectively.

The total WRMS misfits between the GPS estimates and seven model predictions are listed in Table 5.2. In terms of the total WRMS misfits, the differences among models are extremely small, except that AG06a is inferior. The four most recent models (FES2004, TPXO7.1, GOT4.7 and EOT08a) appear to give the best OTL predictions. The total WRMS misfits in the horizontal component for the inland sites are less than those for the coastal sites, mainly caused by the large RMS misfits of K_1 and K_2 .

Table 5.2 The total WRMS misfits of the residual amplitudes of the GPS and VLBI tidal displacement estimates with respect to the model predictions

Obs.	k	Sites ^a	AG 06a	NAO 99b	CSR 4.0	FES 2004	TPXO 7.1	GOT 4.7	EOT 08a
GPS	East	All	2.46	2.31	2.31	2.29	2.29	2.30	2.30
		Inland	2.56	2.39	2.39	2.39	2.38	2.39	2.39
		Coast	2.40	2.25	2.25	2.23	2.23	2.23	2.23
	North	All	1.84	1.66	1.66	1.65	1.64	1.65	1.64
		Inland	2.07	1.83	1.82	1.82	1.82	1.82	1.82
		Coast	1.67	1.54	1.54	1.53	1.52	1.53	1.52
	Vertical	All	5.13	4.47	4.54	4.39	4.41	4.41	4.37
		Inland	5.11	4.34	4.36	4.31	4.35	4.34	4.32
		Coast	5.14	4.57	4.68	4.45	4.46	4.46	4.41
VLBI	East	All	1.60	1.25	1.26	1.25	1.24	1.24	1.25
		Inland	1.42	0.99	1.01	1.00	1.00	0.99	0.99
		Coast	1.85	1.58	1.59	1.58	1.56	1.58	1.59
	North	All	1.40	1.15	1.16	1.14	1.15	1.15	1.14
		Inland	1.29	0.98	0.98	0.97	0.99	0.97	0.96
		Coast	1.56	1.39	1.43	1.39	1.39	1.40	1.40
	Vertical	All	3.88	3.25	3.31	3.16	3.20	3.21	3.16
		Inland	3.49	2.86	2.85	2.83	2.88	2.87	2.83
		Coast	4.45	3.80	3.94	3.63	3.67	3.70	3.63

All values are in millimetres.

^aThe sites are the same as in Table 5.1.

5.2.2 Comparison with VLBI estimates

Petrov and Ma (2003) estimated three-dimensional position variations at 40 sites in 32 frequencies using three million observations from 1980 to 2002. In their study, computation of theoretical time delays generally follows the procedure in the IERS Conventions 1996 (McCarthy, 1996), except that displacements due to solid Earth tides were expressed in the frequency domain rather than in the time domain. Results of the recent harmonic site position variations solution (Solution ID: olc_24d) used in this study are available at ¹³. Since the VLBI observations are not as uniform as the GPS observations, the formal uncertainties of VLBI estimates vary by an order of magnitude, ranging from 0.1 mm to 1.5 mm in the vertical component and from 0.4 mm to 5.0 mm in the horizontal components.

The GPS and VLBI estimates of tidal displacements at eight principal semidiurnal and diurnal frequencies were compared by Thomas et al. (2007) using the results at 25 co-located sites. Their results have shown that the accuracy of GPS estimates in the vertical component is equivalent to or better than that the VLBI estimates for all the constituents except K_2 . They have also concluded that one cannot distinguish between the GPS and VLBI estimates of tidal displacements and the present ocean tide model predictions are accurate to within the current observation noises of these techniques at the global scale.

¹³ http://astrogeo.org/harpos/olc_24d_addons.html

The VLBI estimates of all the 40 sites were compared with the model predictions in terms of the RMS misfits, as shown in Figure 5.9. It can be seen that the AG06a predictions also exhibit the poorest agreement with the VLBI estimates, which is consistent with the GPS estimates, although only the misfits of M_2 are significant. The VLBI/model RMS misfits are almost at the same order for all the constituents, except for K_2 with relatively larger values.

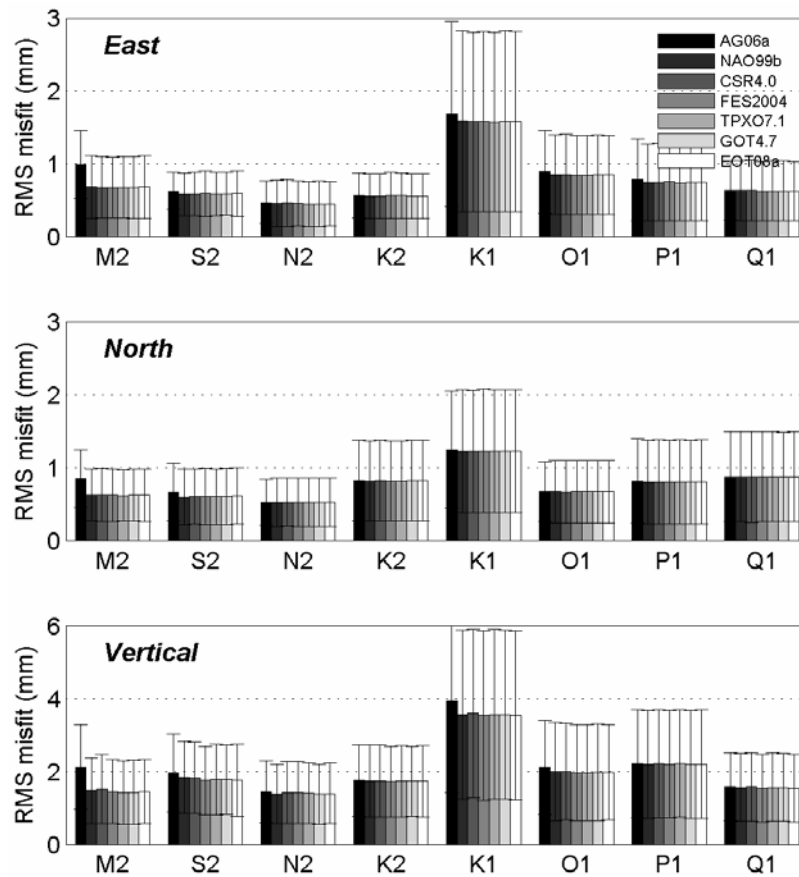


Figure 5.9 The RMS misfits of the VLBI tidal displacement estimates to the model predictions. The misfit bars from left (black) to right (white) represent AG06a, NAO99b, CSR4.0, FES2004, TPX07.1, GOT4.7 and EOT08a, respectively. One sigma formal error bars are also shown.

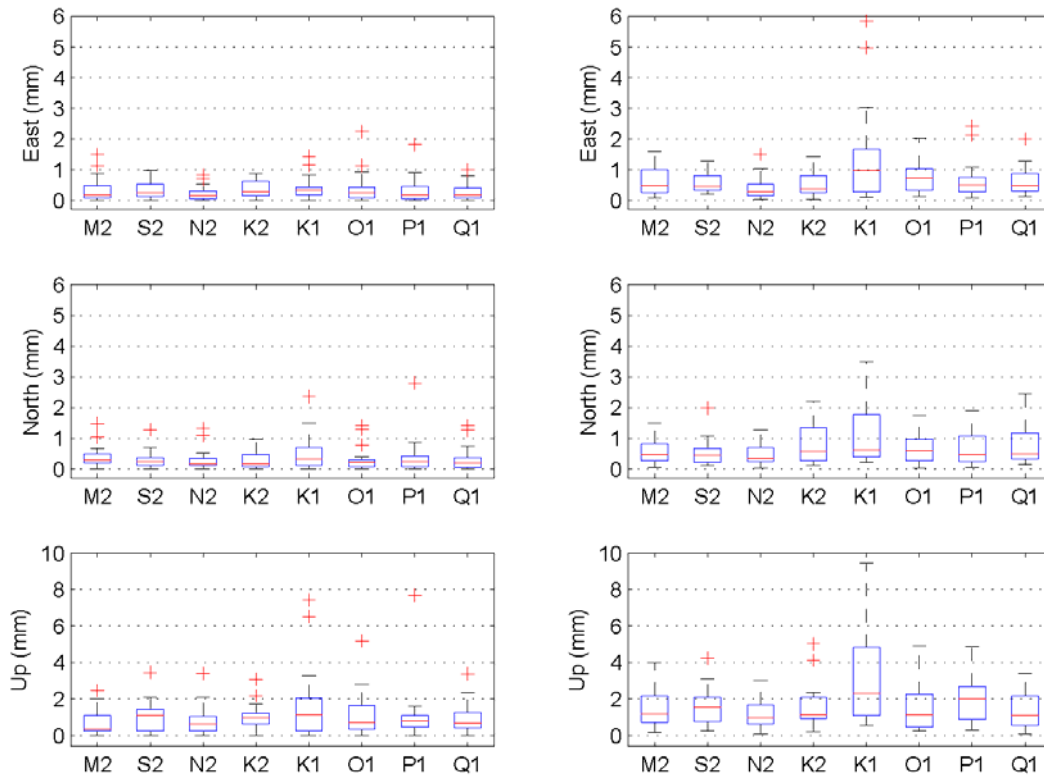


Figure 5.10 Box and whisker plot of the amplitudes of the vector differences between the VLBI estimates and FES2004 predictions for 18 inland sites (left panel) and 22 coastal sites (right panel). The box describes the lower quartile, median and upper quartile values. The whiskers represent 1.5 times the interquartile range, and the plus signs represent outliers beyond the ends of the whiskers.

The RMS misfits between the VLBI estimates and FES2004 model predictions are also shown in Figure 5.7 for comparison with the GPS/model misfits. The VLBI/model RMS misfits for the inland sites are less than those for the coastal sites at all the tidal frequencies. The GPS/model misfits are smaller than the VLBI/model RMS misfits in all the three components for the M_2 , N_2 , O_1 , P_1 and Q_1 constituents. The VLBI/model RMS misfits are smaller than the GPS/model misfits for the horizontal components of S_2 and for all three components of K_2 . For the K_1

constituent, the RMS misfits of both the techniques are of the same order of magnitude. The distribution of the vector differences between the VLBI estimates and FES2004 predictions in Figure 5.10 shows only slight differences between the inland and coastal sites.

Compared to the RMS misfits, the WRMS statistics better represent the accuracy of the VLBI estimates as the formal errors of the VLBI estimates vary considerably across different sites. The WRMS misfits between the VLBI estimates and the FES2004 model predictions in Table 5.1 show a slightly different pattern, compared to the RMS misfits in Figure 5.7. Different from the RMS misfits, the WRMS misfits of M_2 for the VLBI sites are smaller than those for the GPS sites in the horizontal components. The WRMS misfits of both P_1 and K_1 for the VLBI sites are also smaller than those for the GPS sites in all the three components. The larger total WRMS misfits for the GPS sites result from the relatively large WRMS misfits of both K_1 and K_2 (see Tables 5.1-2). The total WRMS statistics shows that the four most recent models (FES2004, TPXO7.1, GOT4.7 and EOT08a) appear to better fit both the GPS and VLBI measurements than the older models. It should be noticed that the VLBI sites with uneven global coverage precludes definitive conclusions by this technique.

5.2.3 Spatial variations of tidal displacement residuals

Spatial variations (amplitude and phase) of the residuals between the GPS estimates and model predictions were investigated next. From the 125 sites analysed, there are

apparent large-scale spatial coherences of the residuals for most of the tidal constituents. Although different ocean tide models give quite different residuals at some of the coastal sites, the overall pattern for each constituent is unchanged. I take the FES2004 model as a reference model and illustrate the spatial patterns of the residuals between the GPS estimates and model predictions for the eight constituents, as shown in Figures 5.11-5.18. All of the figures are also attached in Appendix B.4.

In the semidiurnal frequencies, the tidal displacement residuals of M_2 , S_2 and N_2 show similar phase lags to some extent, especially in the north component, although the amplitudes of each constituent are not of the same order. For example, there are quite similar spatial patterns for the north component of M_2 , S_2 and N_2 in North America, for the north component of M_2 and S_2 in Eurasia and for the east component of M_2 and N_2 in Europe. The east component of S_2 with spatial pattern different from that of M_2 and N_2 shows large systematic residuals in Asia and west North America, but relatively small values in Europe. The amplitude can reach up to 1.9 mm at inland site KUNM in the east component (see Figure 5.11). For the vertical component, M_2 has a strong spatial coherence in North America and S_2 appears to have quite large spatial coherent residuals in Eurasia, such as at two inland sites ARTU (2.8 mm) and KIT3 (2.6 mm) (Figure 5.12). No significant spatial correlation is seen for the K_2 constituent, although its residuals are the largest compared to the other three semidiurnal constituents.

The spatial patterns of the tidal displacement residuals in the diurnal frequencies are

different from those in the semidiurnal frequencies. Similar spatial patterns can be seen more or less in the north component for all the four diurnal constituents. The residuals for the O_1 constituent show the smoothest variations across the whole Earth. The phases of the O_1 east residuals appear to have a consistent trend towards about 135° at most of the sites except for those in Australia. The O_1 vertical residuals at most of the sites in Southern Hemisphere appear to converge towards the South Pole. The spatial distributions of the residuals for the other three diurnal constituents are also illustrated in Figures 5.15, 5.17 and 5.18 and not be described in detail here.

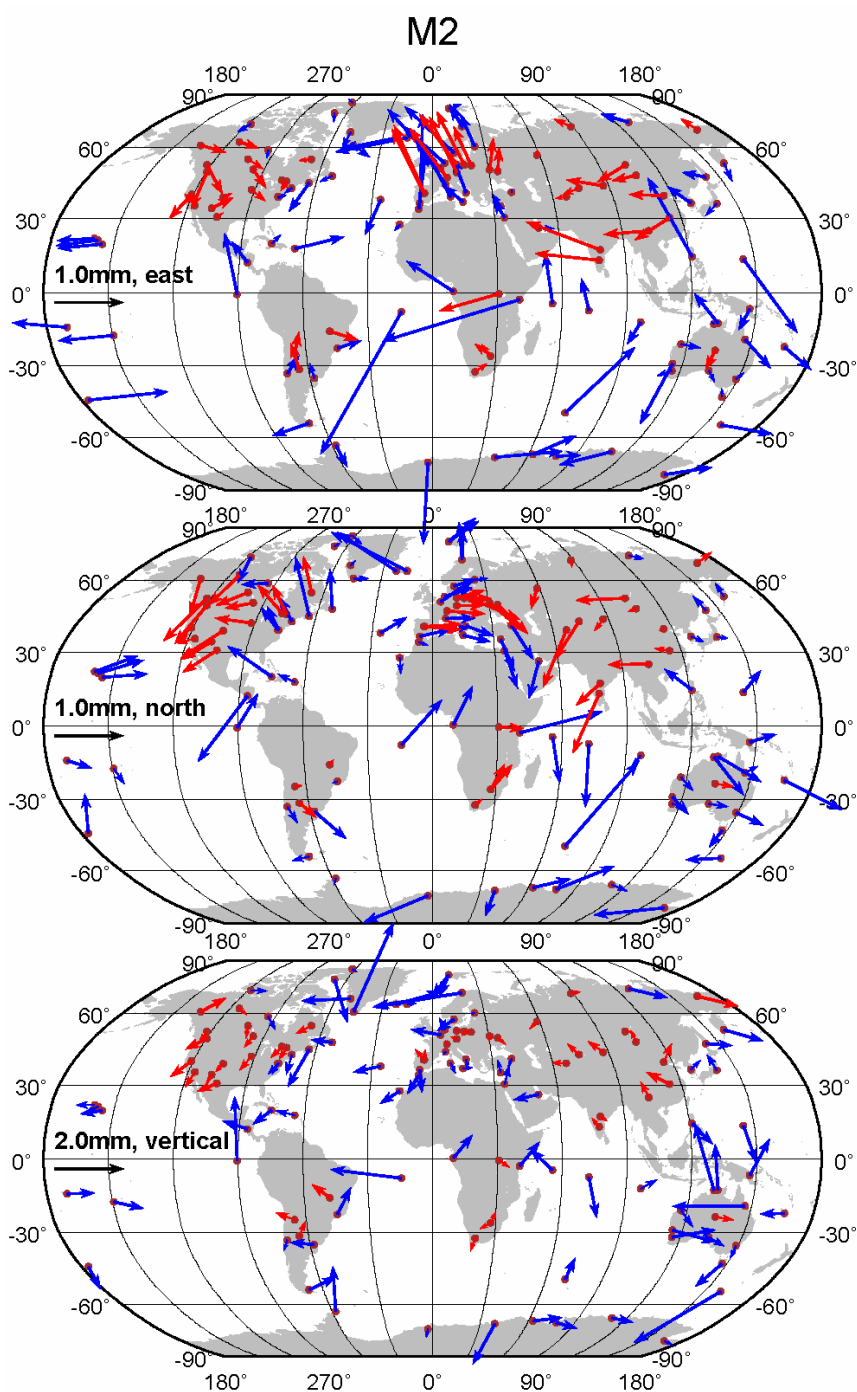


Figure 5.11 Phasor diagrams of the M_2 tidal displacement residuals after removing the FES2004 predictions. Red arrows indicate the residuals for the inland GPS sites more than 150 km from the coast; and blue arrows are for the coastal GPS sites within 150 km of the coastline. Phases increase clockwise from the upward direction.

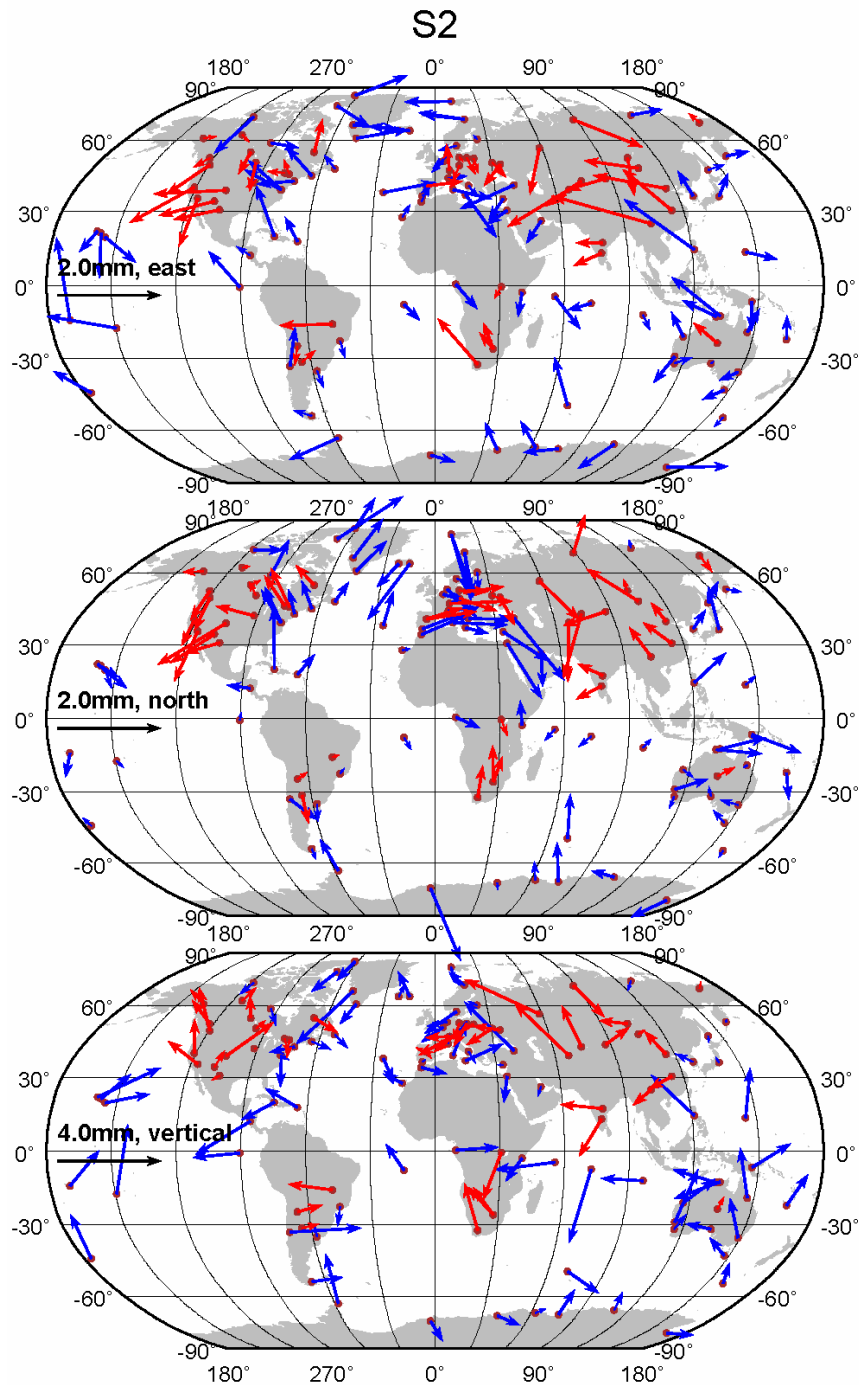


Figure 5.12 Phasor diagrams of the S₂ tidal displacement residuals after removing the FES2004 predictions. Red arrows indicate the residuals for the inland GPS sites more than 150 km from the coast; and blue arrows are for the coastal GPS sites within 150 km of the coastline. Phases increase clockwise from the upward direction.

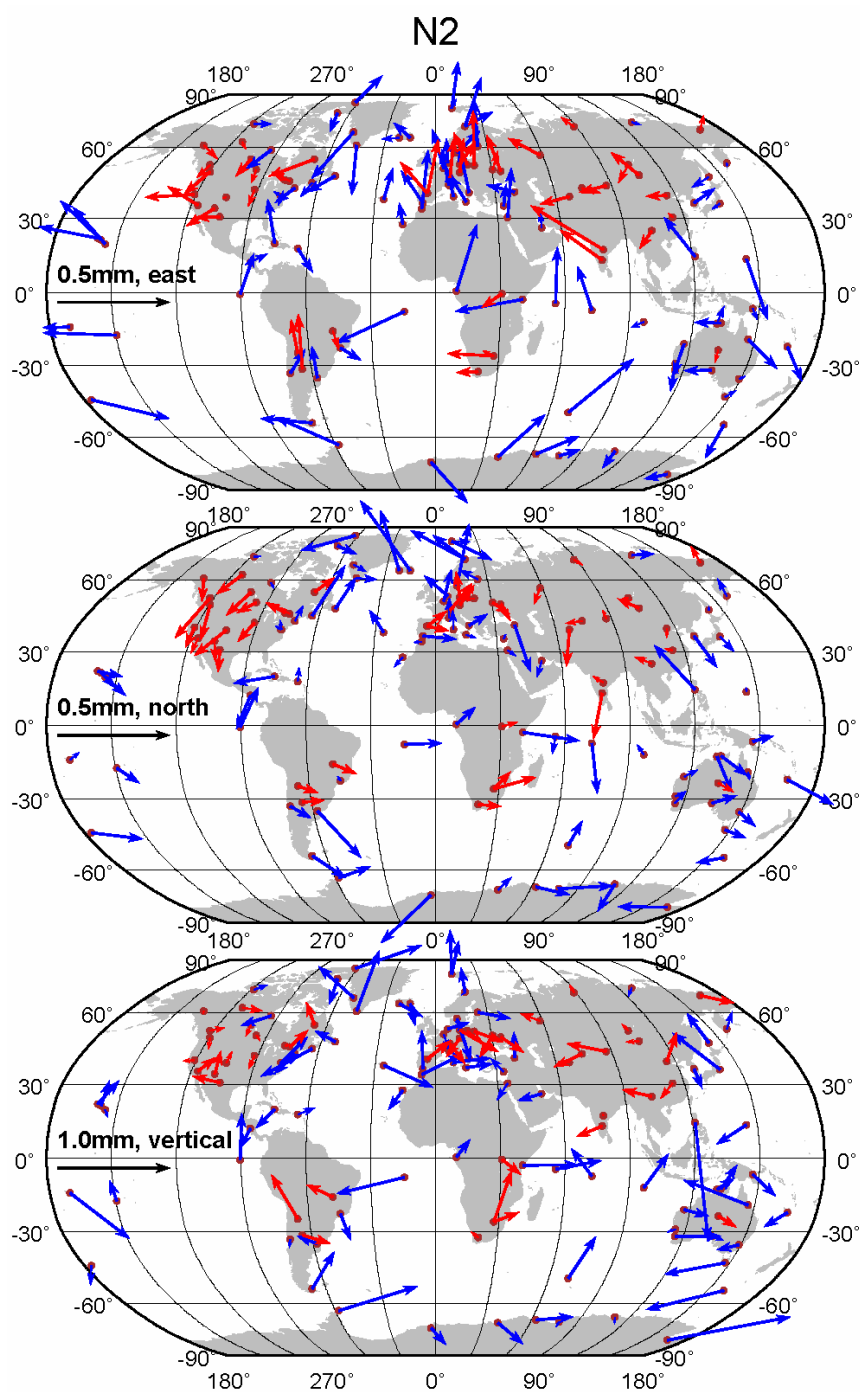


Figure 5.13 Phasor diagrams of the N_2 tidal displacement residuals after removing the FES2004 predictions. Red arrows indicate the residuals for the inland GPS sites more than 150 km from the coast; and blue arrows are for the coastal GPS sites within 150 km of the coastline. Phases increase clockwise from the upward direction.

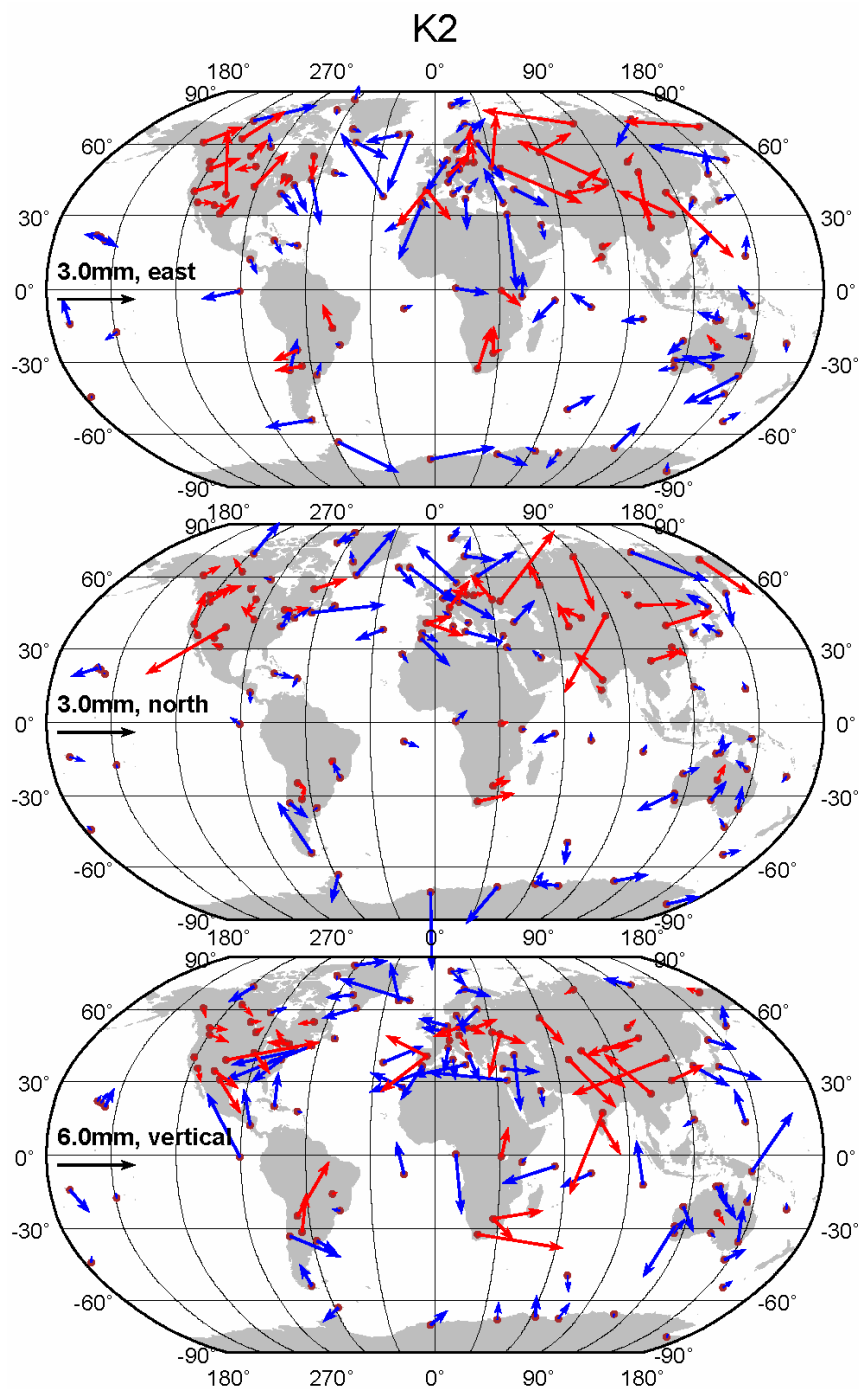


Figure 5.14 Phasor diagrams of the K₂ tidal displacement residuals after removing the FES2004 predictions. Red arrows indicate the residuals for the inland GPS sites more than 150 km from the coast; and blue arrows are for the coastal GPS sites within 150 km of the coastline. Phases increase clockwise from the upward direction.

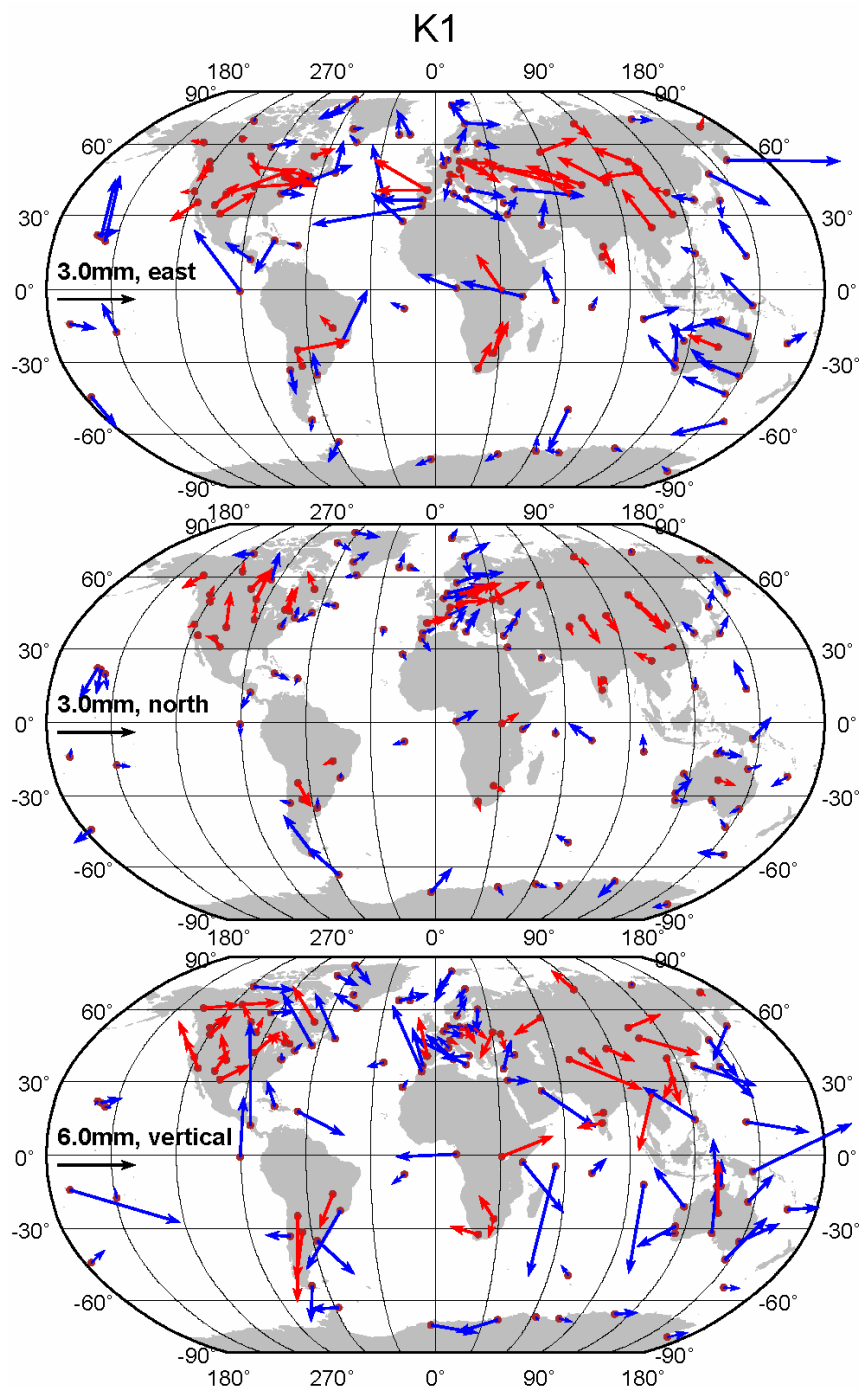


Figure 5.15 Phasor diagrams of the K_1 tidal displacement residuals after removing the FES2004 predictions. Red arrows indicate the residuals for the inland GPS sites more than 150 km from the coast; and blue arrows are for the coastal GPS sites within 150 km of the coastline. Phases increase clockwise from the upward direction.

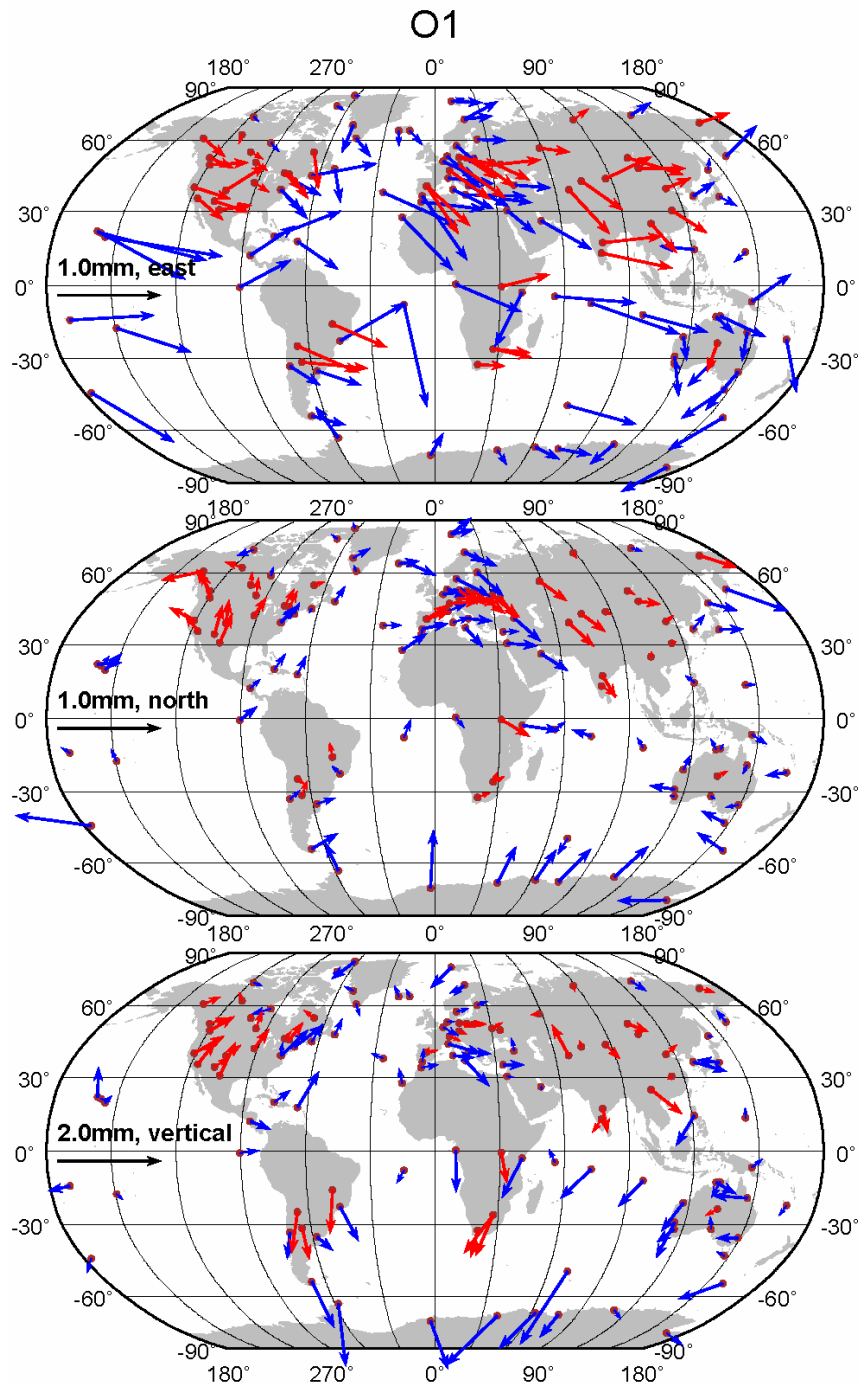


Figure 5.16 Phasor diagrams of the O₁ tidal displacement residuals after removing the FES2004 predictions. Red arrows indicate the residuals for the inland GPS sites more than 150 km from the coast; and blue arrows are for the coastal GPS sites within 150 km of the coastline. Phases increase clockwise from the upward direction.

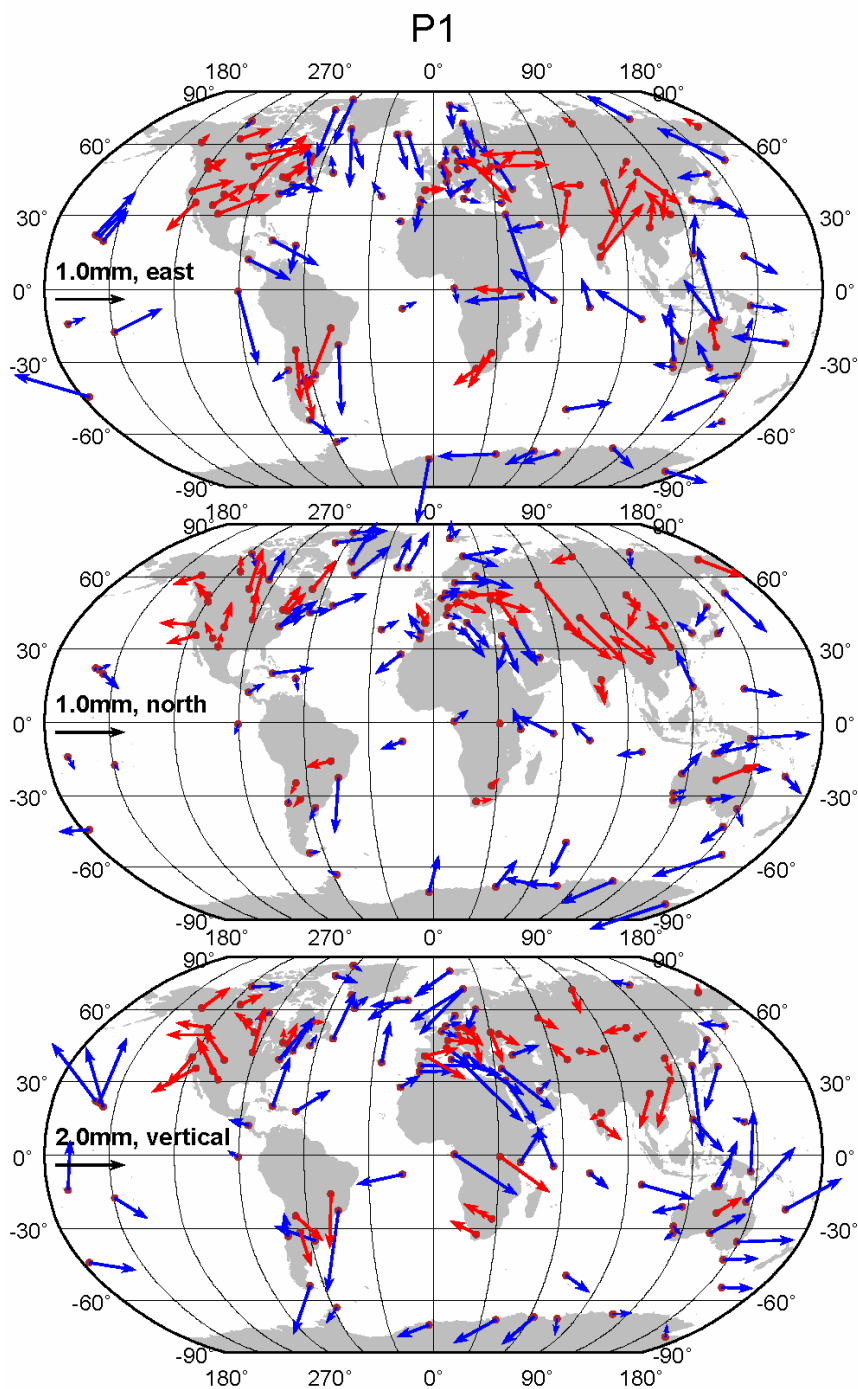


Figure 5.17 Phasor diagrams of the P_1 tidal displacement residuals after removing the FES2004 predictions. Red arrows indicate the residuals for the inland GPS sites more than 150 km from the coast; and blue arrows are for the coastal GPS sites within 150 km of the coastline. Phases increase clockwise from the upward direction.

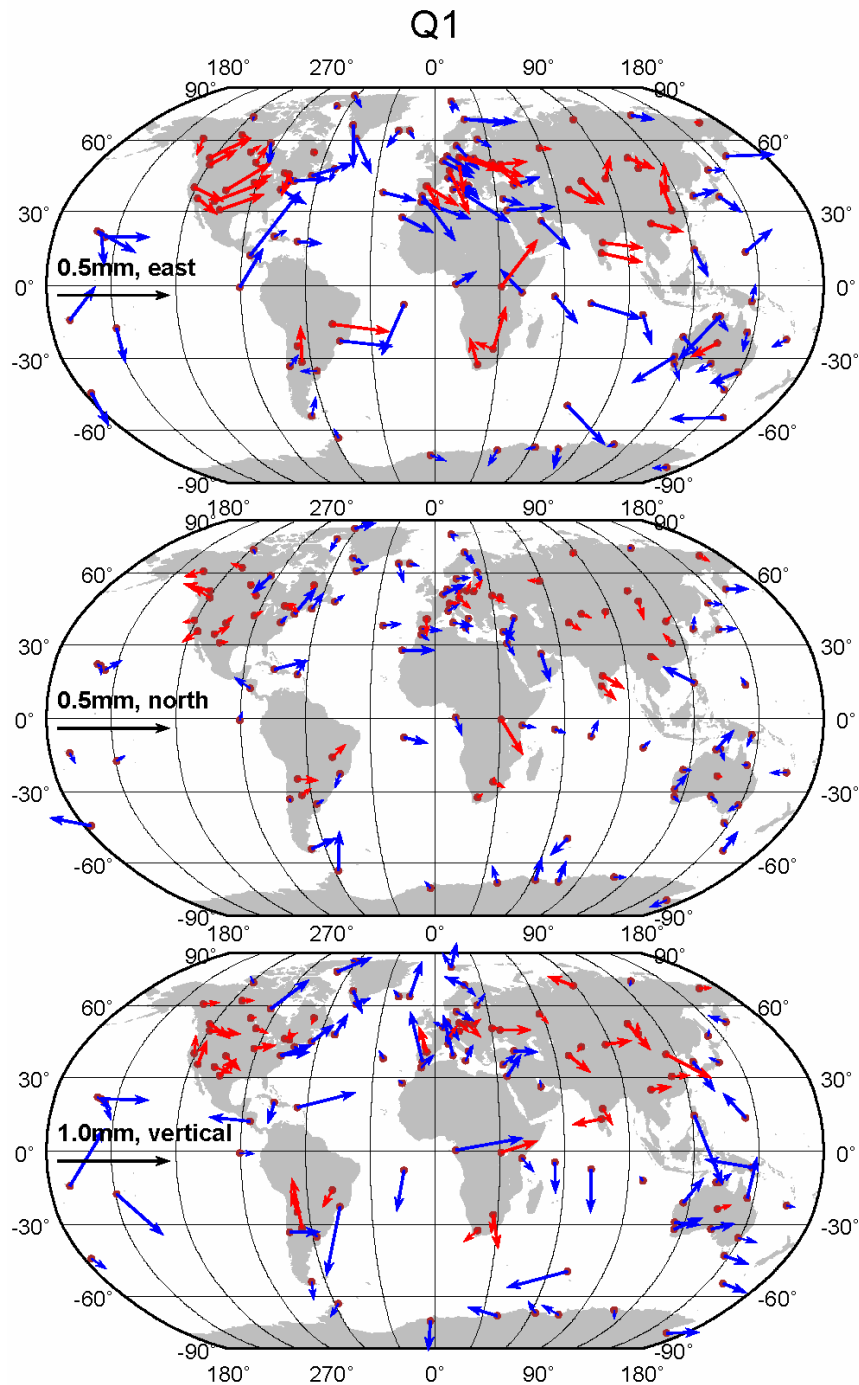


Figure 5.18 Phasor diagrams of the Q_1 tidal displacement residuals after removing the FES2004 predictions. Red arrows indicate the residuals for the inland GPS sites more than 150 km from the coast; and blue arrows are for the coastal GPS sites within 150 km of the coastline. Phases increase clockwise from the upward direction.

I also compared the spatial variations between the VLBI/model and GPS/model residuals. The distribution of the 40 VLBI sites is not as uniform as that of the GPS sites analysed in this study. Most of the VLBI sites are located in North America and Europe. Figure 5.19 shows the phasor diagrams of the M_2 residuals for both GPS and VLBI sites across North America and Europe after removing the FES2004 predictions. The GPS sites show more coherent spatial pattern than the VLBI sites. Although the VLBI/models residuals are in phase with the GPS/models residuals at some of the co-located sites, the residuals of the VLBI sites behave mostly like random noises. Phasor diagrams of the residuals at the GPS and VLBI sites for all the eight principal constituents are given in Appendix B.4. Inspection of these figures suggests that the tidal displacements derived from the VLBI measurements have much larger errors than those from the GPS observations for most of the tidal constituents except K_2 . The spatial patterns of the K_2 residuals at the VLBI and GPS sites are both random chaotic.

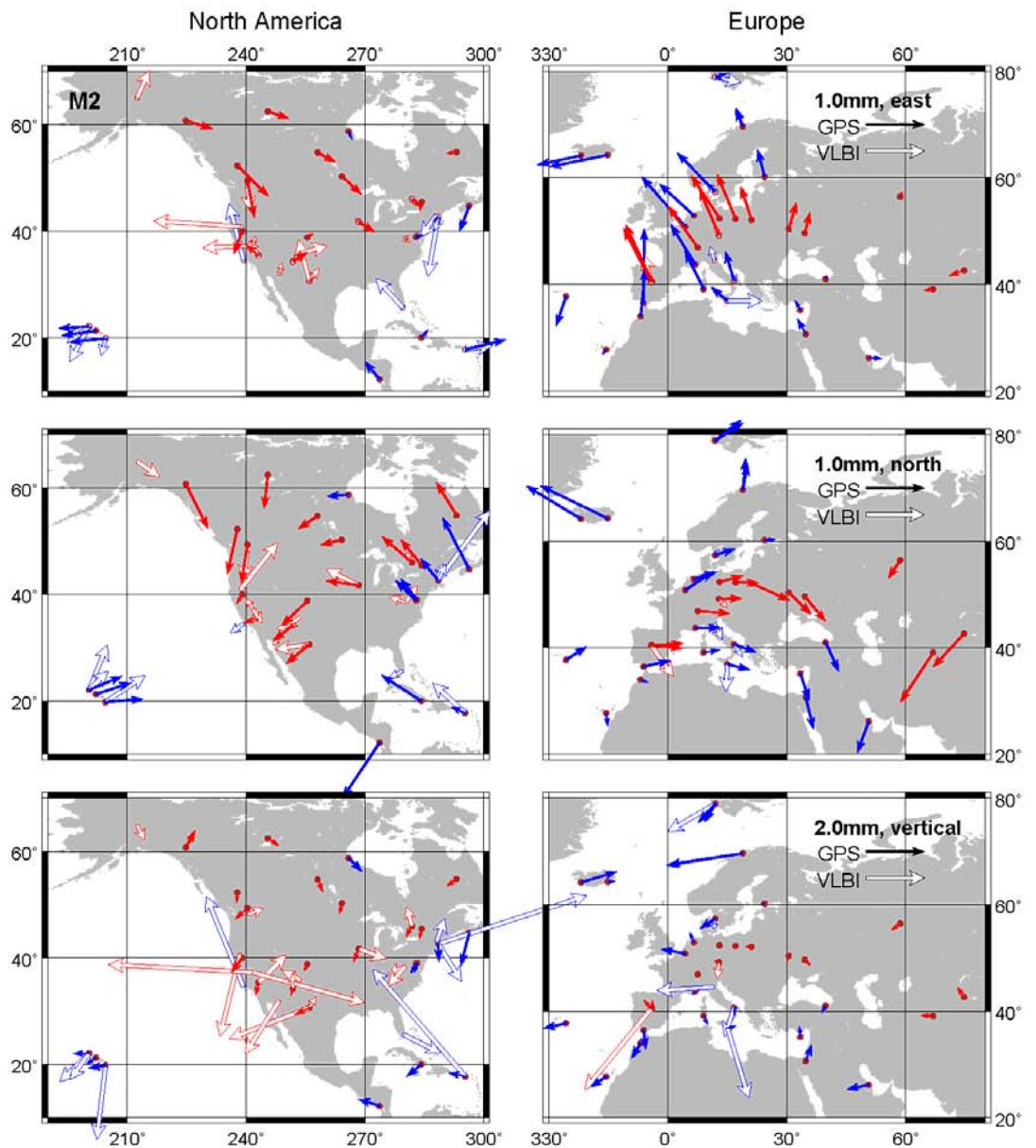


Figure 5.19 Phasor diagrams of the M_2 tidal displacement residuals after removing the FES2004 predictions in North America (left) and Europe (right). Red solid arrows are the residuals for the inland GPS sites more than 150 km from the coast; blue solid arrows are for the coastal GPS sites within 150 km of the coastline, red open arrows are for the inland VLBI sites more than 150 km from the coast; and blue open arrows are for the coastal VLBI sites within 150 km of the coastline. Phases increase clockwise from the upward direction.

5.3 Searching for mis-modelled or un-modelled tidal displacements

The results in Section 5.2 have shown that GPS is capable of estimating the tidal displacements with submillimetre accuracy in all the three components for most of the principal constituents except K_1 and K_2 . The residuals show strong systematic spatial variations. It is therefore considered that the WRMS statistics of the inland GPS sites give the lower limit of accuracy of GPS measurements if the residuals are composed of observational noises and real spatial-correlated signals. Sources of the spatially correlated residual signals can only be partially explained at present. In this section, possible contributions to the spatially correlated signals are discussed. Here five candidate sources are investigated: tidal geocentre motion, solid Earth tide modelling errors, OTL modelling errors, atmospheric loading and GPS-related errors.

5.3.1 Tidal geocentre motion

The modelled OTL values do not account for the geocentre motions due to ocean tides in order to be consistent with the JPL orbit products in this study. Numerical results show that the magnitude of subdaily tidal geocentric motion is expected at the order of several millimetres (see Table 2.4). Therefore, the GPS tidal displacement estimates should be theoretically sensitive to this motion. Scherneck (2000) demonstrated that it is possible that this large scale motion can be absorbed in the GPS orbits during GPS orbit determination. In this case, the correction for this

motion has indirectly been applied. I compared the GPS estimates with the modelled predictions corrected for the tidal geocentre motions. Results of the GPS estimates show significant discrepancies with respect to the model values with the tidal geocentre motions corrected.

To further investigate whether the GPS estimates still reserve a part of this large-scale motion, I attempt to inverse the centre-of-mass parameters using the GPS estimates (see Eq. 1.33 in Chapter 2). The estimated center-of-mass coefficients are quite small, less than 0.2 mm for all eight constituents. Also the coefficients calculated using different components (east, north and vertical) of the GPS estimates are significantly different. The findings may attribute to the fact that frame origin tides are neglected in the products of the JPL global analysis center. The regional results using JPL GPS orbits before and after 1400 GPS week also show that the tidal displacement estimates appear insusceptible to the centre-of-mass variations (see Section 4.2 for details).

In summary, the effects of geocentre motions due to ocean tides on the GPS tidal displacement estimates are insignificant. However, one cannot infer that the effects are unimportant or negligible. Using of the IGS reprocessed GPS orbit products with the center-of-mass corrections will help further clarify this issue in future analysis.

5.3.2 Solid Earth tide modelling errors

The large-scale systematic biases in the GPS/model residuals most possibly result

from deficiency of the solid Earth tide model. The accuracy of the numerical values of Love numbers is dependent on the accuracy of the Earth model used (PREM) and modelling of anelasticity. The characteristics of anelasticity at tidal periods are still considerably uncertain (Mathews et al., 1997). Mantle anelasticity causes an amplitude increase of about 1% and a phase delay of a few tenths of degree for Love numbers. The corresponding tidal displacement uncertainties could be up to a few millimetres. The effect of the mantle's lateral heterogeneities on solid Earth tide deformations is appreciable below 1%. A recent study of Metivier and Conrad (2008) has shown that maximum vertical perturbation of surface displacements is about 0.3 mm, equivalent to or below the current accuracy of GPS measurements. The shorter-wavelength lateral changes in Earth structure may result in larger effects. Zurn et al. (1976) used a finite element model to calculate the effect of geological structure associated with the downgoing lithospheric slab beneath Alaska. They found that this effect on the solid Earth tide displacement reaches up to 0.8%.

The largest deviations from spherical symmetry of the Earth are its rotation and ellipticity. The latitude effects on Love numbers due to rotation and ellipticity seemed to be well established by previous theories (Mathews et al., 1995). For displacements, Mathews et al. (1997) has shown that the effect are at most 1 mm. Nevertheless, it is difficult to verify the latitude dependence of Love numbers caused by the effects of rotation and ellipticity using tidal observations up to now. Another important effect to be taken into account is the resonant behaviour of Love numbers from NDFW at the diurnal band. The relatively large uncertainty of K_1 tidal

displacements makes the GPS technique difficult to provide useful information on the NDFW resonance at present.

The analysis discussed above demonstrates that the uncertainties of modelling solid Earth tides in IERS Conventions 2003 exceed the errors of the GPS tidal measurement estimates in this study. Therefore, GPS observations of tidal displacements may impose important constraints on the solid Earth tide model, especially on the anelasticity of the Earth.

5.3.3 OTL modelling errors

As discussed in Section 2.5, the accuracy of modelled OTL displacements depends on the ocean tide model, Green's function, coastline and numerical scheme of loading computation. Penna et al. (2008) have assessed the accuracy of modelled OTL displacements of M_2 . Their study has shown that the OTL displacements calculated using different software agree at 1~2 mm level for coastal sites, and are better than 0.2 mm for sites more than about 150 km inland.

The accuracy of ocean tide models has always been considered the largest contributor to the uncertainty of OTL displacements, particularly for areas close to shallow seas. Height errors between different modern models can reach up to about 3 mm at IGS sites (Penna et al., 2008) and be as high as around 8 mm in some coastal areas such as the Weddell Sea and Ross Ice Shelf (Penna et al., 2007). The error in the horizontal components is typically about one third that in the vertical

component. It is worth noting that the greater errors may appear if the existing models fail to provide exact information on certain seas.

The relatively large GPS/model misfits at coastal sites in this study indicate that the improvement of ocean tide modelling is still an important issue in high-precision geodetic OTL corrections. No ocean tide model could provide completely satisfactory results for all regions in the world. Further research is still required for evaluating which model is most appropriate for different parts of the world. This study demonstrates that the GPS technique with an extensive spatial coverage provides an independent tool to constrain ocean tide models. For some coastal GPS sites with large uncertainties of the OTL prediction, an alternative approach is to use the GPS tidal displacements instead of the model predictions.

5.3.4 Atmospheric tide loading

Atmospheric tides excited mainly by solar heating also induce periodic motions of the Earth's surface. A model for S_1 and S_2 atmospheric tide loading proposed by T. M. van Dam and R. D. Ray is currently considered to be included in the site displacement models of the IERS Conventions. This model is based on the S_1 and S_2 atmospheric tidal model of Ray and Ponte (2003). The amplitudes of the S_1 and S_2 ATL deformation in the vertical component reach 1~2 mm at the equatorial sites and reduce to negligible magnitudes at the poles. Horizontal deformations are smaller by one order of magnitude. However, the S_1 and S_2 ATL effects are currently not included in almost all of the global analysis centers.

I compared the S_2 tidal displacement estimates with the S_2 ATL displacement predictions calculated by T. M. van Dam^{<14>} as shown in Figure 5.20. It is found that the modelled ATL displacements are too small in the horizontal components (less than 0.2 mm) to explain the large GPS/model residuals in this study. Applying the ATL models slightly changes the spatial pattern of the residuals in the vertical component. However, the amplitudes of the vertical residuals are not reduced in general. In addition, the P_1 and K_1 residuals may also include the effects of S_1 ATL due to their frequencies being very close. From this analysis at the global scale, I conclude that ATL is indiscernible from the S_2 tidal displacement estimates at present.

¹⁴ <http://www.ecgs.lu/atm/>

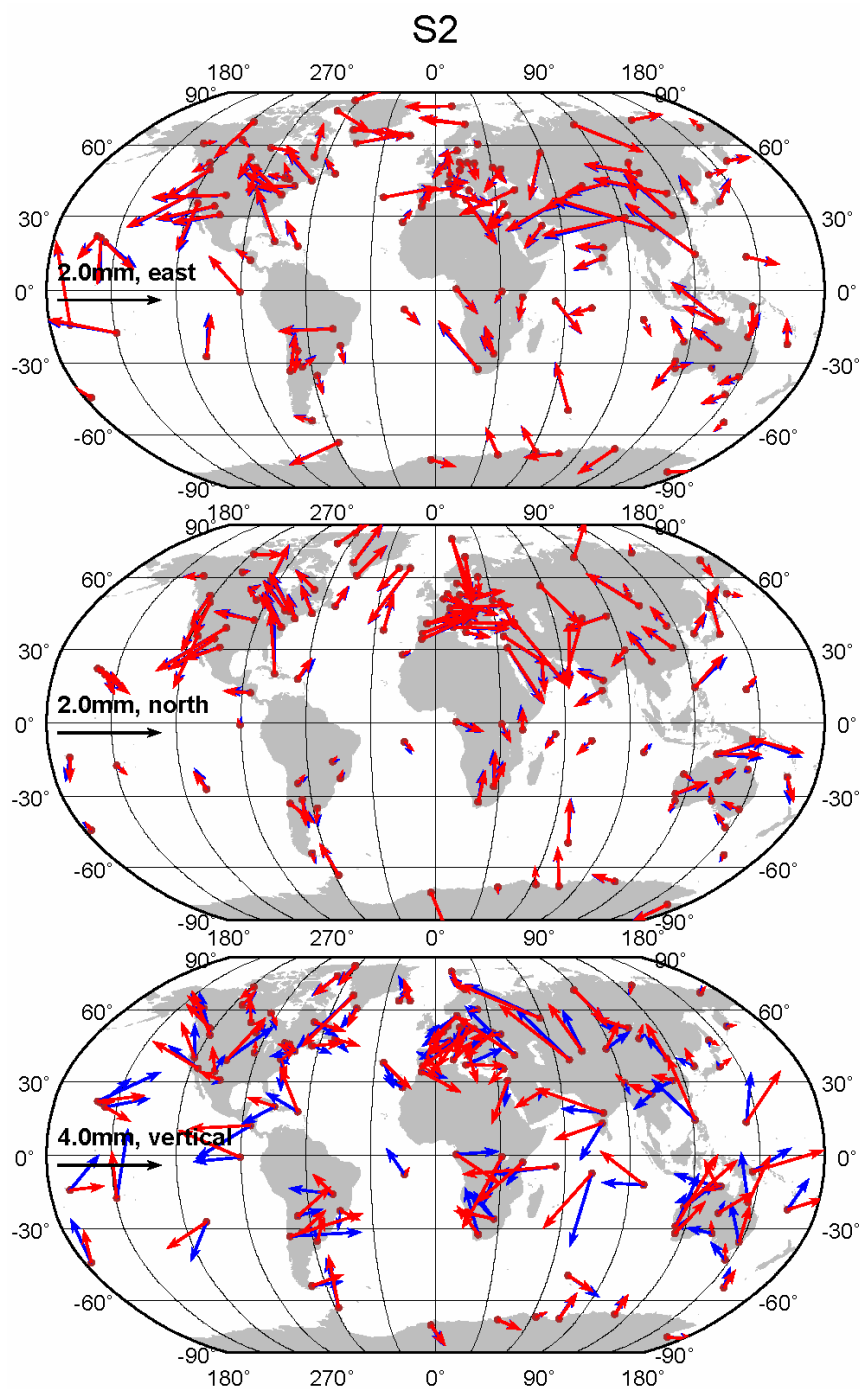


Figure 5.20 Phasor diagrams of the S₂ tidal displacement residuals before (blue arrows) and after (red arrows) removing the effects of modelled atmospheric tide loading. The FES2004 model is used to remove the modelled OTL effects. Phases increase clockwise from the upward direction.

5.3.5 GPS-related errors

The GPS-related errors affecting tidal displacement estimates include inadequate orbit modelling, tropospheric mapping function and a priori hydrostatic delay errors, higher-order ionospheric delays and multipath effects. Previous studies suggested that the large uncertainties of GPS tidal displacement estimates at K_1 and K_2 frequencies come from the GPS satellite orbit errors and multipath effects related to the satellite constellation repeat period corresponding to the K_1 period, and the satellite orbital period corresponding to the K_2 period (Schenewerk et al., 2001; King et al., 2005; King, 2006). By examining long-running, short-baseline ($\ll 1$ km) time-series, King and Williams (2009) further suggested that the majority of the GPS/model tidal residuals of K_1 and K_2 is due to satellite orbit mismodelling and GPS signal propagation effects (including tropospheric and higher-order ionospheric effects) rather than local site effects such as multipath.

The results from the regional analysis discussed in Chapter 4 show that the residual displacements of K_1 and K_2 still exhibit the spatial coherence at small scale (about 50 km^2) and the site-dependent errors, such as multipath effects, are at the same order magnitude. On the other hand, the results from the global analysis show that the K_1 residuals exhibit a large-scale spatial pattern while the K_2 residuals show a different pattern with a greater randomness. So the mechanism responsible for the K_1 and K_2 residuals is still an open question.

The tidal displacement estimates of the solar constituents S_2 and P_1 have seasonal

fluctuations and relatively larger biases. Besides the genuine tidal sources discussed above, GPS systematic errors may also bias the two constituents. Higher-order ionospheric effects and errors in modelling the tropospheric delays (due to unmodelled hydrostatic delays and/or mapping function errors) are the most likely sources.

5.4 Summary

Three-dimensional tidal displacements of 125 IGS05 reference sites of eight principal semidiurnal and diurnal constituents were obtained from analysis of GPS observations from 1996 to 2006. Comparison of the GPS and VLBI estimates of tidal displacements with the predictions of seven recent ocean tide models has shown that GPS is capable of determining the tidal displacements with accuracy equivalent to or better than VLBI for seven principal constituents except K_2 . When the spatially coherent signals of residuals between the GPS and model estimates are considered to be real displacement signals, the WMRS misfits indicate the lower bound for the accuracy of the GPS tidal displacement estimates. The WRMS misfits also indicate that GPS offers tidal displacements with sub-millimetre accuracy in all the three components for all the constituents except K_1 and K_2 .

The AG06a model shows apparent anomalous agreement with both the GPS and VLBI estimates, suggesting that this model is not appropriate to calculate OTL corrections. The four most recent models (FES2004, TPXO7.1, GOT4.7 and EOT08a) fit the GPS estimates equally well at global scale, although they provide

quite different agreements in some coastal areas, especially for the vertical displacements. Moreover, the vertical RMS misfits of coastal sites within 150 km of the coastline are larger than those of sites more than 150 km inland for most of the prominent constituents, suggesting that uncertainty still exists in all the ocean tide models in shallow water seas. For the inland sites, the differences of the OTL predictions between different ocean tide models become indistinguishable by GPS estimates (less than 0.4 mm in the vertical component).

After removing the modelled OTL displacements, the residual displacements show a pattern of large scale spatial coherence for all the constituents except K_2 . At present, the mechanism to explain the spatial coherent signals cannot be explained. The most likely cause is the deficiency of the solid Earth tide model in the IERS Conventions 2003. It implicates that GPS tidal measurements have a great potential to be used for testing solid Earth tide models, especially for the anelasticity of the Earth. The two lunar constituents, M_2 and O_1 , because for these waves the residual vectors have the largest signal-to-noise ratios, may be particularly useful for testing solid Earth tide models.

The results have suggested that GPS position time-series may be further improved if the GPS-estimated tidal displacement coefficients are used instead of the predictions from ocean tide models. The K_1 and K_2 estimates with poorer accuracy should be treated with caution. The effects of the GPS tidal displacement estimates on long-period signals in GPS daily position time-series are also investigated, which

will be discussed in Chapter 6.

Chapter 6 Effects of GPS tidal displacement estimates on long-period signals in position time-series

For over a decade, GPS position time-series with millimetre accuracy have been used for investigating geophysical phenomena at temporal scales from secular variations of the Earth's crust, such as reference frame establishment (e.g., Altamimi et al., 2007), tectonic plate movement (e.g., Larson et al., 1997; Prawirodirdjo and Bock, 2004) and glacial isostatic adjustment (e.g., Milne et al., 2001; Sella et al., 2007), to seasonal loading deformations of the Earth (e.g., Blewitt et al., 2001; Dong et al., 2002; Wu et al., 2003).

Recent studies have demonstrated that subdaily unmodelled or mismodelled periodic signals invariably result in spurious long-period signals in GPS position time-series at periods of geophysical interest, especially semiannual and annual signals (Penna and Stewart, 2003; Stewart et al., 2005; Penna et al., 2007). These spurious signals could be misinterpreted as genuine geophysical signals. Therefore, all subdaily periodic signals should be modelled as accurately as possible at the observation level in GPS data analysis. Otherwise, aliased long-period signals will inevitably arise in position time-series.

The subdaily periodic signals in GPS observations can be classified into two categories: 1) real periodic ground displacements, such as solid Earth tides, OTL and atmospheric tide loading, and 2) technique-dependent systematic effects, such as

inadequate satellite orbit modelling, antenna phase centre variations and multipath effects. At present, only solid Earth tide and OTL displacements are modelled according to the IERS Conventions 2003 in routine GPS data processing. The solid Earth tide models for site displacements generated by IERS Conventions 2003 are generally assumed to be at the 1 mm level. Penna et al. (2008) demonstrated that height errors of M_2 among different model predictions can reach up to about 3 mm at IGS sites and be as high as around 8 mm in some coastal areas, such as the Weddell Sea and Ross Ice Shelf. Tregoning and Watson (2009) found that 1~2 mm displacements resulting from S_1 and S_2 ATL can lead to spurious signals of up to 0.8 mm at GPS draconitic annual and semi-annual periods. By examining the subdaily coordinate spectral characteristics for ~90 global GPS sites, King et al. (2008) found that unmodelled signals with amplitudes of more than 10 mm may emerge in several principal tidal frequencies after the modelled solid Earth tide and OTL displacements are removed. The unmodelled signals propagate into the daily position time-series with annual and semiannual signals with amplitudes of up to 5 mm.

Both the regional and global analyses given in Chapters 4 and 5 have demonstrated that GPS can determine periodic ground displacements at principal semidiurnal and diurnal constituents (excluding K_1 and K_2) with accuracy superior to that of the model predictions, although sources of the large-scale systematic biases between observations and models cannot be quantified at present. The question arises as to whether applying GPS tidal displacement coefficients instead of model predictions

can improve position time-series. To this end, I investigate in this chapter the effects of GPS tidal displacements on long-period signals in position time-series at both 12 GPS sites in Hong Kong and 125 IGS reference sites. To better understand the effects of different tidal constituents, the position time-series are generated using various strategies to account for GPS tidal displacements.

6.1 Spurious long-period signals in GPS position time-series

GPS position time-series for most geophysical applications are conventionally produced by processing GPS observations in discrete 24-solar-hour sessions. According to standard undersampling theory (Shannon, 1998), unmodelled or mismodelled subdaily periodic signals will result in aliased long-period signals in daily position time-series. It has long been assumed that the effects of subdaily periodic signals are mostly averaged out in 24-hour session data processing (Lambert et al., 1998; Dragert et al., 2000; Dong et al., 2002). However, the simulation study of Penna and Stewart (2003) demonstrated that the unmodelled tidal signals for eight principal constituents result in aliased semi-annual and annual signals in position time-series with admittances (amplitude ratio of aliased signal to unmodelled tidal signal) of about 1-12%.

By analysing seven years of continuous GPS data from eight globally distributed sites where controlled errors were not modelled, Penna et al. (2007) showed that an unmodelled S_2 signal in the north component propagates into a semiannual signal in

the height component with admittance of greater than 100%, depending on the level of unmodelled displacement and the site location. The study of Tregoning and Watson (2009) found that failing to model semidiurnal and diurnal ATL at the observation level results in anomalous signals with amplitudes of up to 0.8 mm with periods closely to the GPS draconitic semiannual (~175.7 days) and annual (~351.4 days) periods. Therefore, the effects of unmodelled subdaily periodic signals on GPS position time-series cannot be mitigated by simple averaging through a processing session.

Stewart et al. (2005) developed a generalised analytical error model for the propagation of unmodelled systematic error at an unknown point into a position time-series estimated using least squares from range observations to a single reference point. When the reference point is stationary and the unknown point is undergoing unmodelled periodic motion, the resultant position time-series error can be simply considered the average of the unmodelled motion over the observation time period. However, when the reference point (satellite) occurring in GPS positioning is assumed to be in periodic motion, the resultant position time-series error function contains many periodic terms due to truncation errors in the linearisation of the functional model. The amplitude, phase and period of these periodic terms depend on the amplitude and period of the unmodelled periodic motion, the locations of the unknown point and reference point, the period of reference point's motion and the length of the observation time period. The output signals will

be further aliased into long-period variations accordingly if the observation window overlap is less than the Nyquist period of any of the signals.

When the typical continuous 24-solar-hour, non-overlapping GPS data processing and the unmodelled periodic signals of eight dominant semidiurnal and diurnal tidal constituents are considered, Table 6.1 lists five maximum aliased long-period signals calculated using Eqs (30) and (35) of Stewart et al. (2005). From Table 6.1, the largest aliased periods for all the constituents are due to repeat orbit effects, according to the statement of Penna and Stewart (2003). The aliased periods derived from the 24-hour processing effects for M_2 , N_2 , K_2 , K_1 , O_1 and Q_1 are the second largest, whilst those for S_2 and P_1 are the third largest.

Table 6.1 Five maximum aliased long periods for eight principal semidiurnal and diurnal tidal constituents calculated using Eqs. (30) and (35) of Stewart et al. (2005)^a

M_2	S_2	N_2	K_2	K_1	O_1	P_1	Q_1
<u>13.66</u>	<u>182.63</u>	<u>9.13</u>	∞	∞	<u>13.66</u>	<u>182.62</u>	<u>9.13</u>
<u>14.77</u>	365.26	<u>9.61</u>	<u>182.62</u>	<u>365.24</u>	<u>14.19</u>	121.75	<u>9.37</u>
14.19	∞	9.37	91.31	365.27	13.17	<u>365.24</u>	8.91
15.39	-	9.87	365.23	121.75	14.77	365.27	9.61
16.06	-	10.15	121.75	182.62	15.39	∞	9.87

^a Aliased periods resulting from 24-solar-hour processing and repeat orbit effects of Penna and Stewart (2003) are underlined and double underlined, respectively. Aliased periods (days) are listed by descending amplitude.

The aliased periods given in Table 6.1 provide a clue to mitigating spurious long-period signals in daily GPS position time-series. For example, an unexpected signal with a period of ~13.6 days in GPS position time-series has been detected previously (e.g., Lambert et al., 1998; Williams et al., 2004; Tregoning and Watson,

2009). This indicates that an aliased signal(s) may be likely caused by the unmodelled or mismodelled signals of the M_2 or O_1 constituents. The error in computing the frequency-dependent part of the solid Earth tide corrections in the Bernese software introduced complex spurious periodic signals in position time-series (Bernese Software Mail List 0190, available at ¹⁵< >). Watson et al. (2006) demonstrated that using the outdated IERS1992 solid Earth tide model instead of IERS2003 results in aliased semiannual and annual signals in height time-series with the amplitudes increasing as a function of latitude up to 2 mm and 0.4 mm, respectively. The aliased periods are consistent with theoretical prediction shown in Table 6.1.

Ray et al. (2008) examined stacked spectra of the weekly solutions for 167 IGS sites and found anomalous multiples of the harmonic that is coincident with GPS draconitic year (351.4 days). They suggested that mechanisms for the draconitic harmonics may involve orbit modelling errors or aliasing of site-dependent positioning biases modulated by the varying satellite geometry. Tregoning and Watson (2009) further suggested that unmodelled S_1 and S_2 atmospheric tide loading signals partly contribute to the spurious signals at draconitic frequencies observed by Ray et al. (2008), considering a realistic average aspect repeat time of GPS constellation. To reduce spurious signals in GPS position time-series, it is therefore

¹⁵ <ftp://ftp.unibe.ch/aiub/bswmail/bswmail.0190>

preferable to use the GPS-derived tidal displacement coefficients in which unmodelled subdaily periodic motions are taken into account, rather than applying the model predictions.

6.2 GPS data processing

To obtain an insight into the feasibility of the GPS-derived tidal displacements as substitutes for the model predictions, different GPS position time-series were generated after applying four tidal displacement corrections derived from:

- 1) the model predictions of all the eight principal and three long-period tidal constituents (M_f , M_m and S_{sa});
- 2) GPS estimates of the eight principal constituents plus the model predictions of three long-period constituents;
- 3) GPS estimates of the six principal constituents (excluding K_1 and K_2) plus the model predictions of the remaining five constituents;
- 4) GPS estimates of the seven principal constituents (excluding K_1) plus the model predictions of the remaining four constituents.

The standard PPP strategy in the GIPSY software was employed using the same options as in Chapter 3. Since it is found that integer ambiguity fixing has no significant influence on GPS position time-series in the regional analysis (see detail on Section 4.3), no attempt was made to fix ambiguities in both the regional and global data processing.

Four difference time-series, ts21, ts31, ts24 and ts43, were then obtained by differencing between the second and first position time-series, between the third and first position time-series, between the second and fourth position time-series, and between the fourth and third position time-series, respectively. Except for the effects of different tidal displacement corrections, the common geophysical signals and mode noises are removed after differencing of the position time-series. Series ts21 is the sum of ts31, ts24 and ts43. The results from the regional and global analyses will be discussed separately in Sections 6.3 and 6.4.

6.3 Results from the GPS network in Hong Kong

The GPS tidal displacement coefficients were obtained from the ambiguity-fixed estimates given in Appendix A without removing the systematic biases. The model predictions were derived from the NAO99b model. The difference time-series at HKFN are shown as an example in Figures 6.1-4, along with the corresponding amplitude spectra computed by the Lomb-Scargle periodogram method (Scargle, 1982) with an oversampling factor of four. The difference time-series for all the sites are given in Appendix C.1.

From Figures 6.1-6.4, the long-period signals in the difference time-series are significant after the different tidal corrections were applied. This coincides well with the results from analytical model prediction (Stewart et al., 2005), GPS data simulation (Penna and Stewart, 2003) and real GPS data experiment (Penna et al.,

2007). As shown in Figure 6.2, strong semiannual signals are detected in ts31 for all the three coordinate components. This is possibly caused by a large discrepancy of S_2 between the GPS and model estimates. In addition, the P_1 constituent also partially contributes to the semiannual signals. We have also detected the relatively weak signals of about fortnight period in ts31, which is mostly due to the propagation of M_2 and O_1 .

From the ts24 time-series in Figure 6.3, the K_1 constituent has a significant impact on the annual signals of position time-series. The annual signals in ts24 are more obvious after the antenna dome was used in December 2004, especially for the horizontal components. After OTL modelling was commenced in the JPL global solutions on 03/03/2002 (Watson, 2005), the vertical component of the ts43 time-series in Figure 6.4 shows a secular downward trend, while its east component has a secular eastward movement. The east and vertical velocities seem to be changed again after CMC modelling has been added in the JPL global products since 05/11/2006.

The offset, secular rate and annual and semiannual periodic terms of the difference time-series were estimated simultaneously using the least squares method. The estimated amplitudes of the annual and semiannual signals are shown in Figures 6.5 and 6.6, respectively. The estimated secular rates at each site are shown in Figure 6.7. It is seen from ts24 and ts21 in Figure 6.5 that the different tidal displacement corrections of K_1 have significant influences on the annual signal of position

time-series (magnitudes up to 0.3, 0.2 and 0.3 mm for the east, north and vertical components, respectively). The semiannual signals in ts21 and ts31 can reach up to 0.6 mm (east), 0.1 mm (north) and 0.7 mm (vertical) as shown in Figure 6.6, mostly due to the propagation of the S_2 constituent. From ts21 and ts43 in Figure 6.7, the secular rates reach 0.4 mm/yr and 1 mm/yr for the east and vertical components, respectively, after the different K_2 tidal displacement corrections are applied. This is probably caused by the fact that the period of K_2 is very close to the orbit period of the GPS satellites. The alias frequency between the GPS orbit and K_2 is thus close to infinity and resembles a secular trend.

It is seen from ts21 and ts31 in Figure 6.6 that the semiannual signals of the sites with observations collected since August 2004 are greater than those of the other sites for all the three components. Similar results can also be found in the east component of ts21 and ts24 in Figure 6.5 and all the three components of ts21 and ts43 in Figure 6.7. It is considered that this is mostly caused by the different observation time span at each site. When the offset, secular rate, and annual and semiannual periodic terms were re-estimated using the data with the same observation time span (from 01/08/2004 to 31/12/2007), the differences of the re-estimated parameters between sites are greatly reduced except for the vertical secular rate. The differences of the re-estimated annual and semiannual signals between sites are less than 0.1 mm. However, the differences of the vertical secular rates between sites still reach up to 0.3 mm/yr. This indicates that the GPS-derived

tidal displacement estimates of seven principal constituents (excluding K_2) have almost the same influences on GPS position time-series for all the sites. The propagated long-period signals in the position time-series are mostly due to the effects of systematic biases between the GPS and model values. The common-mode signal of K_2 at all sites can result in obvious region-wide velocity bias. Besides, the velocities can be significantly biased by site-dependent errors, such as multipath.

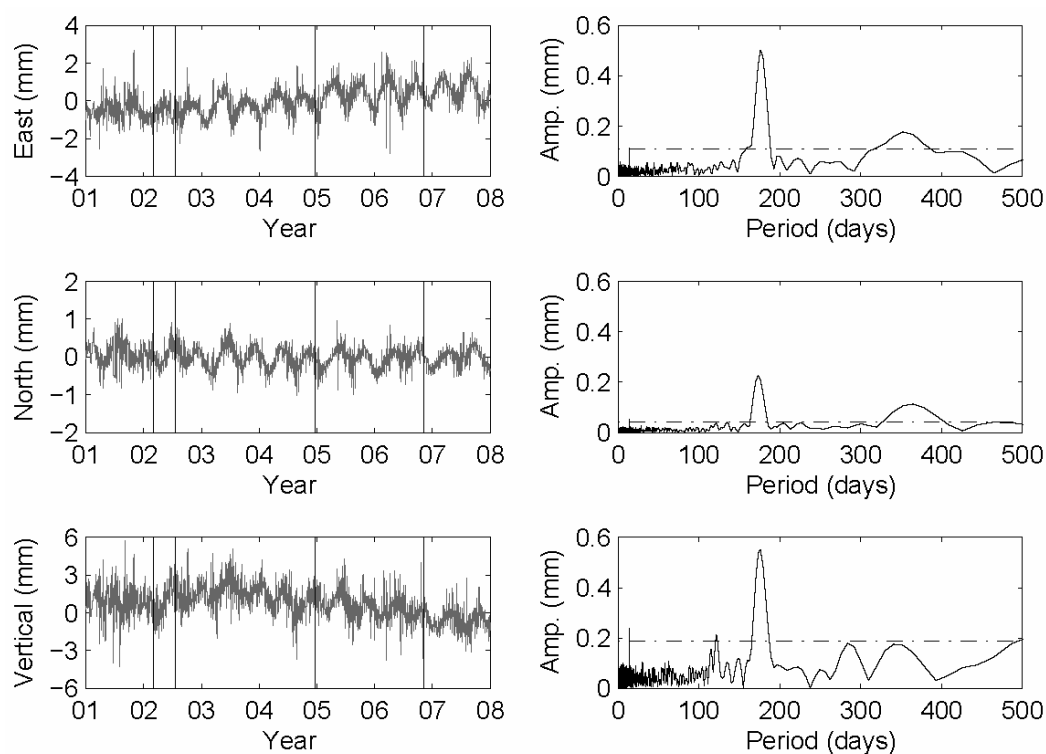


Figure 6.1 Effect of different tidal displacement corrections on position time-series (ts21) at HKFN. The left panel shows the difference time-series (ts21), and the right panel shows the corresponding amplitude spectra with 1% significance levels denoted by dash-dotted lines. Major data processing and environmental changes are indicated by vertical lines in the left panel: the JPL global solutions began modelling OTL using the FES99 model on 03/03/2002 and then upgraded to the FES02 model on 23/07/2002 (Watson, 2005); the antenna domes were added at all the Hong Kong sites in December 2004; and the JPL global solutions began modelling CMC on 05/11/2006.

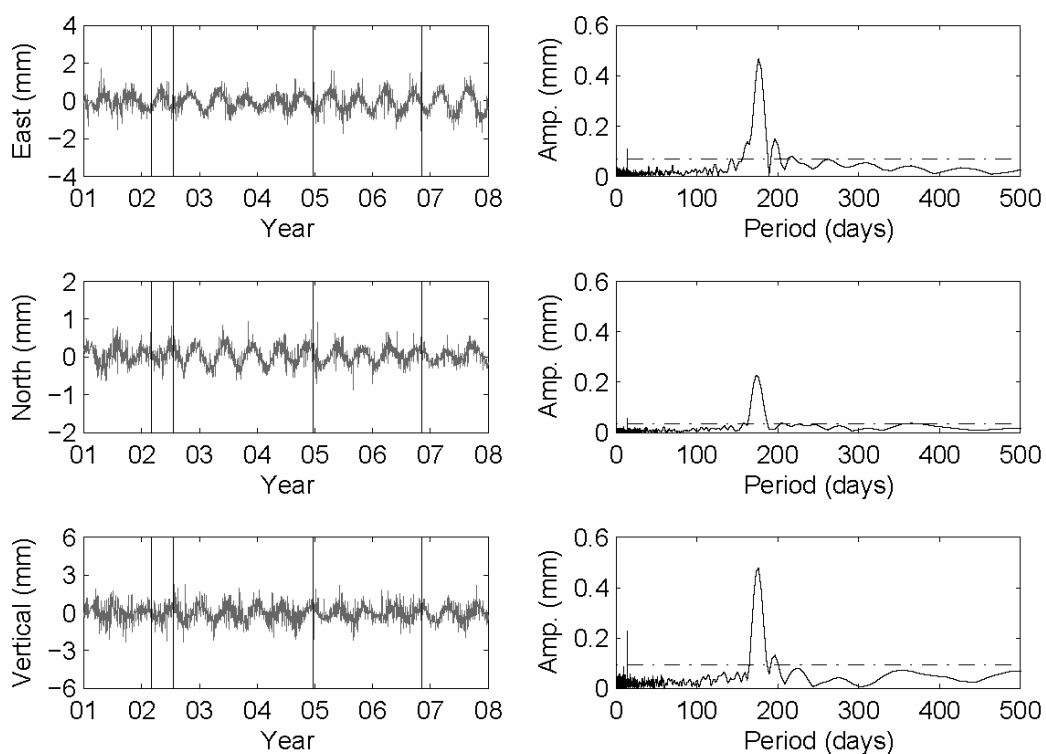


Figure 6.2 Effect of different tidal displacement corrections on position time-series (ts31) at HKFN. The left panel shows the difference time-series (ts31), and the right panel shows the corresponding amplitude spectra with 1% significance levels denoted by dash-dotted lines. The vertical lines in the left panel are the same as Figure 6.1.

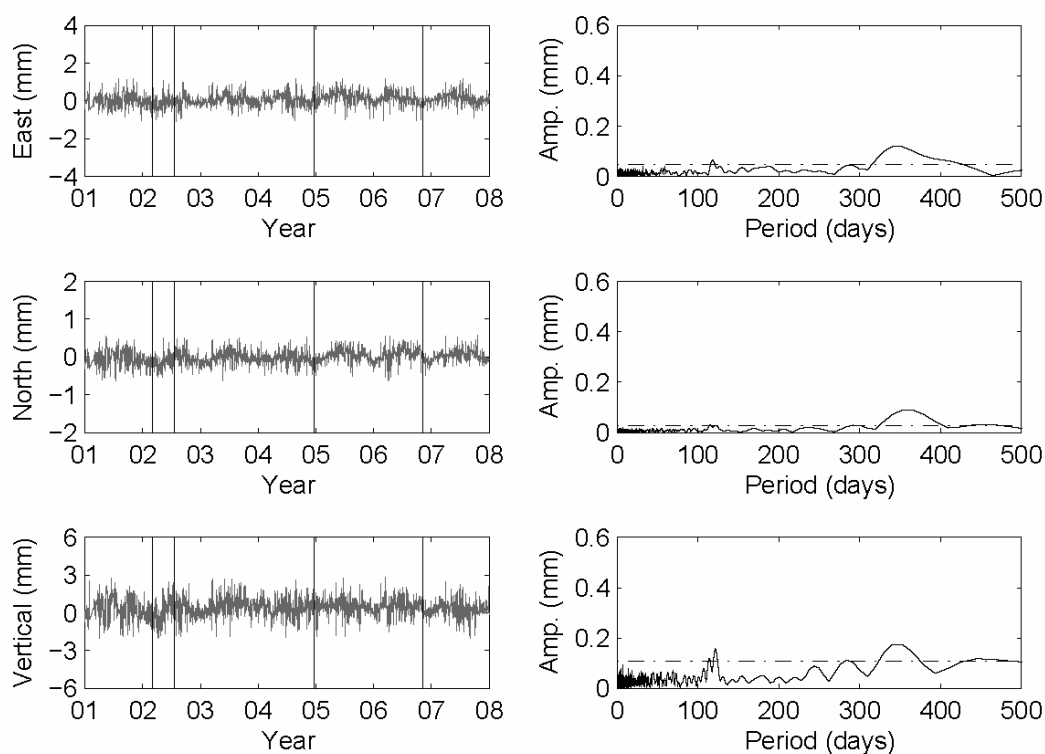


Figure 6.3 Effect of different tidal displacement corrections on position time-series (ts24) at HKFN. The left panel shows the difference time-series (ts24), and the right panel shows the corresponding amplitude spectra with 1% significance levels denoted by dash-dotted lines. The vertical lines in the left panel are the same as Figure 6.1.

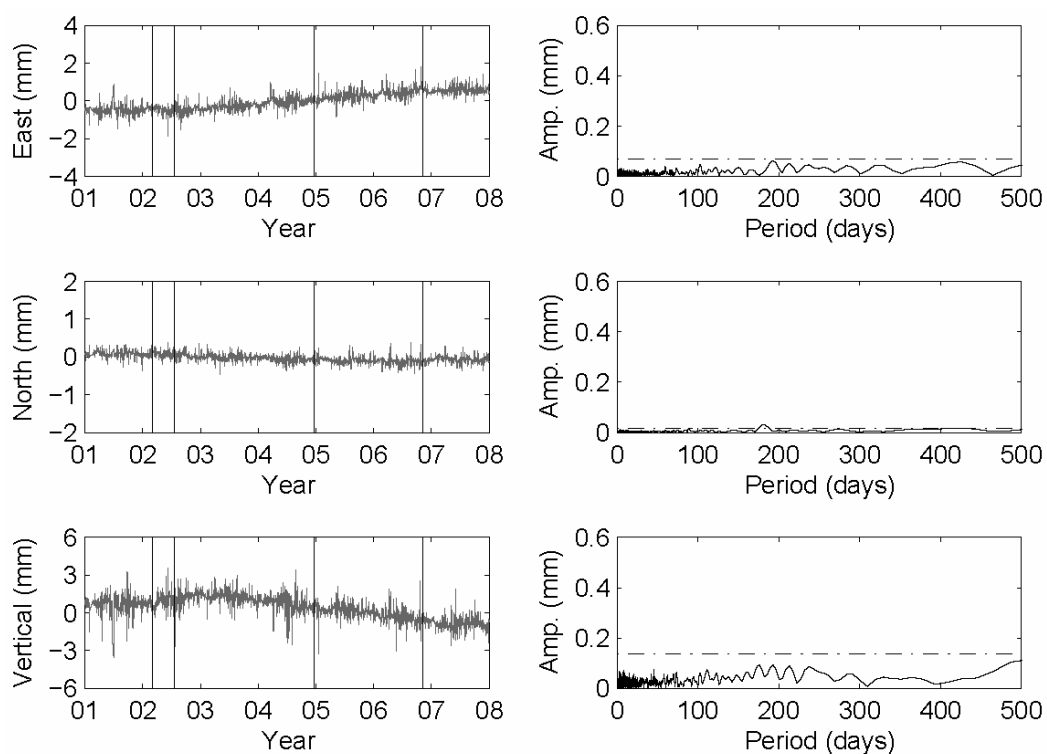


Figure 6.4 Effect of different tidal displacement corrections on position time-series (ts43) at HKFN. The left panel shows the difference time-series (ts43), and the right panel shows the corresponding amplitude spectra with 1% significance levels denoted by dash-dotted lines. The vertical lines in the left panel are the same as Figure 6.1.

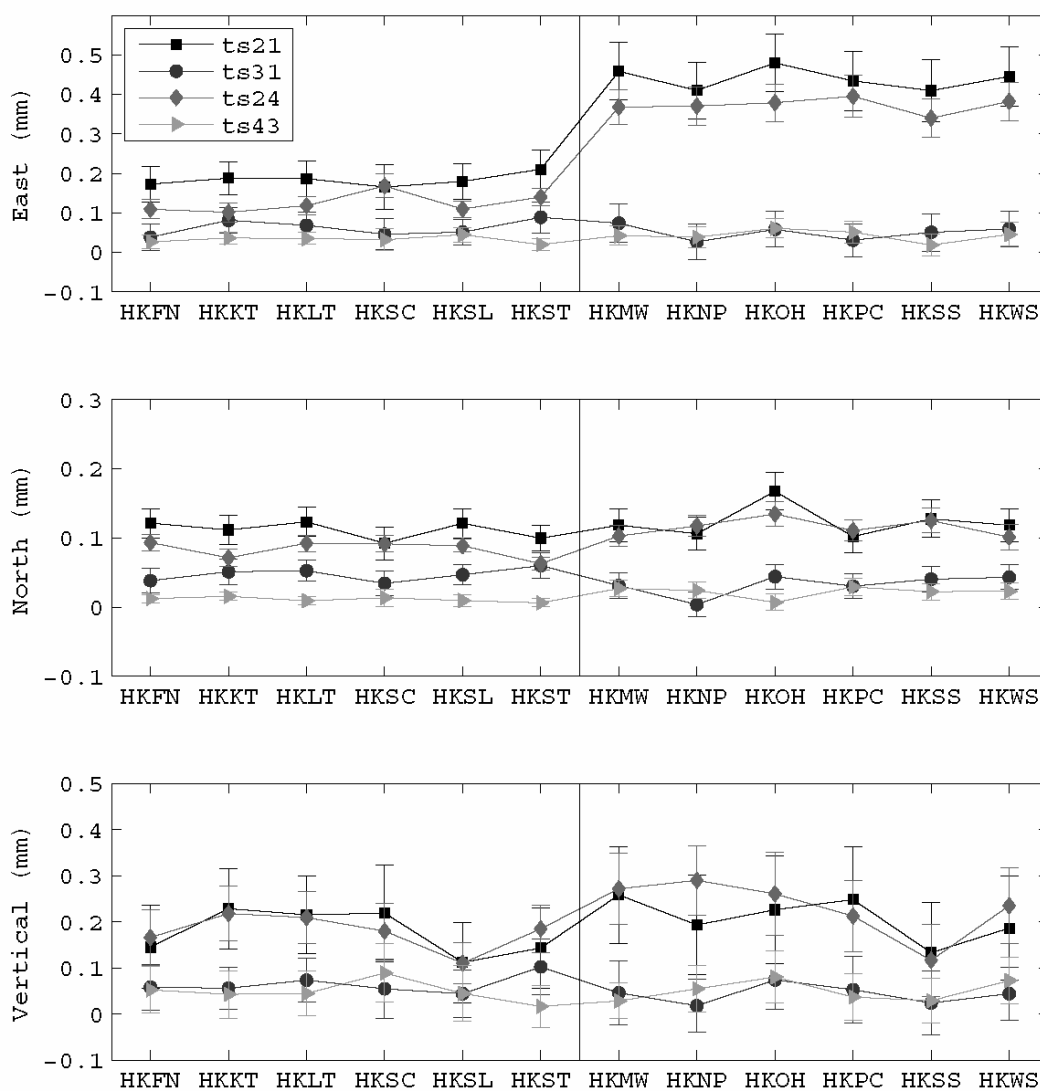


Figure 6.5 Annual amplitudes with 3-sigma error bars of position time-series due to the propagation of different tidal corrections. Six sites with observations collected since January 2001 (except for HKSC with observations collected since October 2002) are shown on the left side of the vertical line; and the remaining six sites with observations collected since August 2004 are shown on the right side of the vertical line.

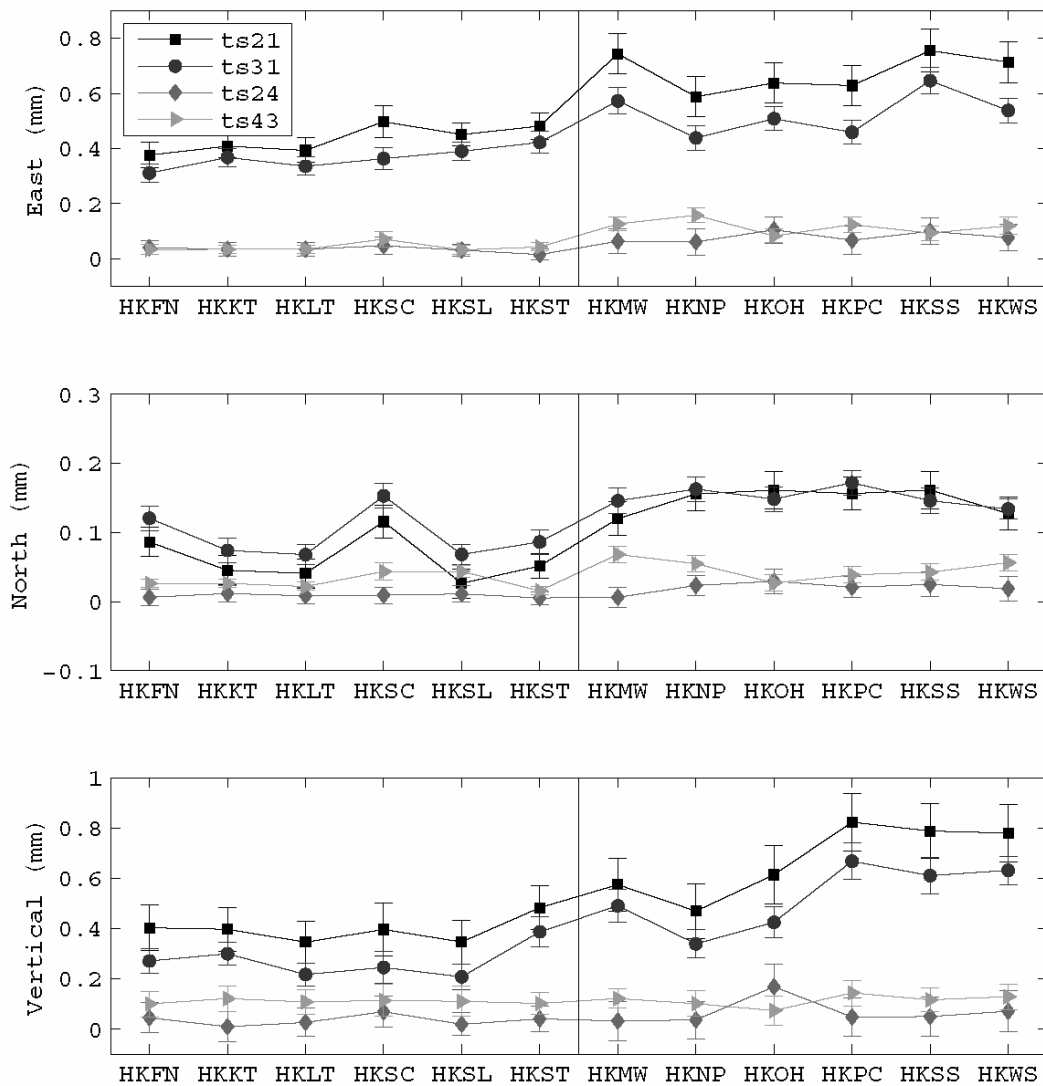


Figure 6.6 Semiannual amplitudes with 3-sigma error bars of position time-series due to the propagation of different tidal corrections. The vertical line is the same as Figure 6.5.

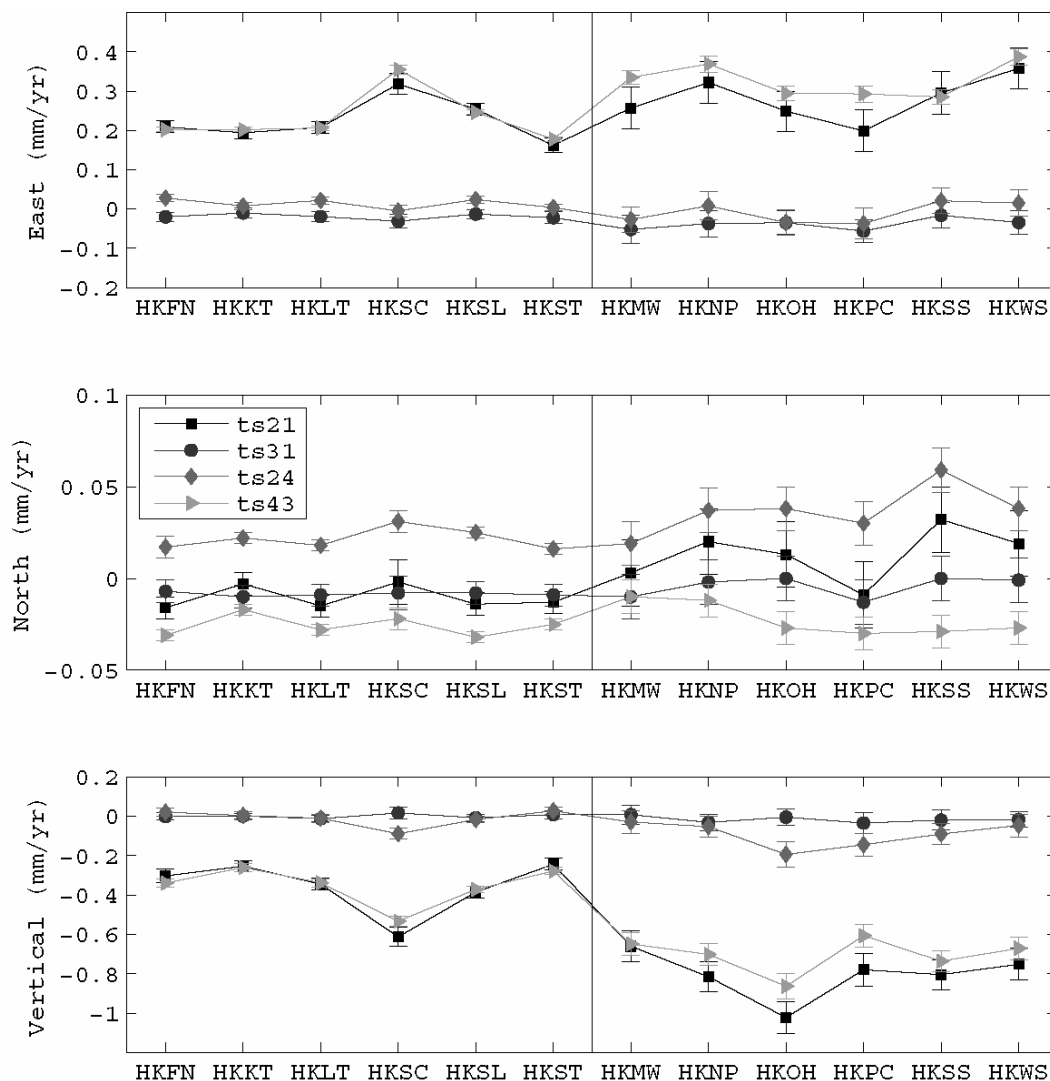


Figure 6.7 Secular rates with 3-sigma error bars of position time-series due to the propagation of different tidal corrections. The vertical line is the same as Figure 6.5.

6.4 Results from the global GPS network

The modelled OTL displacement coefficients are derived from the FES2004 model in the global analysis. The difference time-series (ts21, ts31, ts24 and ts43) at all the 125 global GPS sites are attached in Appendix C.2, along with the corresponding Lomb-Scargle amplitude spectra. In this section, I mainly focus on the semiannual,

annual and secular variations caused by different tidal displacement coefficients, and briefly discuss the characteristics of other spectral signals.

6.4.1 Constituents except K_1 and K_2

By inspecting the difference time-series ts_{31} and their corresponding amplitude spectra for all the global sites in Appendix C.2, it is clear that prominent spectral peaks at some or most of around 9 days, fortnightly, semiannual and annual periods are evident at most sites. The prominent periods found in these GPS difference time-series match theoretical aliased periods in Table 6.1. Annual and semiannual variations of the ts_{31} time-series at all the 125 sites are shown in Figure 6.8 and Figure 6.9, respectively.

The amplitudes of aliased annual signals reach up to ~ 0.32 mm (east), 0.15 mm (north) and 0.37 mm (height), and those of aliased semiannual signals reach up to ~ 0.34 mm (east), 0.23 mm (north) and 0.75 mm (height). Both the annual and semiannual signals exhibit spatial coherence. The latitude dependence of the semiannual signals is also evident. The sites located in high-latitude areas have negligible annual variations. The annual and semiannual signals mainly result from the propagation of differences between the GPS and modelled tidal displacement coefficients at the S_2 and P_1 frequencies. The beating effects between aliased periods of the M_2 , N_2 , O_1 and Q_1 constituents may also partially contribute to the annual and semiannual variations (Penna and Stewart, 2003). However, it is found no significant

secular variations (<0.05 mm/yr) in the ts31 time-series at all the sites, which possibly caused by the GPS/model tidal misfits of S_2 and P_1 according to the predictions in Table 6.1.

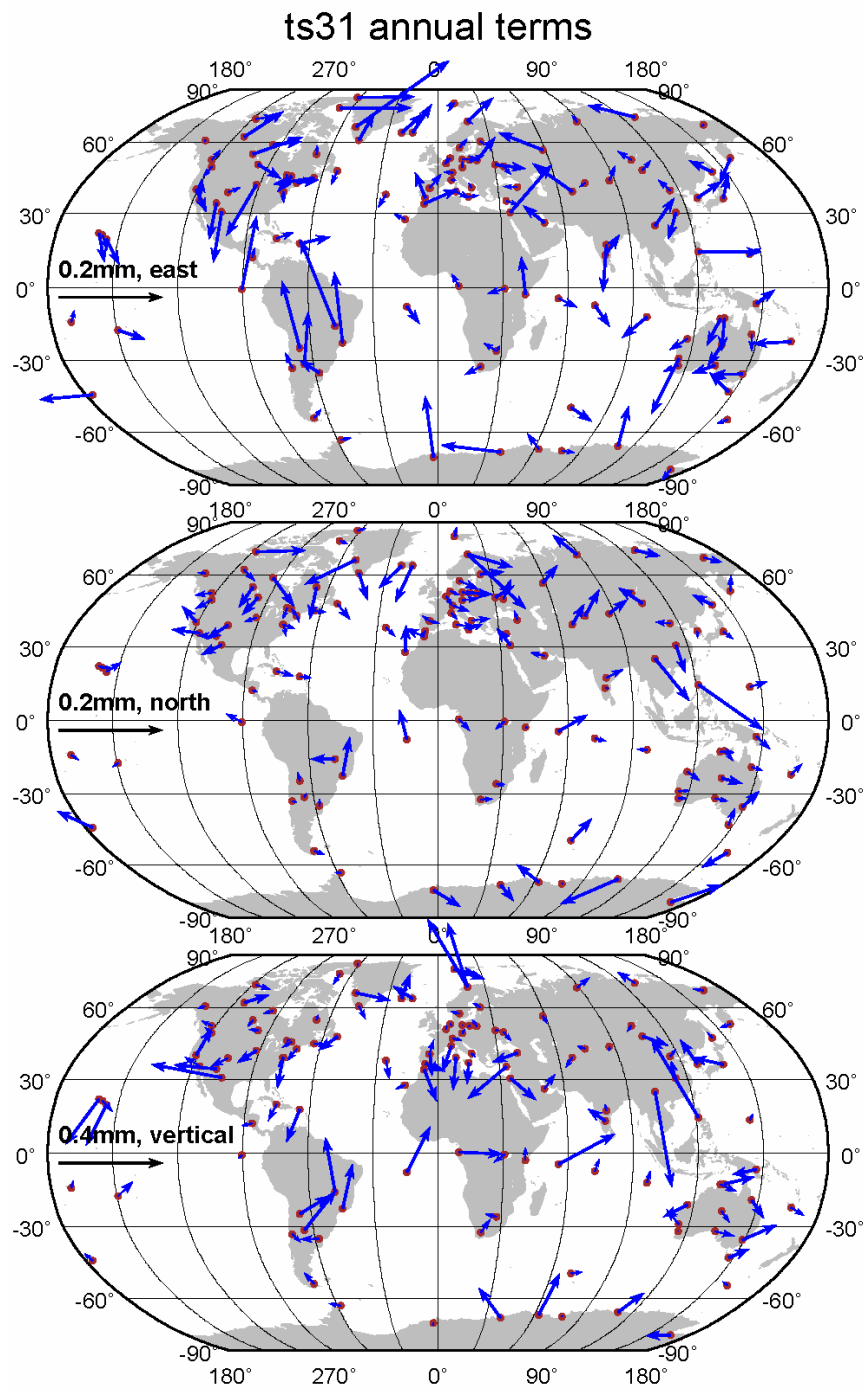


Figure 6.8 Annual variations due to the propagation of GPS/model tidal displacement corrections for all the principal constituents except K_1 and K_2 . The arrows represent the amplitudes. The phases increase clockwise from the upward direction.

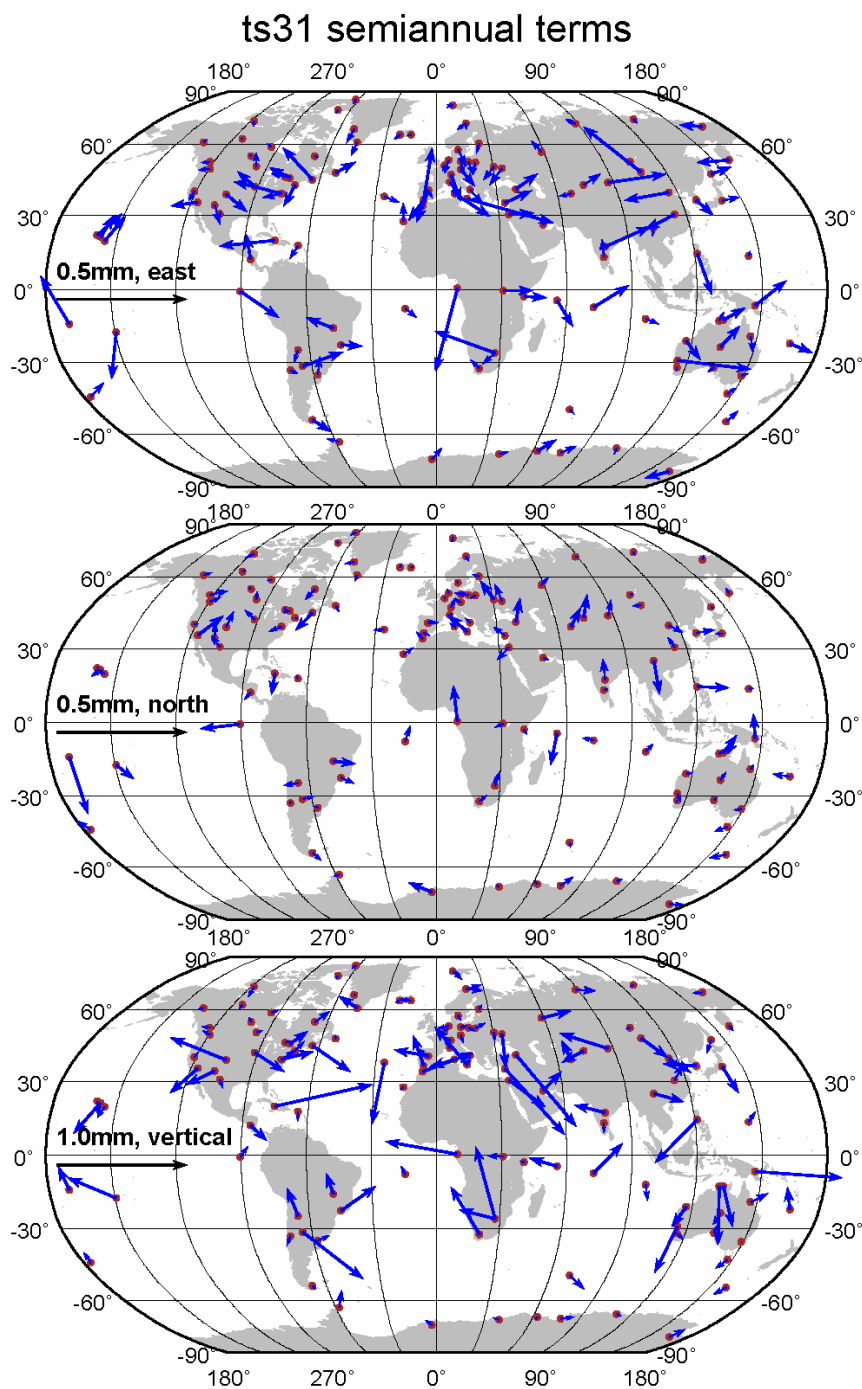


Figure 6.9 Semiannual variations due to the propagation of GPS/model tidal displacement corrections for all the principal constituents except K_1 and K_2 . The arrows represent the amplitudes. The phases increase clockwise from the upward direction.

6.4.2 K_1 constituent

I now investigate the impact of GPS/model tidal displacement coefficients for the K_1 constituent on the GPS position time-series. It can be seen from the amplitude spectra of the ts24 time-series at all the sites in Appendix C.2 that the GPS/model tidal displacement differences of K_1 result in prominent spectral peaks in the annual, semiannual and ~ 122 day periods, which is consistent with the theoretical predictions (Table 6.1). The predicted largest secular variations of K_1 is much less pronounced but still can be detected in the GPS position time-series. The estimated annual, semiannual and secular variations are shown in Figures 6.10-6.12, respectively.

From Figure 6.10, anomalous large annual signals appear in the east component of TRAB (0.65 mm), and in the vertical component of SEY1 (2.06 mm) and KUNM (1.62 mm). When the abnormal signals are excluded, the annual signals are less than 0.38 mm (east), 0.27 mm (north) and 0.67 mm (vertical). The aliased semiannual signals are relatively smaller with magnitudes less than 0.11 mm (east), 0.05 mm (north) and 0.19 mm (vertical) when the vertical abnormal signal at SEY1 with magnitude of 0.56 mm is excluded. The resultant secular rates reach up to 0.16 mm/yr and 0.30 mm/yr for the east and vertical components, respectively. The north secular variations can be neglected due to their quite small magnitudes (i.e., less than 0.04 mm/yr). All the aliased annual, semiannual and secular signals of K_1 show some spatial coherence.

Instrumental updates at some of the sites have significant influences on the propagation of K_1 signals. Taking PIE1 and KUNM as examples (see Figure 6.13), it is seen that three receiver updates at PIE1 and one receiver updates at KUNM result in obvious changes of the signal structures in the difference time-series. The influence on KUNM is stronger than PIE1. By inspecting the convergence plots of the two sites (see Appendix B.1), it is found that the GPS estimates of K_1 tidal displacements can be well resolved at PIE1 while the vertical estimates of K_1 tidal displacements at KUNM cannot converge in the combinations. It is considered that the interaction of different instruments (i.e., receiver and antenna) and the site's surrounding environment results in site-dependent errors, such as multipath effects. It thus leads to two-fold effects related to environmental changes: the effects of K_1 tidal displacement estimates and their corresponding aliased effects.

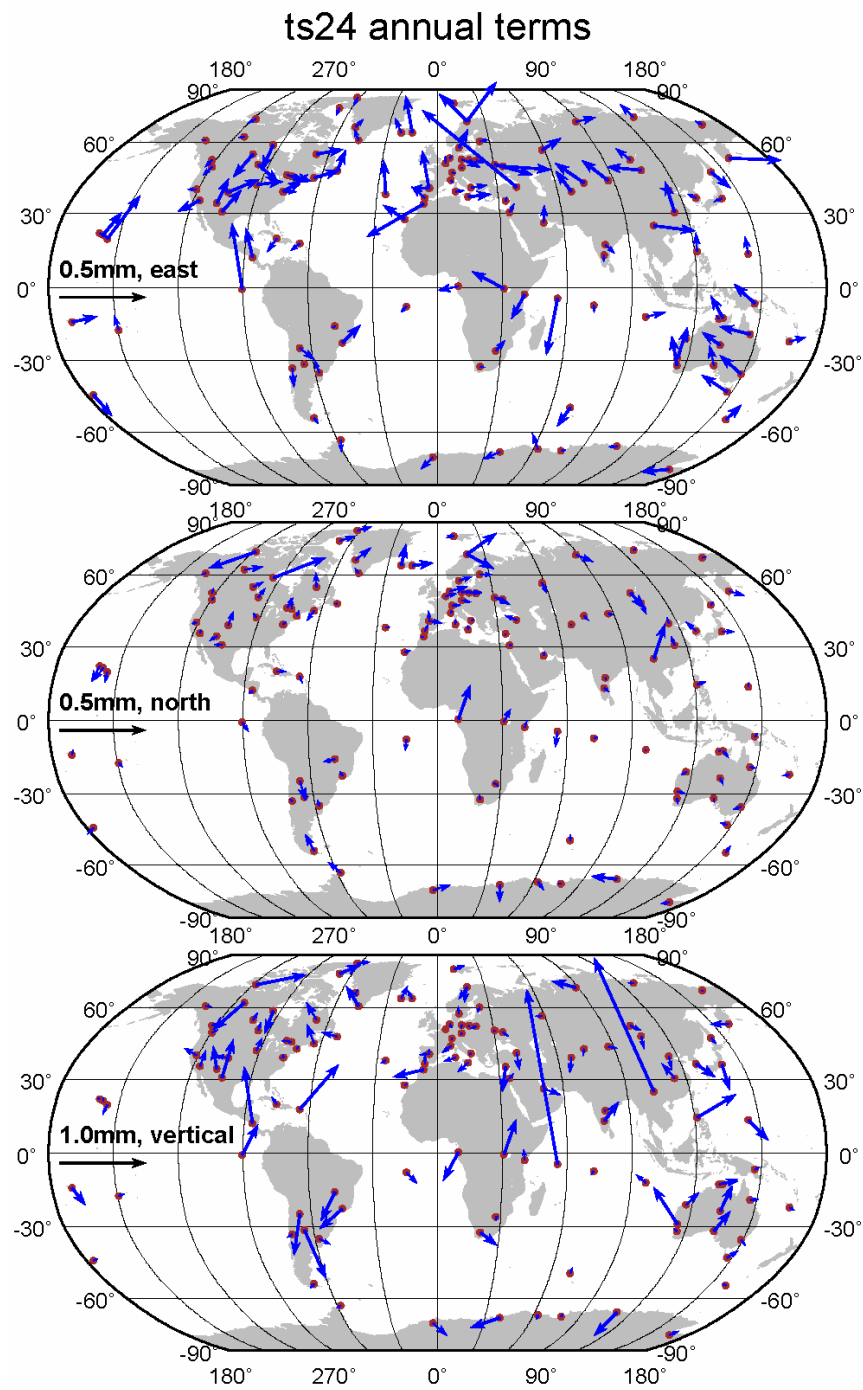


Figure 6.10 Annual variations due to the propagation of GPS/model tidal displacement corrections for the K_1 constituent. The arrows represent the amplitudes. The phases increase clockwise from the upward direction.

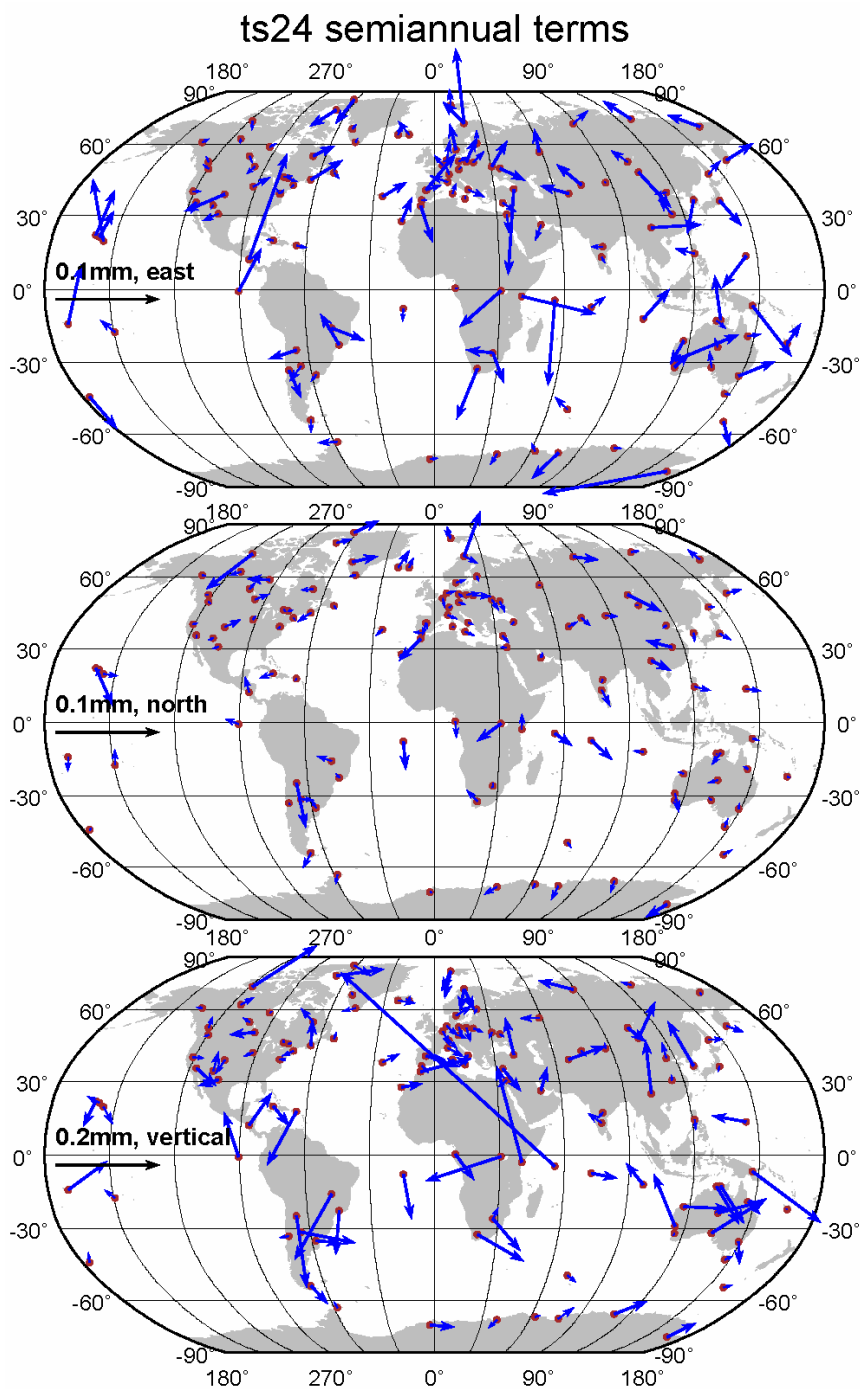


Figure 6.11 Semiannual variations due to the propagation of GPS/model tidal displacement corrections for the K_1 constituent. The arrows represent the amplitudes. The phases increase clockwise from the upward direction.

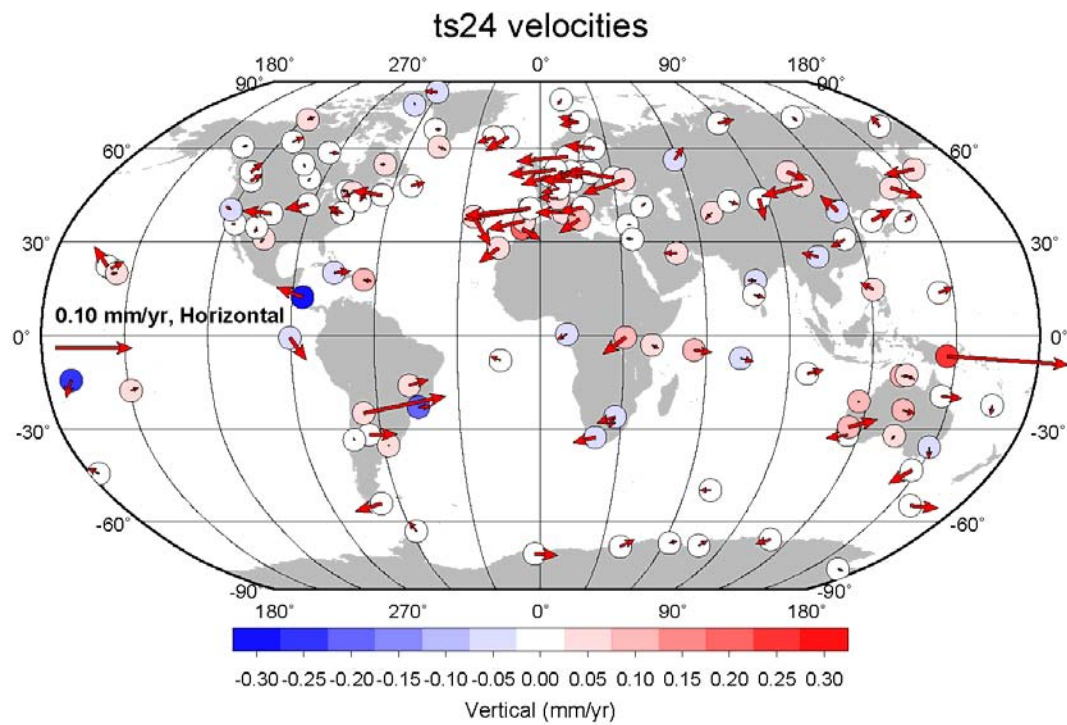


Figure 6.12 Velocity differences due to the propagation of GPS/model tidal displacement corrections for the K_1 constituent.

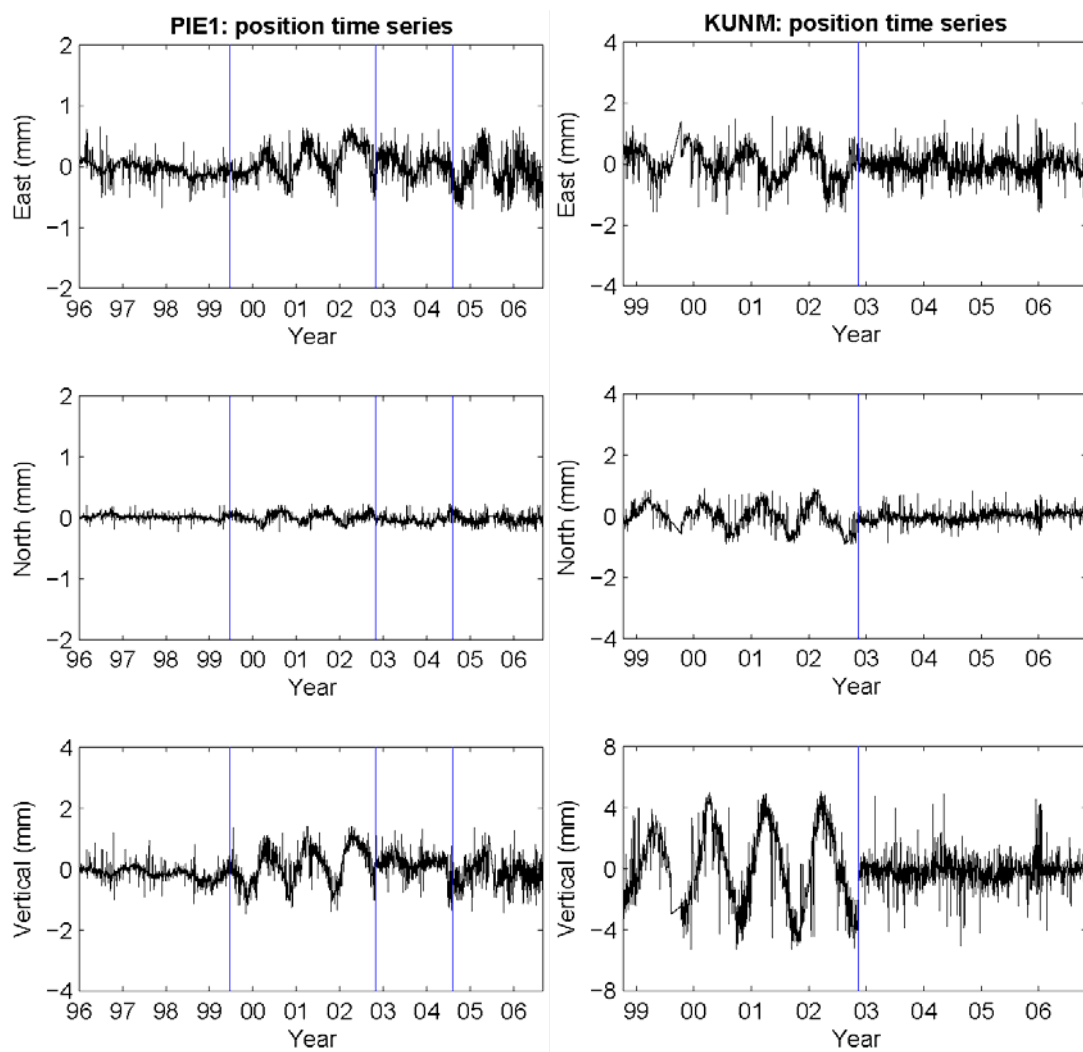


Figure 6.13 Difference time-series (ts24) at sites PIE1 and KUNM. Major receiver upgrades are indicated by vertical blue lines.

6.4.3 K_2 constituent

It can be seen from the ts43 time-series at all the sites in Appendix C.2 that the secular variations of ts43 are correlated with changes in the GPS constellation. The temporal variations are dependent on the K_2 GPS/model differenced signals and also different from site to site. Figure 6.14 shows position variations due to the K_2

GPS/model differenced signals at sites KUNM and RABT. During the time period from 1996 to 2006, 10 Block II/IIA satellites were decommissioned and 14 Block IIR were launched. The vertical secular variations are up to 1.11 mm/yr at RABT. If the time periods of 1998-2002 and 2002-2006 are considered separately, the velocity biases also reach about 1 mm/yr at KUNM. It is considered that the aliased frequency between the K_2 period and the time-variable satellite geometry resembles temporal secular variations, and the biased satellite antenna offsets used in the global analysis cannot be ruled out (Ge et al., 2005).

A global view on the velocity biases resulting from the GPS/model differenced signals of K_2 is demonstrated in Figure 6.15. The estimated velocities can reach 0.12, 0.35 and 1.11 mm/yr in east, north and vertical components, respectively. The velocities for sites located at high latitudes are relatively small, although the K_2 GPS/model differenced signals are large at some of the sites. The aliased annual and semiannual variations are relatively small but cannot be neglected (see Figures 6.16-6.17). For the aliased annual signals, the magnitudes reach about 0.15 mm (east), 0.05 mm (north) and 0.30 mm (vertical), and 0.35 mm (east), 0.13 mm (north) and 0.59 mm (vertical) for the semiannual signals.

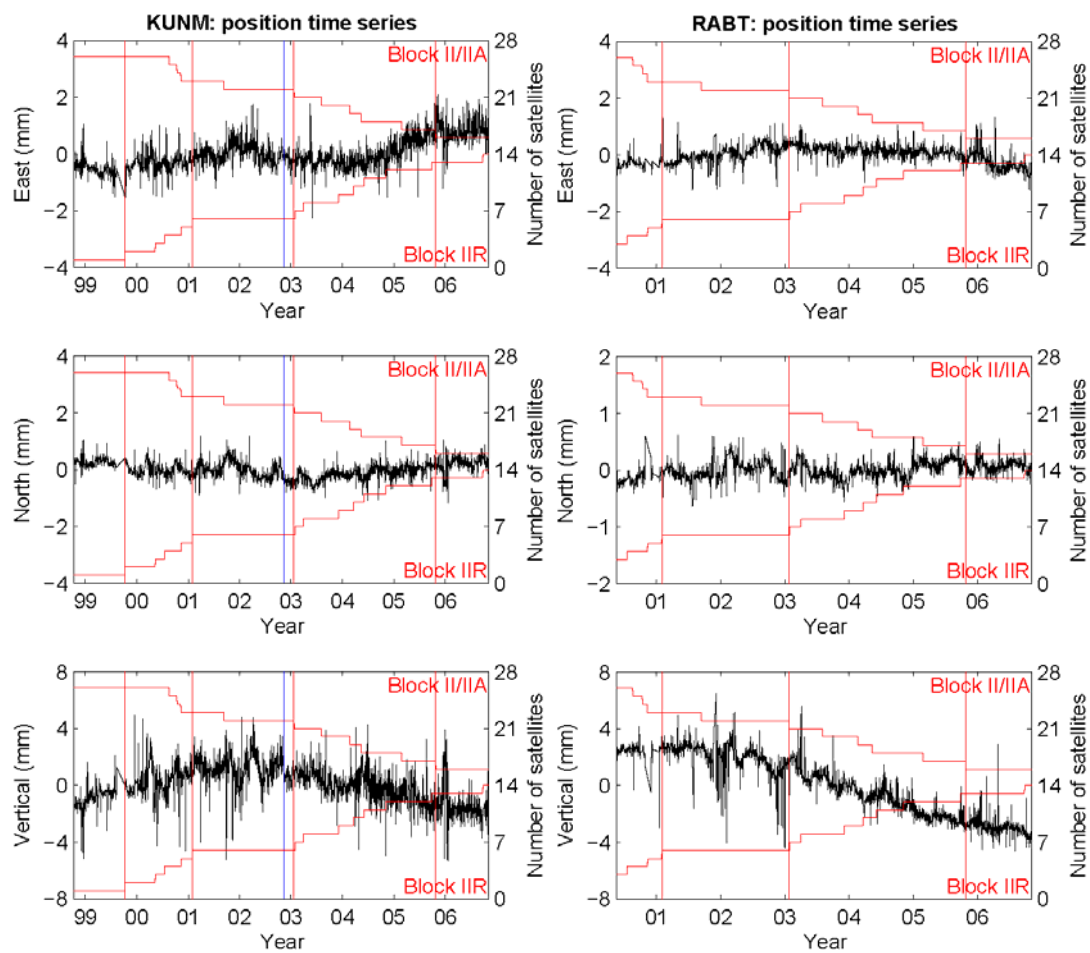


Figure 6.14 Difference time-series (ts43) at KUNM (left panel) and RABT (right panel). Major receiver changes are indicated by vertical blue lines, and variations in the GPS constellation are shown in red lines.

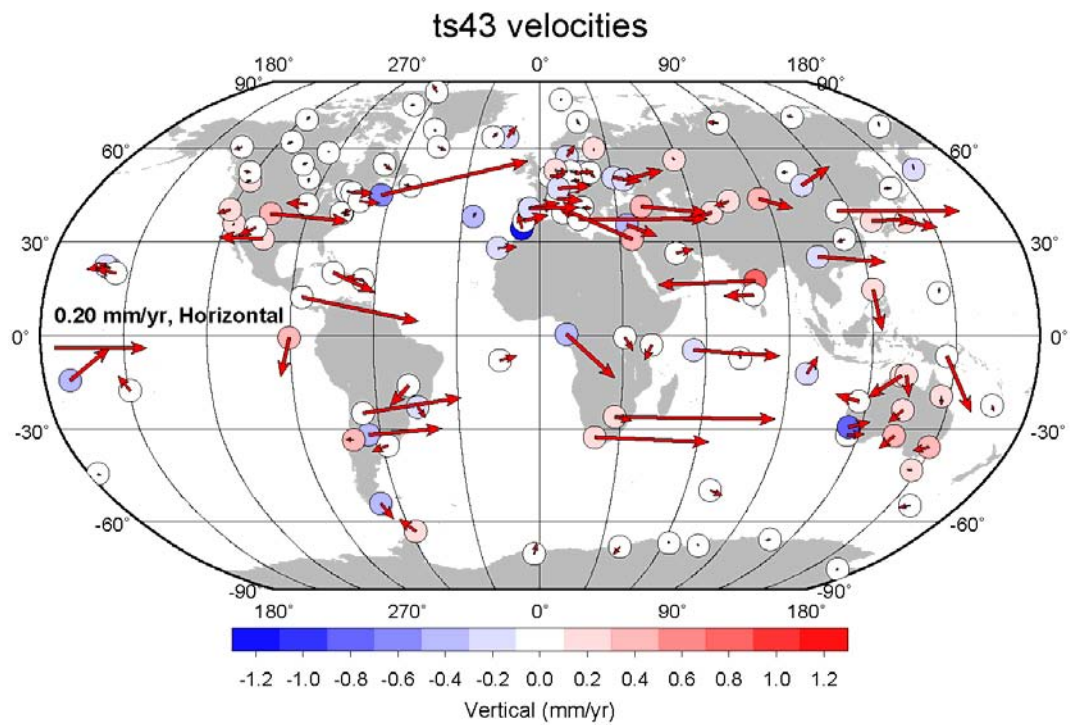


Figure 6.15 Velocity differences due to the propagation of GPS/model tidal displacement corrections for the K_2 constituent.

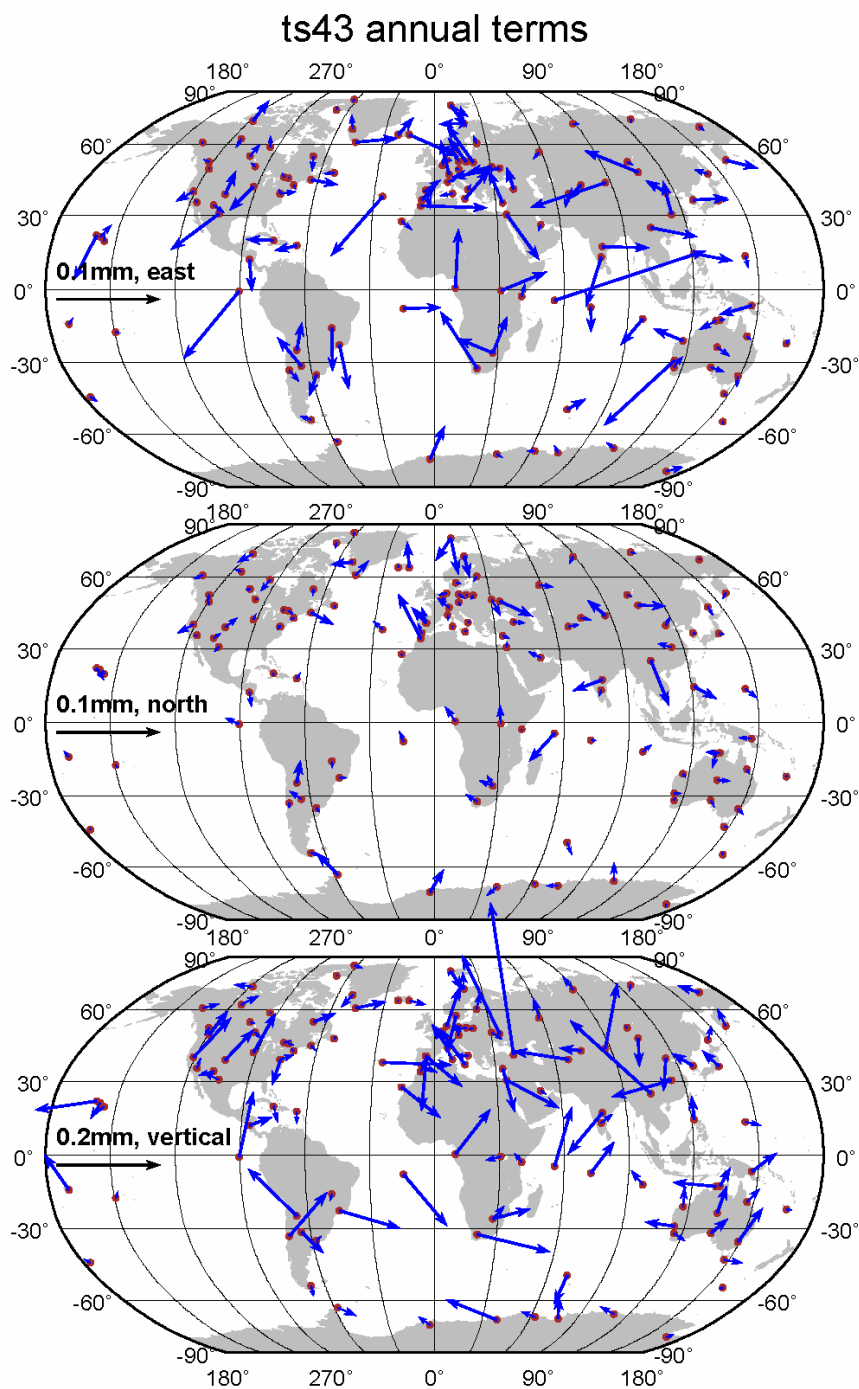


Figure 6.16 Annual variations due to the propagation of GPS/model tidal displacement corrections for the K_2 constituent. The arrows represent the amplitudes. The phases increase clockwise from the upward direction.

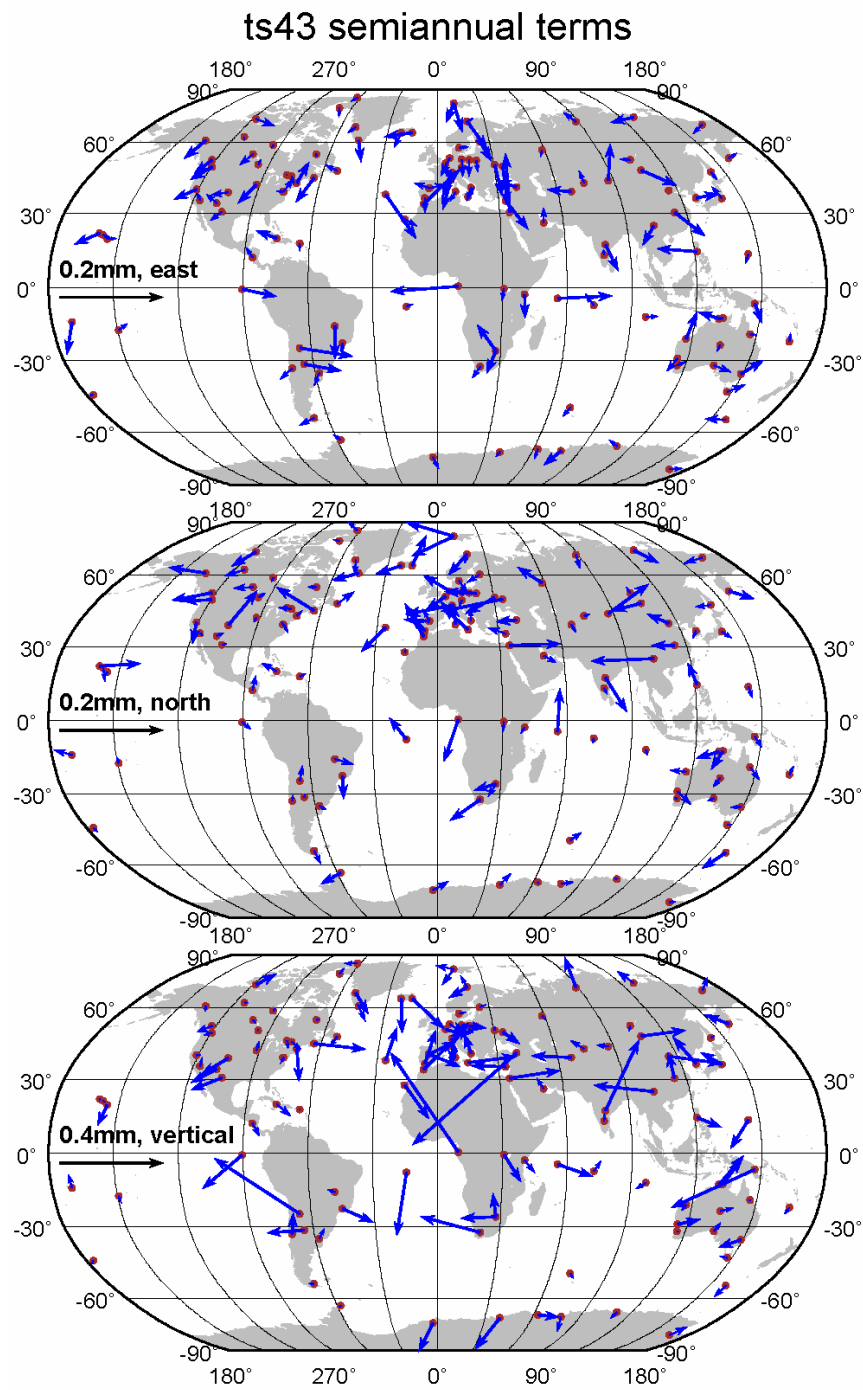


Figure 6.17 Semiannual variations due to the propagation of GPS/model tidal displacement corrections for the K_2 constituent. The arrows represent the amplitudes. The phases increase clockwise from the upward direction.

6.5 Summary

The effects of GPS tidal displacement coefficients instead of modelled predictions on long-period signals in position time-series at 12 GPS sites in Hong Kong and 125 IGS reference sites have been demonstrated. The propagated signals have prominent spectral peaks at periods consistent with theoretical predictions (Stewart et al., 2005). The amplitudes of the aliased signals have been found to be dependent on both the amplitudes of GPS/model tidal residuals and the site locations. These spurious long-period signals in GPS position time-series are large enough to bias estimates of real geophysical signals.

For the principal semidiurnal and diurnal constituents except K_1 and K_2 , the magnitudes of the aliased annual and semiannual signals can reach 0.8 mm in the height time-series. Both the annual and semiannual signals show strong spatial coherence. There is no impact on the site velocity. For the K_1 and K_2 constituents, the propagated signals exhibit not only significant annual and semi-annual variations, but also large secular trends. The difference between the GPS and model estimates of K_2 tidal displacements causes velocity biases of more than 1 mm/yr at some sites. The propagated signals are apparently related to temporal changes of the constellation geometry. Some equipment (i.e., receiver and antenna) changes can alter the propagation behaviour of the K_1 signal.

The empirical subdaily GPS-derived tidal displacement coefficients with

sub-millimetre accuracy (with exception of the K_1 and K_2 constituents) have proved to reduce the spurious signals in position time-series and are recommended to be used in routine GPS data processing for high-precision positioning applications, especially for surface deformation studies on seasonal time scales. The GPS tidal displacements for K_1 and K_2 with inferior accuracy should be used with caution. Improved modelling of GPS-related errors close to K_1 and K_2 frequencies would improve position time-series, whose mechanism requires further investigation.

Chapter 7 Conclusions and recommendations

7.1 Conclusions

Both of the regional and global analyses have demonstrated that the GPS technique is capable of estimating tidal displacements for all the principal semidiurnal and diurnal constituents except K_1 and K_2 with sub-millimetre precision. The GPS tidal displacements of six principal constituents can substitute for the model predictions in GPS data analysis for high-precision geodetic applications. This research opens a door for global continuous GPS network to be used to investigate solid Earth tides and OTL with a spatial coverage not achievable from SG and VLBI observations. Major conclusions drawn from this thesis work are summarised as follows.

The static method of determining the tidal displacements using continuous GPS observations has been developed. Residual three-dimensional tidal displacements at the semidiurnal and diurnal frequencies, after removing the modelled solid Earth tides, were directly estimated from continuous GPS observations via a modified PPP processing strategy on a daily basis. Daily tidal displacement estimates and their variance-covariance matrices were then combined individually at each site using a standard Kalman filter to obtain the final estimates. The two-step processing strategy can not only minimise processing time and maximise efficiency, but also preserve the long observational arcs that are required for the most accurate tidal displacement estimation.

It has been shown that the tidal displacements of all the subdaily constituents, except

K_1 and K_2 , can be resolved fairly well using more than 1,000 daily solutions. The estimates of the four solar-related constituents, S_2 , K_2 , K_1 and P_1 , exhibit seasonal fluctuations probably due to temperature-dependent factors. The K_1 and K_2 estimates cannot stabilise at some of the sites even if more than 3,000 daily solutions are used. The equipment (receiver and antenna) changes and the time-varying GPS constellation geometry have been found to have substantial influences on the estimates of K_1 and K_2 , respectively.

Three to seven years of GPS observations from a dense continuous reference site network in Hong Kong have been analysed to determine the subdaily 3D tidal displacements. By comparing the GPS results with the predictions from seven latest global ocean tide models and the gravity results, it has been found that GOT4.7 and NAO99b are the most suitable models for the OTL corrections in Hong Kong at present. The GPS estimates of M_2 , N_2 , O_1 , P_1 and Q_1 are consistent with the NAO99b model predictions at the sub-millimetre level in all the three components. However, three constituents S_2 , K_1 and K_2 show larger discrepancies between the GPS estimates and model predictions. The residuals between the GPS and model values exhibit strong spatial coherence. After the mean GPS/model biases are removed, the observed misfits between the sites for the six principal constituents, except for K_1 and K_2 , are all less than 0.5 mm and 1.0 mm in the horizontal and vertical components, respectively. The observed misfits at the K_1 and K_2 frequencies are relatively large (within 2.5 mm in all the three components). Integer ambiguity fixing improves the agreement between the east tidal displacement estimates and the model

predictions, especially for the K_2 constituent. Comparison between the GPS and gravity results suggests that the GPS estimates of K_1 and K_2 are mainly affected by GPS-related errors. The S_2 estimates from both GPS and gravity observations show large differences from the model values.

The semidiurnal and diurnal tidal displacements at 125 IGS05 reference sites were also derived by analysing GPS observations from 1996 to 2006. Comparing the GPS and VLBI estimates of tidal displacements with the predictions from the seven latest ocean tide models, GPS is capable of determining the tidal displacements with accuracy superior to VLBI for eight principal constituents except K_2 . The WRMS misfits indicate that GPS can determine tidal displacements with sub-millimetre precision in all the three components for all the constituents except K_1 and K_2 . The AG06a model gives anomalous results compared with both the GPS and VLBI estimates, indicating that this model is inappropriate for modelling OTL corrections in geodetic data processing. The four models (FES2004, TPXO7.1, GOT4.7 and EOT08a) fit the GPS estimates equally well at global scale. There are apparent large-scale spatial pattern for all the constituents except K_2 in the GPS/model residuals. The estimates of the M_2 and O_1 constituents showing the largest signal-to-noise ratios are particularly suitable for testing solid Earth tide models.

It has been demonstrated that the GPS tidal displacement coefficients of all the principal diurnal and semidiurnal constituents (excluding K_1 and K_2) with the sub-millimetre precision can provide an alternative to the model predictions at IGS

or other GPS sites for surface deformation studies on seasonal time-scales. The K_1 and K_2 coefficients should be treated with caution due to their relatively poor accuracy. Changes in the GPS constellation can propagate K_2 GPS/model differenced signals differently over time, resulting in temporal secular variations of more than 1 mm/yr in position time-series.

7.2 Recommendations for future work

This research has revealed promising results for future research on Earth tides. Further progress towards improving the accuracy and reliability of GPS tidal displacement estimates can be expected. The tidal estimates may be substantially improved by homogeneously reprocessed global GPS orbit and clock products to be provided by IGS. Some unresolved issues in this thesis, such as the effects of satellite-specific phase center variations, the centre-of-mass variations due to ocean tides and the higher-order ionospheric terms, should be addressed. Future studies will also benefit from GPS observations with longer observational time period which can further reduce random errors and allow better separation of the tidal constituents.

The estimation technique needs to be further developed before it can be implemented in routine practice. Removing a priori modelled OTL displacement coefficients from observations and constituent-specific constraints on the tidal parameters in daily GPS data processing are expected to improve further the convergence of the tidal parameters in the latter combination. Constituent-dependent scaling of daily variance-covariance matrices in the combination processing would help better

separate the constituents and prevent the contamination of errors that originate from other constituents. New time-efficient ambiguity resolution methods, such as Ambizap (Blewitt, 2008), could be applied to assess the influence on tidal displacement estimates in a global network.

Tidal displacement estimates of K_1 and K_2 suffer from orbit mismodelling and aliasing of errors, due largely to that the repeat period of the GPS constellation and the orbital period of the GPS satellites are closely to the periods of K_1 and K_2 , respectively. The revitalised GLONASS, and the upcoming Compass and Galileo in different orbital configurations will allow for the identification and removal of the systematic errors at the two tidal frequencies. Also, they will provide more observations to further reduce random errors. As a result, GNSS measurements of tidal displacements should be expected to yield submillimetre accuracies for all the eight semidiurnal and diurnal constituents in the next decade.

Unless subdaily periodic systematic errors are modelled perfectly, they will invariably propagate into long-periods of geophysical interest in GPS position time-series. It is highly recommended that the GPS tidal displacement coefficients of the principal diurnal and semidiurnal constituents excluding K_1 and K_2 with the sub-millimetre accuracy be applied to future global GPS data analysis. The unmodelled or mismodelled signals of K_1 and K_2 results in not only significant annual and semi-annual variations, but also large secular trends of up to 1 mm/yr. Understanding the mechanism of GPS-related errors with frequencies close to K_1 and

K_2 would also aid improving position time-series.

A databank of GPS tidal displacement coefficients for globally distributed sites, at least for the IGS sites, needs to be established with the participation of the whole geodetic community in the future. It will not only provide empirical GPS tidal displacement coefficients to satisfy the demand of high-precision positioning, but also promote studies on Earth tides. By comparison with the theoretical model, the GPS tidal datasets will provide important constraints to the structure of the Earth's interior. Even constraints on the anelasticity and heterogeneity of the solid Earth at tidal frequencies could be derived.

Appendix A Auxiliary materials for Chapter 4

Auxiliary materials discussed in Chapter 4 are included in \attachment\chapter4 directory on the attached CD-ROM. They are also available through my homepage (<http://sites.google.com/site/linguosite/>). The auxiliary materials are provided in Portable Document Format (PDF) files.

A.1 Summary about GPS and gravity sites in Hong Kong

A brief summary about 12 GPS sites and one gravity site in Hong Kong are contained in \attachment\chapter4\A.1.pdf.

A.2 Convergence plots for GPS sites in Hong Kong

Convergence plots for 12 GPS sites in Hong Kong are contained in the \attachment\chapter4\A.2 directory. The plot for each site shows the amplitudes of residual vectors after the addition of each daily solution, relative to the final estimates for east (top), north (middle) and vertical (bottom). Both ambiguity-free and ambiguity-fixed results are given.

A.3 Tidal parameter correlations of GPS sites in Hong Kong

Parameter correlation plots of the tidal displacements for 12 GPS sites in Hong Kong are contained in the \attachment\chapter4\A.3 directory. The results of both the ambiguity-free (left) and ambiguity-fixed (right) estimates for each site are illustrated. In each plots, parameter numbers 1-6 are the M_2 east, north, vertical cosine

coefficients, followed by their sine coefficients. The other constituent parameters (S_2 , N_2 , K_2 , K_1 , O_1 , P_1 and Q_1 in turn) are followed in the same way.

A.4 GPS-derived tidal displacements and tidal gravity estimates in Hong Kong

GPS-derived tidal displacements of both the ambiguity-free and ambiguity-fixed solution and tidal gravity estimates in Hong Kong are listed in \attachment\chapter4\A.4.pdf.

Appendix B Auxiliary materials for Chapter 5

Auxiliary materials discussed in Chapter 5 are included in \attachment\chapter5 directory on the attached CD-ROM. They are also available through my homepage (<http://sites.google.com/site/linguosite/>). The auxiliary materials are provided in Portable Document Format (PDF) files.

B.1 Convergence plots for global GPS sites

Convergence plots for 125 global GPS sites are contained in the \attachment\chapter5\B.1 directory. The plot for each site shows the amplitudes of residual vectors after the addition of each daily solution, relative to the final estimates for east (top), north (middle) and vertical (bottom).

B.2 Tidal parameter correlations for global GPS sites

Parameter correlation plots of the tidal displacements for 125 global GPS sites are contained in the \attachment\chapter5\B.2 directory. In each plot for each site, parameter numbers 1-6 are the M_2 east, north, vertical cosine coefficients, followed by their sine coefficients. The other constituent parameters (S_2 , N_2 , K_2 , K_1 , O_1 , P_1 and Q_1 in turn) are followed in the same way.

B.3 Tidal displacement estimates for global GPS sites

Tidal displacement estimates for 125 global GPS sites are listed in \attachment\chapter5\ B.3.pdf. One standard deviation formal errors are also listed on

the next line for the corresponding parameter estimates. Amplitude is in millimetre, phase is positive for the Greenwich lag and N is the number of daily solutions after outlier removal.

B.4 Phasor diagrams of tidal displacement residuals

Phasor diagrams of the tidal displacement residuals after removing the FES2004 predictions for eight principal constituents are given in the \attachment\chapter5\B.4 directory. In each plot, The residuals are represented by the red solid (for the inland GPS sites more than 150 km from the coast), blue solid (the coastal GPS sites within 150 km of the coastline), the red open (for the inland VLBI sites more than 150 km from the coast) and blue open (the coastal VLBI sites within 150 km of the coastline) arrows. Phases increase clockwise from the upward direction.

Appendix C Auxiliary materials for Chapter 6

Auxiliary materials discussed in Chapter 6 are included in \attachment\chapter6 directory on the attached CD-ROM. They are also available through my homepage (<http://sites.google.com/site/linguosite/>). The auxiliary materials are provided in Portable Document Format (PDF) files.

C.1 Plots of difference time-series for GPS sites in Hong Kong

Plots of different difference time-series (ts21, ts31, ts24 and ts43) for GPS sites in Hong Kong are given in the \attachment\chapter6\C.1 directory, along with the corresponding amplitude spectra. For each plot, the left panel shows the difference time-series, and the right panel shows the corresponding amplitude spectra with 1% significance levels denoted by the dash-dotted lines. Major data processing and environmental changes are indicated by vertical lines in the left panel: The JPL global solutions began modelling OTL using the FES99 model on 03/03/2002 and then upgraded to the FES02 model on 23/07/2002; the antenna domes were added at all the Hong Kong sites in December 2004; and the JPL global solutions began modelling CMC on 05/11/2006.

C.2 Plots of difference time-series for global GPS sites

Plots of different difference time-series (ts21, ts31, ts24 and ts43) for 125 global GPS sites are given in the \attachment\chapter6\C.C directory, along with the corresponding amplitude spectra. For each plot, the left panel shows the difference

time-series, and the right panel shows the corresponding amplitude spectra with 1% significance levels denoted by the dash-dotted lines. Some major receiver and antenna changes are indicated by vertical blue and green lines in the left panel for all time-series, respectively. Changes in the satellite constellation are also shown in red lines in the left panel of both ts21 and ts43.

References

- Agnew D.C. (1986) Strainmeters and tiltmeters. *Reviews of Geophysics* 24: 579-624.
- Agnew D.C. (1996) SPOTL: Some programs for ocean-tide loading. *SIO Reference Series 96-8*, Scripps Institution of Oceanography, La Jolla.
- Agnew D.C. (1997) NLOADF: A program for computing ocean-tide loading. *Journal of Geophysical Research-Solid Earth* 102: 5109-5110.
- Agnew D.C. (2007) Earth tides. in *Treatise on Geophysics*, pp. 163-195, T. A. Herring, ed., Elsevier, New York.
- Allinson C.R., Clarke P.J., Edwards S.J., King M.A., Baker T.F., Cruddace P.R.. (2004) Stability of direct GPS estimates of ocean tide loading. *Geophysical Research Letters* 31(15), L15603, doi: 10.1029/2004GL020588.
- Altamimi Z., Collilieux X., Legrand J., Garayt B., Boucher C. (2007) ITRF2005: A new release of the International Terrestrial Reference Frame based on time series of station positions and Earth orientation parameters. *Journal of Geophysical Research-Solid Earth* 112, B09401, doi:10.1029/2007JB004949.
- Andersen O., Egbert G., Erofeeva S., Ray R. (2006) Non-linear tides in shallow water regions from multi-mission satellite altimetry & the Andersen 06 Global Ocean Tide Model. in AGU WPGM meeting, Beijing, China.

- Baker T.F., Bos M.S. (2003) Validating Earth and ocean tide models using tidal gravity measurements. *Geophysical Journal International* 152: 468-485.
- Blewitt G. (1989) Carrier phase ambiguity resolution for the global positioning system applied to geodetic baselines up to 2000 km. *Journal of Geophysical Research-Solid Earth and Planets* 94: 10187-10203.
- Blewitt G. (2003) Self-consistency in reference frames, geocenter definition, and surface loading of the solid Earth. *Journal of Geophysical Research-Solid Earth* 108(B2), 2103, doi:10.1029/2002JB002082.
- Blewitt G. (2008) Fixed point theorems of GPS carrier phase ambiguity resolution and their application to massive network processing: Ambizap. *Journal of Geophysical Research-Solid Earth* 113, B12410, doi:10.1029/2008JB005736.
- Blewitt G., Heflin M.B., Webb F.H., Lindqwister U.J., Malla R.P. (1992) Global coordinates with centimeter accuracy in the international terrestrial reference frame using GPS. *Geophysical Research Letters* 19: 853-856.
- Blewitt G., Lavallee D., Clarke P., Nurutdinov K. (2001) A new global mode of Earth deformation: Seasonal cycle detected. *Science* 294: 2342-2345.
- Bos M.S., Baker T.F. (2005) An estimate of the errors in gravity ocean tide loading computations. *Journal of Geodesy* 79: 50-63.
- Boy J.P., Hinderer J. (2006) Study of the seasonal gravity signal in superconducting

gravimeter data. *Journal of Geodynamics* 41: 227-233.

Boy J.P., Llubes M., Hinderer J., Florsch N. (2003) A comparison of tidal ocean loading models using superconducting gravimeter data. *Journal of Geophysical Research-Solid Earth* 108(B4), 2193, doi:10.1029/2002JB002050.

Boy J.P., Llubes M., Ray R., Hinderer J., Florsch N., Rosat S., Lyard F., Letellier T. (2004) Non-linear oceanic tides observed by superconducting gravimeters in Europe. *Journal of Geodynamics* 38: 391-405.

Braswell W.D., Lindzen R.S. (1998) Anomalous short wave absorption and atmospheric tides. *Geophysical Research Letters* 25: 1293-1296.

Brush S.G. (1996) *Nebulous Earth: the Origin of the Solar System and the Core of the Earth from Laplace to Jeffreys*. Cambridge University Press, Cambridge.

Bullesfeld F.J. (1985) Ein Beitrag Zur Harmonischen Darstellung Des Gezeitenerzeugenden Potentials. *Veroeffentlichungen der Deutschen Geodaetischen Kommission, Reihe C* 31: 3-103.

Cartwright D.E., Edden A.C. (1973) Corrected tables of tidal harmonics. *Geophysical Journal of the Royal Astronomical Society* 33: 253-264.

Cartwright D.E., Tayler R.J. (1971) New computations of tide-generating potential. *Geophysical Journal of the Royal Astronomical Society* 23: 45-74.

- Chapman S., Lindzen R.S. (1970) Atmospheric tides: thermal and gravitational. Gordon and Breach, New York.
- Clarke P.J., Lavallee D.A., Blewitt G., van Dam T. (2007) Basis functions for the consistent and accurate representation of surface mass loading. *Geophysical Journal International* 171: 1-10.
- Cochran E.S., Vidale J.E., Tanaka S. (2004) Earth tides can trigger shallow thrust fault earthquakes. *Science* 306: 1164-1166.
- Crossley D., Hinderer J., Casula G., Francis O., Hsu H.T., Imanishi Y., Jentzsch G., Kaarianen J., Merriam J., Meurers B. (1999) Network of superconducting gravimeters benefits a number of disciplines. *Eos, Transactions American Geophysical Union* 80(11) : 121-121.
- Darwin G.H. (1883) Report of a committee for the harmonic analysis of tidal observations. *Brit. Assoc. Advancement Sci., Rept*: 49-118.
- Dehant V., Defraigne P., Wahr J.M. (1999) Tides for a convective Earth. *Journal of Geophysical Research-Solid Earth* 104: 1035-1058.
- Desai S.D. (2002) Observing the pole tide with satellite altimetry. *Journal of Geophysical Research-Oceans* 107 (C11), 3186, doi:10.1029/2001JC001224.
- Dong D., Fang P., Bock Y., Cheng M.K., Miyazaki S. (2002) Anatomy of apparent seasonal variations from GPS-derived site position time series. *Journal of*

Geophysical Research-Solid Earth 107 (B4), 2075,
doi:10.1029/2001JB000573.

Dong D., Yunck T., Heflin M. (2003) Origin of the international Terrestrial Reference Frame. *Journal of Geophysical Research-Solid Earth* 108 (B4), 2200,
doi:10.1029/2002JB002035.

Doodson A.T. (1921) The harmonic development of the tide-generating potential. *Proceedings of the Royal Society of London Series a - Containing Papers of a Mathematical and Physical Character* 100: 305-329.

Dragert H., James T.S., Lambert A. (2000) Ocean loading corrections for continuous GPS: A case study at the Canadian coastal site Holberg. *Geophysical Research Letters* 27: 2045-2048.

Ducarme B., Venedikov A.P., Arnos J., Vieira R. (2004) Determination of the long period tidal waves in the GGP superconducting gravity data. *Journal of Geodynamics* 38: 307-324.

Dziewonski A.M., Anderson D.L. (1981) Preliminary Reference Earth Model. *Physics of the Earth and Planetary Interiors* 25: 297-356.

Eanes R.J. (1994) Diurnal and semidiurnal tides from TOPEX/POSEIDON altimetry. *Eos Trans. AGU* 75: 108.

Eanes R.J., Shuler A. (1999) An improved global ocean tide model from

- TOPEX/Poseidon altimetry: CSR4. 0. *EGS 24th General Assembly, The Hague*.
- Egbert G.D., Bennett A.F., Foreman M.G.G. (1994) TOPEX/Poseidon tides estimated using a global inverse model. *Journal of Geophysical Research-Oceans* 99: 24821-24852.
- Egbert G.D., Erofeeva S.Y. (2002) Efficient inverse modeling of barotropic ocean tides. *Journal of Atmospheric and Oceanic Technology* 19: 183-204.
- Fang G.H., Kwok Y.K., Yu K.J., Zhu Y.H. (1999) Numerical simulation of principal tidal constituents in the South China Sea, Gulf of Tonkin and Gulf of Thailand. *Continental Shelf Research* 19: 845-869.
- Fang G.H., Wang Y.G., Wei Z.X., Choi B.H., Wang X.Y., Wang J. (2004) Empirical cotidal charts of the Bohai, Yellow, and East China Seas from 10 years of TOPEX/Poseidon altimetry. *Journal of Geophysical Research-Oceans* 109, C11006, doi:10.1029/2004JC002484.
- Farrell W.E. (1972) Deformation of Earth by surface loads. *Reviews of Geophysics and Space Physics* 10: 761-797.
- Foreman M.G.G. (1979) Manual for tidal heights analysis and prediction. *Patricia Bay. Pacific Marine Science Report 77-10*, Institute of Ocean Sciences, Patricia Bay, Sidney, BC, 97pp.

- Ge M., Gendt G., Dick G., Zhang F.P., Reigber C. (2005) Impact of GPS satellite antenna offsets on scale changes in global network solutions. *Geophysical Research Letters* 32, L06310, doi:10.1029/2004GL022224.
- Gregorius T. (1996) GIPSY-OASIS II: How it works? Univ. of Newcastle upon Tyne, Newcastle, England, U.K.
- Haas R., Schuh H. (1998) Ocean loading observed by geodetic VLBI, In: Ducarme B and Paquet P (eds.) *Proceedings of the 13th International Symposium on Earth Tides*, pp. 111–120. Brussels: Observatoire Royal de Belgique.
- Han S.C., Ray R.D., Luthcke S.B. (2007) Ocean tidal solutions in Antarctica from GRACE inter-satellite tracking data. *Geophysical Research Letters* 34, L21607, doi:10.1029/2007GL031540.
- Hartmann T., Wenzel H.G. (1995) The HW95 tidal potential catalogue. *Geophysical Research Letters* 22: 3553-3556.
- Hewitt E., Hewitt R.E. (1979) Gibbs-Wilbraham phenomenon - episode in fourier-analysis. *Archive for History of Exact Sciences* 21: 129-160.
- Hinderer J., Crossley D. (2000) Time variations in gravity and inferences on the Earth's structure and dynamics. *Surveys in Geophysics* 21: 1-45.
- Hinderer J., Crossley D. (2004) Scientific achievements from the first phase (1997-2003) of the Global Geodynamics Project using a worldwide network

- of superconducting gravimeters. *Journal of Geodynamics* 38: 237-262.
- Hinderer J., Crossley D., Warburton R.J., Gerald S. (2007) Gravimetric methods - superconducting gravity meters. in *Treatise on Geophysics*, pp. 65-122, Elsevier, Amsterdam.
- Hobson E.W. (1955) The theory of spherical and ellipsoidal harmonics. Chelsea, New York.
- Iwano S., Fukuda Y., Sato T., Tamura Y., Matsumoto K., Shibuya K. (2005) Long-period tidal factors at Antarctica Syowa Station determined from 10 years of superconducting gravimeter data. *Journal of Geophysical Research-Solid Earth* 110, B10403, doi:10.1029/2004JB003551.
- Jentzsch G. (1997) Earth tides and ocean tidal loading. in *Tidal Phenomena*. Lecture Notes in Earth Sciences, vol. 66, pp. 145–171.
- Kalnay E., Kanamitsu M., Kistler R., Collins W., Deaven D., Gandin L., Iredell M., Saha S., White G., Woollen J., Zhu Y., Chelliah M., Ebisuzaki W., Higgins W., Janowiak J., Mo K.C., Ropelewski C., Wang J., Leetmaa A., Reynolds R., Jenne R., Joseph D. (1996) The NCEP/NCAR 40-year reanalysis project. *Bulletin of the American Meteorological Society* 77: 437-471.
- Kasahara J. (2002) Geophysics: Tides, earthquakes, and volcanoes. *Science* 297: 348-349.

- Kedar S., Hajj G.A., Wilson B.D., Heflin M.B. (2003) The effect of the second order GPS ionospheric correction on receiver positions. *Geophysical Research Letters* 30(16), 1829, doi:10.1029/2003GL017639.
- Khan S.A., Hoyer J.L. (2004) Shallow-water loading tides in Japan from superconducting gravimetry. *Journal of Geodesy* 78: 245-250.
- Khan S.A., Scherneck H.G. (2003) The M_2 ocean tide loading wave in Alaska: vertical and horizontal displacements, modelled and observed. *Journal of Geodesy* 77: 117-127.
- Khan S.A., Tscherning C.C. (2001) Determination of semi-diurnal ocean tide loading constituents using GPS in Alaska. *Geophysical Research Letters* 28: 2249-2252.
- King M. (2006) Kinematic and static GPS techniques for estimating tidal displacements with application to Antarctica. *Journal of Geodynamics* 41: 77-86.
- King M., Colemar R., Nguyen L.N. (2003) Spurious periodic horizontal signals in sub-daily GPS position estimates. *Journal of Geodesy* 77: 15-21.
- King M., Williams S.D.P. (2009) Apparent stability of GPS monumentation from short baseline time series. *Journal of Geophysical Research-Solid Earth*. doi:10.1029/2009JB006319, in press.

- King M.A., Penna N.T., Clarke P.J., King E.C. (2005) Validation of ocean tide models around Antarctica using onshore GPS and gravity data. *Journal of Geophysical Research-Solid Earth* 110, B08401, doi:10.1029/2004JB003390.
- King M.A., Watson C.S., Penna N.T., Clarke P.J. (2008) Subdaily signals in GPS observations and their effect at semiannual and annual periods. *Geophysical Research Letters* 35, L03302, doi:10.1029/2007GL032252.
- Kudryavtsev S.M. (2004) Improved harmonic development of the Earth tide-generating potential. *Journal of Geodesy* 77: 829-838.
- Lambert A., Pagiatakis S.D., Billyard A.P., Dragert H. (1998) Improved ocean tide loading corrections for gravity and displacement: Canada and northern United States. *Journal of Geophysical Research-Solid Earth* 103: 30231-30244.
- Larson K.M., Freymueller J.T., Philipsen S. (1997) Global plate velocities from the Global Positioning System. *Journal of Geophysical Research-Solid Earth* 102: 9961-9981.
- Lavallee D.A., van Dam T., Blewitt G., Clarke P.J. (2006) Geocenter motions from GPS: A unified observation model. *Journal of Geophysical Research-Solid Earth* 111, B05405, doi:10.1029/2005JB003784.
- Le Meur E., Hindmarsh R.C.A. (2000) A comparison of two spectral approaches for computing the Earth response to surface loads. *Geophysical Journal*

International 141: 282-298.

Le Provost C., Genco M.L., Lyard F., Vincent P., Canceil P. (1994) Spectroscopy of the world ocean tides from a finite-element hydrodynamic model. *Journal of Geophysical Research-Oceans* 99: 24777-24797.

Le Provost C., Lyard F., Molines J.M. (1991) Improving ocean tide predictions by using additional semidiurnal constituents from spline interpolation in the frequency-domain. *Geophysical Research Letters* 18: 845-848.

Le Provost C., Lyard F., Molines J.M., Genco M.L., Rabilloud F. (1998) A hydrodynamic ocean tide model improved by assimilating a satellite altimeter-derived data set. *Journal of Geophysical Research-Oceans* 103: 5513-5529.

Lefevre F., Lyard F.H., Le Provost C. (2000) FES98: A new global tide finite element solution independent of altimetry. *Geophysical Research Letters* 27: 2717-2720.

Lefevre F., Lyard F.H., Le Provost C., Schrama E.J.O. (2002) FES99: A global tide finite element solution assimilating tide gauge and altimetric information. *Journal of Atmospheric and Oceanic Technology* 19: 1345-1356.

Lichten S.M. (1990) Estimation and filtering for high-precision GPS positioning applications. *Manuscripta Geodaetica* 15: 159-176.

Love A.E.H. (1909) The Yielding of the Earth to Disturbing Forces. *Proceedings of the Royal Society of London. Series A, Containing Papers of a Mathematical and Physical Character* 82: 73-88.

Lyard F., Lefevre F., Letellier T., Francis O. (2006) Modelling the global ocean tides: modern insights from FES2004. *Ocean Dynamics* 56: 394-415.

Mathews P.M., Buffett B.A., Shapiro I.I. (1995) Love numbers for a rotating spheroidal Earth - new definitions and numerical values. *Geophysical Research Letters* 22: 579-582.

Mathews P.M., Dehant V., Gipson J.M. (1997) Tidal station displacements. *Journal of Geophysical Research-Solid Earth* 102: 20469-20477.

Matsumoto K., Takanezawa T., Ooe M. (2000) Ocean tide models developed by assimilating TOPEX/Poseidon altimeter data into hydrodynamical model: a global model and a regional model around Japan. *Journal of Oceanography* 56: 567-581.

McCarthy D.D. (1996) IERS conventions (1996). *IERS Technical Note 21*. Frankfurt am Main, Germany.

McCarthy D.D., Petit G. (2004) IERS Conventions (2003). *IERS Technical Note 32*. Frankfurt am Main, Germany.

Melachroinos S.A., Biancale R., Llubes M., Perosanz F., Lyard F., Vergnolle M.,

- Bouin M.N., Masson F., Nicolas J., Morel L., Durand S. (2008) Ocean tide loading (OTL) displacements from global and local grids: comparisons to GPS estimates over the shelf of Brittany, France. *Journal of Geodesy* 82: 357-371.
- Metivier L., Conrad C.P. (2008) Body tides of a convecting, laterally heterogeneous, and aspherical Earth. *Journal of Geophysical Research-Solid Earth* 113, B11405, doi:10.1029/2007JB005448.
- Milne G.A., Davis J.L., Mitrovica J.X., Scherneck H.G., Johansson J.M., Vermeer M., Koivula H. (2001) Space-geodetic constraints on glacial isostatic adjustment in Fennoscandia. *Science* 291: 2381-2385.
- Mitrovica J.X., Davis J.L., Mathews P.M., Shapiro I.I. (1994a) Determination of tidal Love number parameters in the diurnal band using an extensive VLBI data set. *Geophysical Research Letters* 21: 705-708.
- Mitrovica J.X., Davis J.L., Shapiro I.I. (1994b) A spectral formalism for computing 3-dimensional deformations due to surface loads .1. Theory. *Journal of Geophysical Research-Solid Earth* 99: 7057-7073.
- Molteni F., Buizza R., Palmer T.N., Petroliagis T. (1996) The ECMWF ensemble prediction system: Methodology and validation. *Quarterly Journal of the Royal Meteorological Society* 122: 73-119.

- Munk W.H., Cartwright D.E. (1966) Tidal spectroscopy and prediction. *Philosophical Transactions of the Royal Society of London Series a - Mathematical and Physical Sciences* 259: 533-581.
- Munk W.H., Macdonald G.J.F. (1960) The rotation of the Earth. A geophysical discussion, 323 pp. University Press, Cambridge.
- Niell A.E. (1996) Global mapping functions for the atmosphere delay at radio wavelengths. *Journal of Geophysical Research-Solid Earth* 101: 3227-3246.
- Pagiatakis S.D. (1990) The response of a realistic Earth to ocean tide loading. *Geophysical Journal International* 103: 541-560.
- Penna N.T., Bos M., Baker T., Scherneck H.G. (2008) Assessing the accuracy of predicted ocean tide loading displacement values. *Journal of Geodesy* 82: 893-907.
- Penna N.T., King M.A., Stewart M.P. (2007) GPS height time series: Short-period origins of spurious long-period signals. *Journal of Geophysical Research-Solid Earth* 112, B02402, doi:10.1029/2005JB004047.
- Penna N.T., Stewart M.P. (2003) Aliased tidal signatures in continuous GPS height time series. *Geophysical Research Letters* 30 (23), 2184, doi:10.1029/2003GL018828.
- Petrov L., Ma C.P. (2003) Study of harmonic site position variations determined by

- very long baseline interferometry. *Journal of Geophysical Research-Solid Earth* 108 (B4), 2190, doi:10.1029/2002JB001801.
- Prawirodirdjo L., Bock Y. (2004) Instantaneous global plate motion model from 12 years of continuous GPS observations. *Journal of Geophysical Research-Solid Earth* 109, B08405, doi:10.1029/2003JB002944.
- Ray J., Altamimi Z., Collilieux X., van Dam TL. (2008) Anomalous harmonics in the spectra of GPS position estimates. *GPS Solutions* 12: 55-64.
- Ray J., Altamimi Z., van Dam T., Herring T. (2007) Principles for conventional contributions to modeled station displacements, Position paper presented at the IERS Workshop on Conventions, Paris, September 22-23, 2007.
- Ray R.D. (1998) Diurnal oscillations in atmospheric pressure at twenty-five small oceanic islands. *Geophysical Research Letters* 25: 3851-3854.
- Ray R.D. (1999) A global ocean tide model from TOPEX/Poseidon altimetry: GOT99. 2. *NASA Tech. Memo* 209478: 58.
- Ray R.D. (2001) Comparisons of global analyses and station observations of the S-2 barometric tide. *Journal of Atmospheric and Solar-Terrestrial Physics* 63: 1085-1097.
- Ray R.D., Eanes R.J., Egbert G.D., Pavlis N.K. (2001) Error spectrum for the global M_2 ocean tide. *Geophysical Research Letters* 28: 21-24.

- Ray R.D., Egbert G.D. (2004) The global S_1 tide. *Journal of Physical Oceanography* 34: 1922-1935.
- Ray R.D., Ponte R.M. (2003) Barometric tides from ECMWF operational analyses. *Annales Geophysicae* 21: 1897-1910.
- Ray R.D., Sanchez B.V. (1989) Radial deformation of the Earth by oceanic tidal loading. NASA. Technical Memorandum 100743, National Aeronautics and Space Administration, Goddard Space Flight Center, Greenbelt, Md.
- Roosbeek F. (1996) RATGP95: A harmonic development of the tide-generating potential using an analytical method. *Geophysical Journal International* 126: 197-204.
- Rosat S., Lambert S.B. (2009) Free core nutation resonance parameters from VLBI and superconducting gravimeter data. *Astronomy & Astrophysics* 503: 287-291.
- Ryan J.W., Clark T.A., Coates R.J., Ma C., Wildes W.T., Gwinn C.R., Herring T.A., Shapiro I.I., Corey B.E., Counselman C.C., Hinteregger H.F., Rogers A.E.E., Whitney A.R., Knight C.A., Vandenberg N.R., Pigg J.C., Schupler B.R., Ronnang B.O. (1986) Geodesy by radio interferometry - Determinations of baseline vector, Earth rotation, and solid Earth tide parameters with the Mark-I very long baseline radio interferometry system. *Journal of Geophysical Research-Solid Earth and Planets* 91: 1935-1946.

- Saastamoinen J. (1972) Atmospheric correction for troposphere and stratosphere in radio ranging of satellites. *Geophysical monograph 15*, American Geophysical Union, Washington D.C., USA, pp 247 – 252.
- Sato T., Tamura Y., Matsumoto K., Imanishi Y., McQueen H. (2004) Parameters of the fluid core resonance inferred from superconducting gravimeter data. *Journal of Geodynamics 38*: 375-389.
- Savcenko R., Bosch W. (2008) EOT08a - empirical ocean tide model from multi-mission satellite altimetry. in Report No. 81 Deutsches Geodätisches Forschungsinstitut (DGFI), München.
- Scargle J.D. (1982) Studies in astronomical time-series analysis .2. Statistical aspects of spectral-analysis of unevenly spaced data. *Astrophysical Journal 263*: 835-853.
- Schenewerk M.S., Marshall J., Dillinger W. (2001) Vertical ocean-loading deformations derived from a global GPS network. *Journal of the Geodetic Society of Japan 47*: 237-242.
- Scherneck H.G. (1991) A parametrized solid Earth tide model and ocean tide loading effects for global geodetic baseline measurements. *Geophysical Journal International 106*: 677-694.
- Scherneck H.G., Johansson J.M., Webb F.H. (2000) Ocean loading tides in GPS and

- rapid variations of the frame origin. *Geodesy Beyond: 2000*, 19-30, Springer.
- Schwiderski E.W. (1980) On charting global ocean tides. *Reviews of Geophysics* 18: 243-268.
- Schrama E.J.O. (2005) Three algorithms for the computation of tidal loading and their numerical accuracy. *Journal of Geodesy* 78: 707-714.
- Sella G.F., Stein S., Dixon T.H., Craymer M., James T.S., Mazzotti S., Dokka R.K. (2007) Observation of glacial isostatic adjustment in "stable" North America with GPS. *Geophysical Research Letters* 34, L02306, doi:10.1029/2006GL027081.
- Shannon C.E. (1998) Communication in the presence of noise (Reprinted from the Proceedings of the IRE, vol 37, pg 10-21, 1949). *Proceedings of the IEEE* 86: 447-457.
- Shida T., Matsuyama M. (1912) On the elasticity of the Earth and the Earth's crust. *Mem. Coll. Sci. Engng. Kyoto Univ* 4: 277-284.
- Shum C.K., Woodworth P.L., Andersen O.B., Egbert G.D., Francis O., King C., Klosko S.M., LeProvost C., Li X., Molines J.M., Parke M.E., Ray R.D., Schlax M.G., Stammer D., Tierney C.C., Vincent P., Wunsch C.I. (1997) Accuracy assessment of recent ocean tide models. *Journal of Geophysical Research-Oceans* 102: 25173-25194.

- Sovers O.J. (1994) Vertical ocean loading amplitudes from VLBI measurements. *Geophysical Research Letters* 21: 357-360.
- Stewart M.P., Penna N.T., Lichti D.D. (2005) Investigating the propagation mechanism of unmodelled systematic errors on coordinate time series estimated using least squares. *Journal of Geodesy* 79: 479-489.
- Sun H., Ducarme B., Xu H., Vandercoilden L., Xu J., Zhou J. (2005) Adaptability of the ocean and Earth tidal models based on global observations of the superconducting gravimeters. *Science in China Series D: Earth Sciences* 48: 1859-1869.
- Sun H.P., Hsu H., Chen W., Chen X.D., Zhou J.C., Liu M., Gao S. (2006) Study of Earth's gravity tide and oceanic loading characteristics in Hong Kong area. *Chinese Journal of Geophysics-Chinese Edition* 49: 724-734.
- Sun H.P., Jentzsch G., Xu J.Q., Hsu H.Z., Chen X.D., Zhou J.C. (2004) Earth's free core nutation determined using C032 superconducting gravimeter at station Wuhan/China. *Journal of Geodynamics* 38: 451-460.
- Tamura Y. (1987) A harmonic development of the tide-generating potential. *Bulletin d'Information des Mare'es Terrestres* 99: 6813-6855.
- Thomas A.M., Nadeau R.M., Burgmann R. (2009) Tremor-tide correlations and near-lithostatic pore pressure on the deep San Andreas fault. *Nature* 462:

1048-1051.

Thomas I.D., King M.A., Clarke P.J. (2007) A comparison of GPS, VLBI and model estimates of ocean tide loading displacements. *Journal of Geodesy* 81: 359-368.

Tregoning P., Watson C. (2009) Atmospheric effects and spurious signals in GPS analyses. *Journal of Geophysical Research-Solid Earth*. 114, B09403, doi:10.1029/2009JB006344.

van den Dool H.M., Saha S., Schemm J., Huang J. (1997) A temporal interpolation method to obtain hourly atmospheric surface pressure tides in Reanalysis 1979-1995. *Journal of Geophysical Research-Atmospheres* 102: 22013-22024.

Vergnolle M., Bouin M.N., Morel L., Masson F., Durand S., Nicolas J., Melachroinos S.A. (2008) GPS estimates of ocean tide loading in NW-France: determination of ocean tide loading constituents and comparison with a recent ocean tide model. *Geophysical Journal International* 173: 444-458.

Vey S., Calais E., Llubes M., Florsch N., Woppelmann G., Hinderer J., Amalviet M., Lalancette M.F., Simon B., Duquenne F., Haase J.S. (2002) GPS measurements of ocean loading and its impact on zenith tropospheric delay estimates: a case study in Brittany, France. *Journal of Geodesy* 76: 419-427.

- Wahr J.M. (1981) Body tides on an elliptical, rotating, elastic and oceanless Earth. *Geophysical Journal of the Royal Astronomical Society* 64: 677-703.
- Wahr J.M. (1985) Deformation induced by polar motion. *Journal of Geophysical Research-Solid Earth and Planets* 90: 9363-9368.
- Wahr J.M., Sasao T. (1981) A diurnal resonance in the ocean tide and in the Earth's load response due to the resonant free core nutation. *Geophysical Journal of the Royal Astronomical Society* 64: 747-765.
- Watson C., Tregoning P., Coleman R. (2006) Impact of solid Earth tide models on GPS coordinate and tropospheric time series. *Geophysical Research Letters* 33, L08306, doi:10.1029/2005GL025538.
- Watson C.S. (2005) Satellite altimeter calibration and validation using GPS buoy technology. Thesis for Doctor of Philosophy, University of Tasmania, Hobart, Australia.
- Webb F.H., Zumberge J.F. (1997) An introduction to GIPSY/OASIS-II. *JPL Publ. D-11088, Jet Propulsion Laboratory, California Institution of Technology, Pasadena.*
- Wessel P., Smith W.H.F. (1998) New, improved version of generic mapping tools released. *Eos, Transactions American Geophysical Union* 79: 579-579.
- Widmer R., Masters G., Gilbert F. (1991) Spherically symmetric attenuation within

- the Earth from normal mode data. *Geophysical Journal International* 104: 541-553.
- Williams S.D.P., Bock Y., Fang P., Jamason P., Nikolaidis R.M., Prawirodirdjo L., Miller M., Johnson D.J. (2004) Error analysis of continuous GPS position time series. *Journal of Geophysical Research-Solid Earth* 109, B03412, doi:10.1029/2003JB002741.
- Wu X.P., Heflin M.B., Ivins E.R., Argus D.F., Webb F.H. (2003) Large-scale global surface mass variations inferred from GPS measurements of load-induced deformation. *Geophysical Research Letters* 30 (14), 1742, doi:10.1029/2003GL017546.
- Wu X.P., Heflin M.B., Ivins E.R., Fukumori I. (2006) Seasonal and interannual global surface mass variations from multisatellite geodetic data. *Journal of Geophysical Research-Solid Earth* 111, B09401, doi:10.1029/2005JB004100.
- Xi Q.W. (1987) A new complete development of the tide-generating potential for the epoch J 2000. 0. *Bulletin d'Information des Mare' es Terrestres* 99: 6766-6812.
- Xu J.Q., Sun H.P., Luo S.C. (2002) Study of the Earth's free core nutation by tidal gravity data recorded with international superconducting gravimeters. *Science in China Series D-Earth Sciences* 45: 337-347.

- Yun H.S., Lee D.H., Song D.S. (2007) Determination of vertical displacements over the coastal area of Korea due to the ocean tide loading using GPS observations. *Journal of Geodynamics* 43: 528-541.
- Zumberge J.F., Heflin M.B., Jefferson D.C., Watkins M.M., Webb F.H. (1997) Precise point positioning for the efficient and robust analysis of GPS data from large networks. *Journal of Geophysical Research-Solid Earth* 102: 5005-5017.
- Zürn W. (1997) Earth tide observations and interpretation. in: Wilhelm H, Zürn W, and Wenzel HG (eds.) *Tidal Phenomena*, pp. 95–109. Berlin: Springer-Verlag.
- Zurn W., Beaumont C., Slichter L.B. (1976) Gravity tides and ocean loading in southern Alaska. *J. geophys. Res.* 81: 4923-4932.